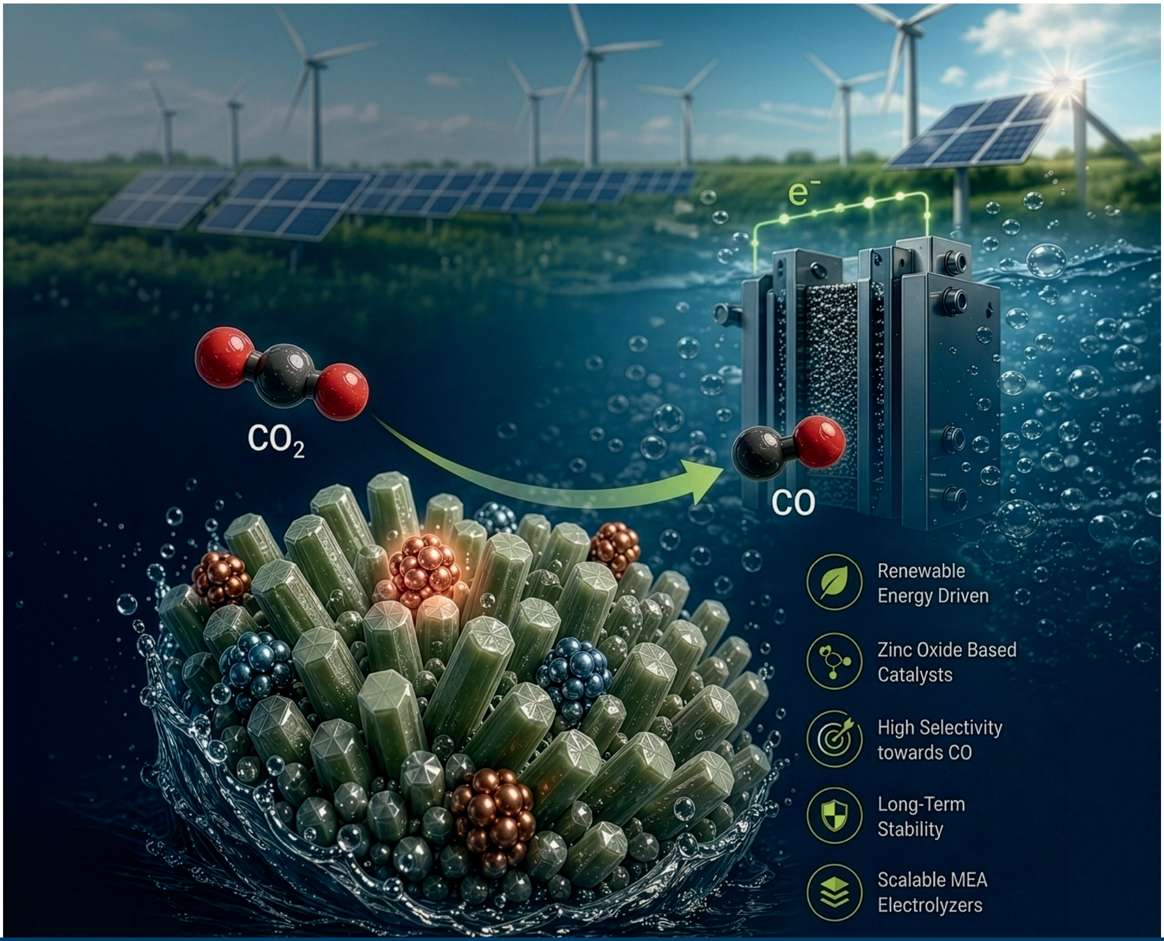

Zinc-Based Catalysts for the Electrochemical CO_2 Reduction

Ilias Stamatelos

Energie & Umwelt / Energy & Environment
Band / Volume 714
ISBN 978-3-95806-933-6

Mitglied der Helmholtz-Gemeinschaft

JÜLICH
Forschungszentrum

Schriften des Forschungszentrums Jülich
Reihe Energie & Umwelt / Energy & Environment Band / Volume 714

Forschungszentrum Jülich GmbH
Institute of Energy Technologies (IET)
Elektrochemische Verfahrenstechnik (IET-4)

Zinc-Based Catalysts for the Electrochemical CO_2 Reduction

Ilias Stamatelos

Schriften des Forschungszentrums Jülich
Reihe Energie & Umwelt / Energy & Environment Band / Volume 714

ISSN 1866-1793 ISBN 978-3-95806-933-6

Bibliografische Information der Deutschen Nationalbibliothek.
Die Deutsche Nationalbibliothek verzeichnet diese Publikation in der
Deutschen Nationalbibliografie; detaillierte Bibliografische Daten
sind im Internet über http://dnb.d-nb.de abrufbar.

Herausgeber und Vertrieb: Forschungszentrum Jülich GmbH
Zentralbibliothek, Verlag
52425 Jülich
Tel.: +49 2461 61-5368
Fax: +49 2461 61-6103
zb-publikation@fz-juelich.de
www.fz-juelich.de/zb

Umschlaggestaltung: Grafische Medien, Forschungszentrum Jülich GmbH

Titelbild: KI-gestütztes Design

Druck: Grafische Medien, Forschungszentrum Jülich GmbH

Schriften des Forschungszentrums Jülich
Reihe Energie & Umwelt / Energy & Environment, Band / Volume 714

D 82 (Diss. RWTH Aachen University, 2026)

ISSN 1866-1793
ISBN 978-3-95806-932-9 (Print)
ISBN 978-3-95806-933-6 (E-Book)

Abstract

The electrochemical reduction of carbon dioxide, ECR, fueled by renewable energy sources, holds promise for addressing escalating greenhouse emissions and closing the carbon cycle. This thesis focuses on developing cost-effective catalysts to facilitate the electrochemical conversion of CO_2 to CO. Utilizing low-temperature wet-chemical synthesis, zinc oxide, ZnO, based materials were synthesized and extensively characterized. The electrochemical characteristics and ECR performance of these materials were investigated in various electrolyzers, including H-cells, flow-cells, and zero-gap cells. Employing analytical techniques such as gas and ionic chromatography, we systematically mapped the product selectivity of different materials, offering detailed insights into the functions of the catalysts during ECR.

To maximize the ZnO CO_2-to-CO ECR capability, various ZnO allotropes were synthesized, revealing distinct differences in morphology and surface constitution. ZnO nanorods emerged as the most promising, exhibiting high ECR performance with a Faradaic Efficiency for CO FE_{CO} of over 80% in a current density range of 50–160 mA cm^{-2}, in both flow-cell and membrane-electrode-assembly (MEA) electrolyzers. Despite an initial stability challenge attributed to the depletion of the ECR-active ZnO phase, an in-situ regeneration strategy was developed, demonstrating stable CO_2-to-CO conversion for over 100 hours at 160 mA cm^{-2}.

To enhance direct and stable electrolysis, ZnO-based heterostructures decorated with d-block metal oxides of: Cu, Ni, Co, Fe, were explored. Among these, Cu/ZnO binary oxide showed the highest partial current density for CO j_{CO} and exceptional stability of 30 hours with a FE_{CO} of 77% at 100 mA cm^{-2}. The stabilizing effect of Cu on the ZnO phase enhanced overall ECR performance. Expanding our investigation, ternary Zn-Ce-Ag oxide catalysts were fabricated, achieving a FE_{CO} of 80% for 100 hours at 200 mA cm^{-2}. Further addition of a small amount of silver, less than 10 wt. %, led to a structured core-shell morphology, resulting in a remarkable FE_{CO} of 90% at 200 mA cm^{-2}, with exceptional stability for 200 hours in the MEA.

This research offers critical insights into the design of efficient ECR catalysts, displaying their potential for real-world application in large-scale, of 100 cm^2 active area, MEA electrolyzers. The catalysts developed not only advance fundamental understanding but also pave the way for the practical implementation of ECR technology.

Keywords: *Zinc Oxide, CO_2-to-CO, electrochemical CO_2 reduction, membrane electrode assembly, stability, heterostructures, large-scale*

Zusammenfassung

Die elektrochemische Reduktion von Kohlendioxid, ECR, die mit erneuerbaren Energiequellen betrieben wird, ist ein vielversprechender Weg, um die eskalierenden Treibhausgasemissionen zu bekämpfen und den Kohlenstoffkreislauf zu schließen. Diese Arbeit konzentriert sich auf die Entwicklung kostengünstiger Katalysatoren, die die elektrochemische Umwandlung von CO_2 in CO erleichtern. Mittels nasschemischer Niedertemperatursynthese wurden Materialien auf der Basis von Zinkoxid, ZnO, synthetisiert und eingehend charakterisiert. Die elektrochemischen Eigenschaften und die ECR-Leistung dieser Materialien wurden in verschiedenen Elektrolyseuren untersucht, darunter H-Zellen, Durchflusszellen und Zero-Gap-Zellen. Mit Hilfe von Analysetechniken wie der Gas- und Ionenchromatographie haben wir die Produktselektivität der verschiedenen Materialien systematisch kartiert und so detaillierte Einblicke in die Funktionen der Katalysatoren während der ECR erhalten.

Um die CO_2-zu-CO-ECR-Fähigkeit von ZnO zu maximieren, wurden verschiedene ZnO-Allotrope synthetisiert, die deutliche Unterschiede in Morphologie und Oberflächenbeschaffenheit aufwiesen. ZnO-Nanostäbchen erwiesen sich als die vielversprechendsten und zeigten eine hohe ECR-Leistung mit einer Faradaischen Wirkungsgrad für CO FE_{CO} von über 80% in einem Stromdichtebereich von 50-160 mA cm^{-2}, sowohl in Durchflusszellen als auch in Membran-Elektroden-Einheit-Elektrolyseure (MEA). Trotz anfänglicher Stabilitätsprobleme, die auf die Erschöpfung der ECR-aktiven ZnO-Phase zurückzuführen waren, wurde eine In-situ-Regenerationsstrategie entwickelt, die eine stabile CO_2-zu-CO-Umwandlung über 100 Stunden bei 160 mA cm^{-2} zeigte.

Um die direkte und stabile Elektrolyse zu verbessern, wurden Heterostrukturen auf ZnO-Basis untersucht, die mit d-Block-Metalloxiden von: Cu, Ni, Co, Fe, dekoriert sind. Unter diesen zeigte das binäre Cu/ZnO-Oxid die höchste Teilstromdichte für CO j_{CO} und eine außergewöhnliche Stabilität von 30 Stunden, mit einer FE_{CO} von 77 % bei 100 mA cm^{-2}. Die stabilisierende Wirkung von Cu auf die ZnO-Phase verbesserte die gesamte ECR-Leistung. In Erweiterung unserer Untersuchung wurden ternäre Zn-Ce-Ag-Oxid-Katalysatoren hergestellt, die 100 Stunden lang bei 200 mA cm^{-2} eine FE_{CO} von 80 % erreichten. Die weitere Zugabe einer kleinen Menge Silber, weniger als 10%, führte zu einer strukturierten Kern-Schale-Morphologie, was zu einem bemerkenswerten FE_{CO} von 90% bei 200 mA cm^{-2} führte, mit einer außergewöhnlichen Stabilität für 200 Stunden in der MEA.

Diese Forschungsarbeit bietet entscheidende Einblicke in die Entwicklung effizienter ECR-Katalysatoren und zeigt ihr Potential für die praktische Anwendung in großangelegten, mit 100 cm^2 aktiver Flache, MEA-Elektrolyseuren. Die entwickelten Katalysatoren fördern nicht nur das grundlegende Verständnis, sondern eben auch den Weg für die praktische Umsetzung der ECR-Technologie.

Table of Contents

Acknowledgments

I would like to thank Prof. Stolten for showing interest in my work and being my doctorate father. I am grateful for his useful scientific insight and his guidance through the tedious process of writing my thesis. Alongside, I want to express my sincere gratitude to Dr. Pasel, for his continuous support and guidance all these years.

Electrochemistry is a complex and multi-disciplinary field, that tends to avert the uninitiated people who show interest in it. As such, I want to thank both Prof. Lopes and Dr. Scheepers, who took the responsibility and task of mentoring and introducing me to this realm. A task that would certainly not have had the same impact, without the meaningful discussions and knowledge exchange that I had with my fellow doctorate colleagues of IEK-14.

It would be honestly difficult for me to summarize in a few lines the gratitude and respect that I feel for Prof. Dinh. He gave me someone to look up to, not only as a scientist but also as a person.

Η διατριβή αυτή αφιερώνεται εξ’ ολοκλήρου εις την οικογένειά μου. Η ανατροφή τους καθώς και η πνευματική, ηθική και υλική υποστήριξη που μου παρείχαν αφειδώς, και με πολλή αγάπη, ουσιαστικά προεξόφλησαν την μέχρι τώρα πορεία μου. Εις αυτούς χρωστώ τα πάντα μέχρις εδώ, και χάρη σ’ αυτούς προσβλέπω εις ένα φωτεινό μέλλον.

Βαθιές ρίζες και δυνατά φτερά.

Μοῦσαι Πιερίηθεν, ἀοιδῇσι κλείουσαι,
δεῦτε, Δί’ ἐννέπετε, σφέτερον πατέρ’ ὑμνείουσαι.
ὅν τε διὰ βροτοὶ ἄνδρες ὁμῶς ἄφατοί τε φατοί τε,
ῥητοί τ’ ἄρρητοί τε Διὸς μεγάλοιο ἕκητι.
ῥέα μὲν γὰρ βριάει, ῥέα δὲ βριάοντα χαλέπτει,
ῥεῖα δ’ ἀρίζηλον μινύθει καὶ ἄδηλον ἀέξει,
ῥεῖα δέ τ’ ἰθύνει σκολιὸν καὶ ἀγήνορα κάρφει
Ζεὺς ὑψιβρεμέτης, ὃς ὑπέρτατα δώματα ναίει.
κλῦθι ἰδὼν ἀίων τε, δίκῃ δ’ ἴθυνε θέμιστας τύνη.

List of abbreviations

1. **AEM** Anion Exchange Membrane
2. **BET** Isotherm of Adsorption, after Brunauer-Emmett-Teller
3. **BPM** Bipolar Membrane
4. **CB** Carbon Black (Acetylene Black) nanoparticles
5. **CEM** Cation Exchange Membrane
6. **CL** Catalyst Layer
7. **cp** co-precipitation
8. **cs** sequential precipitation
9. **ECR** Electrochemical CO_2 Reduction
10. **EDX** Energy Dispersive X-ray Spectroscopy
11. **EtOH** Ethanol
12. **EE**$_{CO}$ Energy Efficiency for CO
13. **FE** Faradaic Efficiency
14. **FE**$_i$ Faradaic Efficiency for a product i
15. **GDE** Gas Diffusion Electrode
16. **GDL** Gas Diffusion Layer
17. **GC** Gas Chromatography
18. **HPLC** High-Performance Liquid Chromatography
19. **HER** Hydrogen Evolution Reaction
20. **IPA** Isopropyl Alcohol
21. **ICP-OES** Inductively Coupled Plasma with Optical Emission Spectroscopy
22. **MEA** Membrane Electrode Assembly
23. **MPL** Micro Porous Layer
24. **NP** Nanoparticles
25. **NR** Nanorods
26. **NS** Nanosheets
27. **OD-Zn** Oxide Derived zinc
28. **OER** Oxygen Evolution Reaction
29. **PGMs** Platinum Group Metals
30. **PTFE** Polytetrafluoroethylene
31. **RDS** Rate Determining Step
32. **SACs** Single Atom Catalysts
33. **SEM** Scanning Electron Microscopy
34. **STP** Conditions of Standard Temperature and Pressure
35. **TEM** Transmission Electron Microscopy
36. **XPS** X-ray Photoelectron Spectroscopy
37. **XRD** X-ray Diffraction

List of symbols

1. **S** generic chemical species
2. **η** overpotential
3. **μ** chemical potential
4. **ν** stoichiometric factor
5. **ΔG** change of system’s free energy
6. **ΔH** change of system’s enthalpy
7. **α** activity and symmetry factor in Tafel-analysis
8. **K** equilibrium constant
9. **E** potential
10. **z** number of electrons
11. **T** temperature
12. **R** universal gas constant
13. **F** Faraday’s constant
14. **j** current density
15. **c** concentration of a species
16. **E_H** thermoneutral potential
17. **ΔS** change of system’s entropy
18. **D** diffusion coefficient

Chapter 1:
Introduction

1.1 Motivation

The escalating atmospheric concentration of CO_2 has triggered global concerns due to its direct impact on the greenhouse effect and the Earth's temperature. To address the increasing emissions, captured CO_2 is typically pressurized and stored underground. However, effectively utilizing CO_2 remains a substantial challenge, necessitating rigorous scientific research and practical industrial applications. Essentially, the conversion of CO_2 into valuable fuels or chemicals is commonly achieved through hydrogenation and electrochemical or photochemical reduction. The electrochemical CO_2 reduction, ECR, can follow diverse reduction pathways, ranging from 2- to 18-electron transfers, resulting in generating various gaseous and liquid products, as seen in Figure 1. The selectivity of products is intricately linked to the catalyst material chosen for the ECR. In recent years, ECR powered by renewable energy sources has garnered significant attention due to its remarkable energy efficiency of more than 30% at low operational temperatures between 25°C and 60°C. [1]

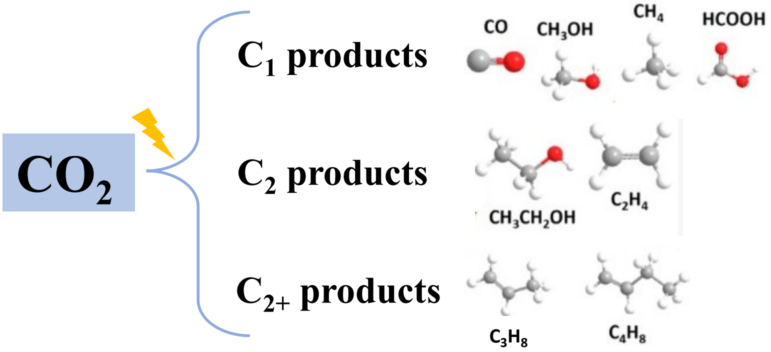

Figure 1.1. Graphical representation of the possible products that are possible to be formed through the electrochemical CO_2 reduction, ECR.

The plethora of products formed by the ECR leads to a complex reaction mechanism. The reaction pathway includes intermediate species, like $\bullet CO_2^-$, with high activation energies of about ~ 1 eV, introducing sluggish kinetics and high overpotentials η. [2–4] Various techno-economic studies suggested that carbon monoxide, CO, and formic acid, HCOOH, are the most viable products of the ECR. [5,6] Specifically, CO has a net present value of over 50 million $ and can be utilized as a useful intermediate for various products from the chemical industry. While CO, requiring 2 e^- for its formation, stands out as one of the most advantageous outputs attainable from the ECR. Due to the favorable ratio of its molecular weight, of 28.01 g mol^{-1}, per electron transferred for its formation. [5,7,8] CO generation through the ECR opens the door to a more decentralized CO production system, eliminating transportation risks and expenses. Nonetheless, to make the CO_2-to-CO commercially viable, three performance indicators should be sought after for the ECR electrolyzer: high current densities of $j > 0.5$ A cm^{-2}, low cell potential of 3 V or below ideally, and high Faradaic efficiency, FE_{CO}, higher than 80%. In the early 1990s, Hori et al. [9] classified the product selectivity of the different metals, namely group IVB-IVA for the ECR. His finding indicated that mainly platinum-group metals (PGM) like Ag, Au, Pd, Pt, tend to form CO. Despite the inherent CO selectivity of these metals, with FE_{CO} of about 87%, Hori et al. managed to record current densities below 10 mA cm^{-2}, owning to severe mass-transport limitations, stemming from the H-cell electrolyzer's architecture. To overcome this, the implementation of PGM catalysts on gas-diffusion electrodes (GDEs) in flow-cell and membrane electrode assembly (MEA) electrolyzers effectively countering the CO_2 mass-transfer limitations. Giving rise to high CO_2-to-CO reaction rates, with partial current densities for CO, j_{CO}, over 120 mA cm^{-2}.[10,11]

Despite their promising performance, PGM catalysts are known to introduce high Capital Expenditure (CAPEX) into the electrolyzer.[12] The efficient development of ECR electrolyzers requires the implementation of low-cost materials. PGM-free catalysts such as zinc, Zn, have exhibited promising performance in catalyzing the ECR to CO while maintaining low material cost.[13] Tuning properties like heteroatoms, grain-boundaries, oxygen vacancies of Zn and zinc oxide, ZnO, based materials have proven a successful way of actively converting CO_2-to-CO. The development of such materials does not only aspire to illustrate the practical application of the ECR but also elucidate vital mechanistic aspects of this process. [14,15]

1.2 Objective of this dissertation

This PhD thesis aims to advance the field of electrochemical CO_2 reduction, ECR, by developing innovative Zn-based catalysts in membrane electrode assemblies (MEAs) electrolyzers. By recognizing the potential of Zn-based materials as cost-effective catalysts for ECR, the objective is to harness their potential while addressing their limited stability of about ~40 h, for the electrocatalytic CO_2-to-CO conversion.

Feasible wet-chemical methods were employed to craft different catalysts, including structured ZnO, and to investigate the impact of morphology and the function of ZnO in ECR performance. By proposing a new operational strategy for the MEA, the aim was to prolong system durability without compromising CO selectivity, being held above 80%.

Heterostructured ZnO combined with various transition metal-oxides were fabricated to further improve ECR performance and gain insights into the role of ZnO and identify key parameters affecting catalyst durability.

Based on these findings, the structure and composition of the composite Zn-based oxide were optimized, and the new catalyst was applied in MEA electrolyzers. This led to a stable ECR, of more than 200 h, with high CO selectivity of 90%. The integration of the material in a large-scale MEA electrolyzer, with an active area of 100 cm^2, demonstrated equally stable and selective ECR.

In conclusion, this dissertation not only expands our understanding of efficient ECR catalysts but also lays the groundwork for sustainable and transformative electrochemical processes. Through meticulous exploration and innovation, this research contributes to advancing carbon-neutral chemical synthesis.

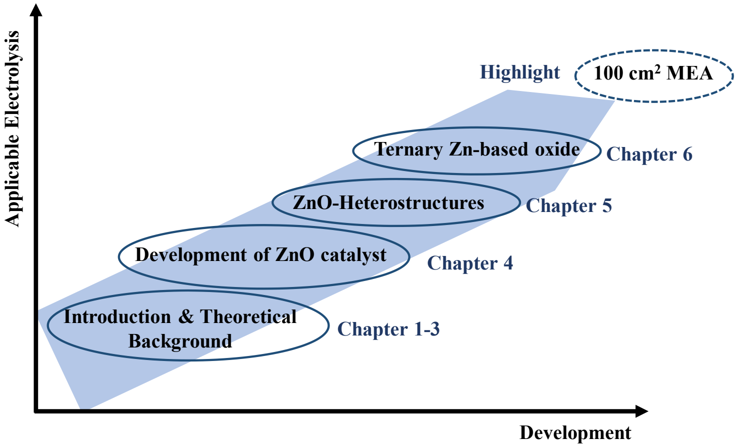

Figure 1.2. Graphical representation of the development process of the ECR electrolyzer in this dissertation.

1.3 Dissertation Overview

In **Chapter 2**, an introduction to the fundamental aspects of the ECR is given. This chapter provides an overview of the thermodynamics that govern this process, along with vital aspects of the reaction kinetics that steer the reaction's selectivity. Additionally, this chapter provides a thorough literature review of the state-of-the-art PGM-free catalysts and electrolyzer setup.

Chapter 3 provides an experimental insight into the different cell setups that have been used for the assessment of the ECR performance and the electrochemical characterization of the different catalysts. Insights into the experimental setup and the analytical techniques used are also provided. Details for the fabrication of the different catalysts and electrodes are also included.

Chapter 4 discusses the optimization of the ZnO properties by investigating the ECR performance of various ZnO-allotropes. This section introduces a novel way of efficiently tackling the initially limited stability of ZnO in the MEA.

Chapter 5 investigates the electrochemical behavior of various ZnO-metal heterostructures. The inter-phasal interactions of the binary Zn-metal oxides illuminate the potential of Zn-based heterostructures in augmenting material stability.

Chapter 6 forwards the concept with the creation and optimization of engineering metal/metal-oxide interfaces by fabricating a ternary Zn-Ce-Ag oxide. Showcasing the real application potential of the ECR.

Chapter 7 is a summary and discussion of the main results achieved in this dissertation.

In **Chapter 8,** the overall conclusions and outcomes of the thesis are laid out.

Chapter 2:
Fundamentals of CO_2 Electroreduction

In recent decades, there has been a surging interest in both the investigation and practical application of novel electrochemical processes, owing to their unique ability to convert electrical energy into chemical feedstock through electrolysis cells. Such processes become a valuable tool for harnessing surplus electrical energy to drive non-spontaneous reactions and as a means of electricity storage and supply. Furthermore, electrochemical procedures often offer notable advantages when compared to traditional thermochemical and thermo-catalytic reactions, particularly concerning their ability to provide relatively mild reaction conditions, typically at ambient pressure and temperature. [16]

One prominent example of the potential applications of electrochemical processes is the electrochemical reduction of CO_2, ECR, which holds great promise for efficiently converting atmospheric carbon into valuable products.

Despite its promising potential, the practical implementation of ECR presents significant challenges. The intricacy of the underlying reaction mechanisms, coupled with the high activation energies required for the involved reaction species, results in heightened energy demands. Additionally, the physicochemical properties of CO_2 and its interaction within the electrolyzer have a profound impact on the reaction kinetics and, consequently, product selectivity. Therefore, an overall understanding of the thermodynamic and kinetic principles governing ECR is imperative for addressing and overcoming the challenges it poses.[17]

2.1 Basic concepts of electrochemistry

Thermodynamics: In an electrolysis system, consisting of chemical species S, separated oxidation and reduction reactions take place under the application of external overpotential η. The reduction half-reaction ***eq. 2.1*** always takes place in the cathode, while the oxidation half-cell reaction ***eq. 2.2*** is always in the anode. The total reaction of the electrolyzer ***eq. 2.3*** is the sum of the half-reactions ***eq. 2.1*** and ***eq. 2.2***.

Cathode: $S_{ox,\,c} + ze^- \leftrightarrow S_{red,\,c}$ ***eq. 2.1***

Anode: $S_{red,\,a} \leftrightarrow S_{ox,\,a} + ze^-$ ***eq. 2.2***

Cell Reaction: $S_{ox,\,c} + S_{red,\,a} \leftrightarrow S_{ox,\,a} + S_{red,\,c}$ ***eq. 2.3***

Electrolysis is an endergonic process, with $\Delta G>0$, meaning that the application of an external load is necessary for the reaction ***eq. 2.3*** to happen. If no external potential is applied, the system is at equilibrium conditions, where $\Delta G=0$. The free enthalpy ΔG is composed of the sum of the chemical potentials μ_i multiplied by the respective stoichiometric factors of the species ν_i, described in ***eq. 2.4***. The change of the Gibbs free energy G. concerning the number of moles of a chemical species n, describes its chemical potential μ_i. The μ_i also depends on the activity a_i, of the system's species. This is described in ***eq. 2.5***. For the total reaction, the effect of each species a_i to the reaction direction can be assessed with the expression ***eq. 2.6***, depicting the equilibrium constant K. If the Faraday Law is solved for ΔG and equated with the initial ***eq. 2.4***, we have ***eq. 2.7***, describing the relation of the ΔG with the induced potential E, of an electrochemical process. Multiplying ***eq. 2.5*** with the ν_i we result in ***eq. 2.8***, which can also be expressed as ***eq. 2.9*** considering the ***eq. 2.7***. The ***eq. 2.9*** equation is the Nernst equation, describing the shifting of the equilibrium potential due to the influence of the activity of the chemical species.

$\Delta G = \sum_i \nu_i \mu_i$ ***eq. 2.4***

$\mu_i = \frac{\partial G}{\partial n} = \mu_i^o + RT\ln a_i$, where $R = 8.314\ J\ K^{-1}\ mol^{-1}$ ***eq. 2.5***

$K = \frac{[products]}{[educts]} = \Pi a_i^{\nu}$, where ν_i is the stoichiometric factor ***eq. 2.6***

$\Delta G = -zFE = \sum_i \nu_i \mu_i$, where $F = 96485\ C\ mol^{-1}$ ***eq. 2.7***

$\Delta G = \Delta G^o + RT \bullet \Sigma(\nu_i \ln a_i)$ ***eq. 2.8***

$E_N = E_{eq} = E^o - \frac{RT}{zF}\ln(\Pi a_i^{\nu i})$ ***eq. 2.9***

$E_{eq,\ tot.} = E_{eq,\ anode} - E_{eq,\ cathode}$ ***eq. 2.10***

For all variants that represent thermodynamic properties, the notation '^{o}' depicts the pre-defined thermodynamic property in STP conditions. The ***eq. 2.9*** applies both to the anodic and cathodic reaction of the electrolyzer and in extension to the total cell reaction, as dictated by the law of Hess ***eq. 2.10***.

Kinetics: The finite velocity at which these individual elementary steps occur results in an electrode surface polarization that extends beyond the equilibrium point of the reaction. This polarization serves as the driving force required to overcome the reaction-specific resistances, thereby initiating a net flow of electrons. A critical parameter, known as the overpotential η, is defined as the disparity between the electrode potential when a current is flowing and its equilibrium value ***eq. 2.11***. Overpotential η, is contingent on various factors, including the specific species involved in the reaction, the prevailing reaction conditions, and the characteristics of the electrode material.

$\eta = E - E_{eq}$ ***eq. 2.11***

At low polarization, the η is primarily dictated by the electron transfer process occurring during the rate-determining elementary step of an electrochemical reaction. This phenomenon is closely associated with the kinetic barriers that either hinder or facilitate this crucial step. It is fundamentally a consequence of the finite speed at which charge is transferred to a redox species. In situations where the rate-determining step of the reaction involves a one-electron transfer and other contributions are negligibly small, with $\eta \sim 0$, the current-voltage relationship can be effectively described by the well-known Butler-Volmer equation ***eq. 2.12***. This equation is significant in the realm of electrochemical kinetics and serves as a pivotal phenomenological tool, as it connects the η, thermodynamics, with the reaction rate and kinetics, through current j. It characterizes the extent of oxidative and reductive charge-transfer reactions, $j_{ct,ox}$ and $j_{ct,red}$ respectively, as defined in ***eq. 2.1*** and ***eq. 2.2***. It also illustrates the net flow of electrons e^- across the electrode surface, contingent on the charge-transfer overpotential η_{ct}, which represents the polarization solely attributed to the charge transfer. This equation is grounded in the theory of the activated complex, which examines changes in the ΔG along the reaction pathway for both forward and backward reactions. It reaches a peak when the activated complex, serving as the transitional state between reactants and products according to the theory, forms. In the context of electrochemical reactions, it considers alterations in the energy landscape for both forward and backward reactions, especially regarding shifts in potential differences between the electrode and electrolyte during electrode polarization. Consequently, it influences the modifications in the ΔG for the forward and backward reactions to varying degrees, leading to a preference for one direction over the other, with negative polarization favoring reduction and vice versa. [18,19]

$$j_{ct} = j_{ct,ox} + j_{red,ox} = j_o\ [\exp(\frac{azF}{RT}\eta_{ct}) - \exp(-\frac{(1-a)zF}{RT}\eta_{ct})],\ \text{where } 0>\alpha<1 \qquad \textbf{\textit{eq. 2.12}}$$

For ***eq. 2.12***, the exchange current density j_o, represents the current density at equilibrium, where $\eta=0$, being a tangible characteristic of the electrocatalysis system. The charge transfer coefficient or symmetry factor α, is derived from quantum mechanics [20], reflecting the extent to which the galvanic potential difference between the electrode and electrolyte, as described earlier, influences the change in activation energy. It essentially signifies how substantial electrode polarization impacts the reaction in either direction.

$$\eta_{ct} = \frac{2.303RT}{(1-a)zF}\log j_o - \frac{2.303RT}{(1-a)zF}\log j_{ct} = a - b\log j_{ct} \qquad \textbf{\textit{eq. 2.13}}$$

When the η_{ct} magnitude is significantly large, $|\eta_{ct}| >> \frac{RT}{zF}$, equal to 25.6/z mV at T=298 K, in the cathodic scenario, the oxidative current can be disregarded, and vice versa. In this case, the relationship simplifies to an exponential one. By rearranging the equation ***eq. 2.12***, replacing ln with log and solving for η_{ct}, we obtain what is commonly referred to as the Tafel equation ***eq. 2.13***. This equation incorporates the Tafel slope denoted as b, measured in mV/decade, and an additional constant α. For a rapid process, the movement of electroactive species to and from the electrode surface cannot keep pace with their consumption or generation, the reactants start to diminish, and the product accumulates within the double layer. Consequently, the actual concentration at the electrode surface, denoted as c_{surf}, deviates from the initial concentration c_o, to which E_o corresponds. Both concentrations are in equilibrium and, therefore the activities, given that there is no chemical gradient. However, with an increasing current density, this equilibrium would be disturbed, causing the activity to differ, leading to a change in the concentration equilibrium. This deviation results in the development of a concentration gradient between the bulk electrolyte and the electrode surface. To address this, the disparity in concentration must be considered in the electrode potential and is described by the concentration overpotential, represented as η_{conc}. Taking into account the concentration dependence of the standard potential using the Nernst equation, ***eq. 2.9***, we result into the ***eq. 2.14*** for cathodic currents. By solving the ***eq. 2.14*** for the overpotential, implicating the ***eq. 2.13***, we end up in ***eq. 2.15*** describing the concentration overpotential.

$$j_{red} = -j_o\frac{\text{Csurf}}{Co}\exp[-\frac{(1-a)zF}{RT}\ \eta] \qquad \textbf{\textit{eq. 2.14}}$$

$$\eta_{conc} = -\frac{RT}{(1-a)zF}\ln\frac{\text{Csurf}}{Co} \qquad \textbf{\textit{eq. 2.15}}$$

In technical electrode systems, especially when aiming for high current densities, the interplay between mass transport and its associated limitations assumes a crucial role. These concentration gradients, on the one hand, lead to substantial electrode polarization at elevated conversion levels and introduce a limiting current density, denoted as j_L, beyond which further polarization fails to augment the reaction rate. Additionally, in specific scenarios where various reactions compete for active sites influenced by distinct degrees of transport constraints, a shift in product distribution towards unwanted by-products, such as electrolyte decomposition, as seen through hydrogen production in aqueous CO_2 reduction, can be induced even before reaching this limiting current.

2.2 Thermodynamics of the CO_2 Electroreduction

During the ECR, CO_2 is reduced to produce valuable products, with the parallel reduction of H_2O, materialized through the H_2 evolution, HER. On the other hand, the anode is where the oxidation of H_2O occurs. The formation of various ECR products, as illustrated in Table 2.1, and their associated intermediates involves the transfer of differing numbers of electrons in each case. This results in a range of half-reaction potentials E_o. The CO_2 molecule's stable linear structure O=C=O, with a strong C=O bond of 750 kJ mol^{-1}, poses a significant barrier to its electrochemical conversion, leading to increased activation energy. [21] The formation of diverse ECR products involves several steps involving proton-electron transfers, which significantly influence E_o and energy demand. This is followed by a series of stepwise proton and/or electron transfers that lead to the creation of various end products, to be discussed in part 2.3. The presence of protons H^+, and the high E_o values associated with ECR product formation introduce the HER as a parasitic reaction in the system. This is due to the low potential for HER, 0 V vs. SHE, and the rapid kinetics of H_2 formation. [22,23] To mitigate the impact of HER, ECR is often conducted in an alkaline environment. [24]

Table 2.1. Half-reaction potentials of possible products of the ECR in aqueous solutions. [25]

Product	Equation	E_o (V vs SHE, 25°C)
Hydrogen	$2H^+ + 2e^- \rightarrow H_2$	0
ECR-Intermediate	$CO_2 + e^- \rightarrow \bullet CO_2^-$	-1.9
Carbon monoxide	$CO_2 + 2H^+ + 2e^- \rightarrow CO + H_2O$	-0.104
Formic acid	$CO_2 + 2H^+ + 2e^- \rightarrow HCOOH$	-0.171
Methanol	$CO_2 + 6H^+ + 6e^- \rightarrow CH_3OH + H_2O$	0.016
Methane	$CO_2 + 8H^+ + 8e^- \rightarrow CH_4 + 2H_2O$	0.169
Ethylene	$2CO_2 + 12H^+ + 12e^- \rightarrow C_2H_4 + 4H_2O$	0.085

In alkaline systems, the proton donor for the ECR is the H_2O molecules present. The mechanism of HER and OER also complies with the existing alkaline environment. The standard potential E_o and the reaction pathway of the reactions are dictated by the alkaline. The focus of this thesis remains the CO formation. The ***eq. 2.16–2.18*** describe the half-reactions that take place in an alkaline CO_2 electrolyzer at ambient conditions.[24,26] In the cathode, the ECR ***eq. 2.16*** takes place in parallel with the parasitic HER, ***eq. 2.17***. The anode reaction is the OER, ***eq. 2.18***, under alkaline conditions, fed by the crossing OH^-. Overall, the reaction that takes place in the electrolyzer is described by the ***eq. 2.19***.

Cathode: $CO_2 + H_2O + 2e^- \rightarrow CO + 2OH^-$, $E_o = -0.93$ (V vs SHE) ***eq. 2.16***

$2H_2O + 2e^- \rightarrow H_2 + 2OH^-$, $E_o = -0.83$ (V vs SHE) ***eq. 2.17***

Anode: $2OH^- \rightarrow \frac{1}{2} O_2 + H_2O + 2e^-$, $E_o = -0.4$ (V vs SHE) ***eq. 2.18***

Cell: $CO_2 \rightarrow CO + \frac{1}{2} O_2$, $E_o = 1.33$ V ***eq. 2.19***

The catalyst efficiency is assessed by its activation overpotential η_{act}, facilitating the formation of ECR intermediates, as seen in Figure 2.1a. The I-V response of the reaction consists of a standard polarization curve, expressing the rate of the reaction. Implementing the previously introduced term of overpotential η, bridging the thermodynamic foundations of the reaction with its rate. A standard polarization curve of the full-cell reduction reaction, ***eq. 2.19***, seen in Figure 2.1b, assumes no voltage losses from the cell components. The standard potential E^o of 1.33 V, for the reaction is derived from the ***eq. 2.7***. The thermoneutral potential E_H^o of 1.48 V, is calculated from the relation: $E_H^o = -\frac{\Delta H_o}{zF}$, for the standard enthalpy ΔH_o, of the ***eq. 2.19***. The difference between the E^o and E_H^o is a result of the entropy change, denoted through the term $T\Delta S^o$, within the overall process and necessitates the introduction or removal of heat from the system. As described by the fundamental relation: $\Delta G = \Delta H - T\Delta S$. When the entirety of the required heat is provided by Joule heating stemming from the flow of electric and ionic currents through internal resistances, this heat demand can be directly attributed to the supplied electrical energy. If an electrolyzer operates at 100% efficiency, denoted by an operational voltage of 1.46 V under standard conditions, the heat generated by the electrolyzer equals the heat required for the electrolysis process to proceed. Consequently, this scenario for the ECR achieves thermoneutrality, meaning the electrolyzer neither emits heat into the surroundings nor absorbs heat from the surroundings.[27] illustrates how the thermodynamic background of the reaction sets the guidelines for the kinetics.

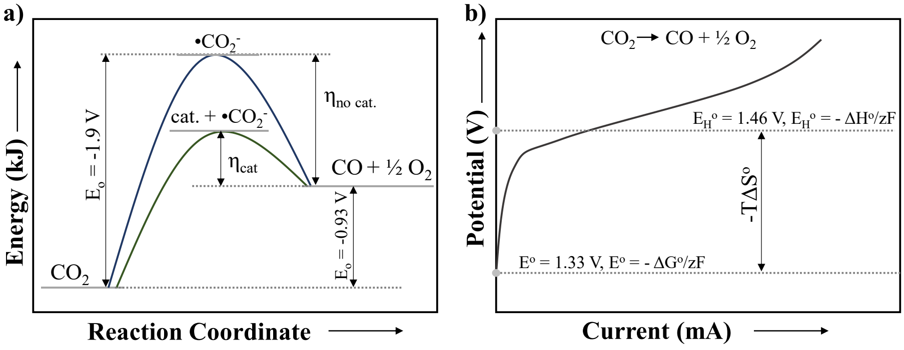

Figure 2.1. Thermodynamic breakdown of the ECR. a) Energy levels of the reaction species, b) Thermodynamic characteristics of the polarization curve for the full-cell reaction.

2.3 Kinetics of the CO_2 Electroreduction

Electroreduction is a complex, multi-stage process that encompasses the transfer of multiple electrons.[28,29,30] It involves several crucial steps, including CO_2 adsorption, electron transfer, and product desorption occurring at the electrode's surface. Extensive research has revealed that the current density, the specific electrochemical species involved, and the selectivity of the ECR are predominantly influenced by the choice of electrode material and the reduction potential applied. The initial step of the ECR is the diffusion of $CO_{2(g)}$ over the catalyst layer, followed by one e-transfer for the formation of the $\bullet CO_{2(ads)}^{-}$ intermediate, ***eq. 2.20***. The following protonation of the $\bullet CO_{2(ads)}^{-}$ ***eq. 2.21***, aided from the water molecule, is proposed to happen rapidly, forming the transition •COOH species. [31] A subsequent step involves both an electron and a proton transfer ***eq. 2.22***, forming the adsorbed $\bullet CO_{(ads)}$. Finally, the $\bullet CO_{(ads)}$ desorbs from the catalyst's surface, yielding the $CO_{(g)}$ ***eq. 2.23***. [32–34]

$CO_{2(g)} + \bullet + e^- \leftrightarrow \bullet CO_{2(ads)}^{-}$ ***eq. 2.20***

$\bullet CO_{2(ads)}^{-} + H_2O_{(l)} \leftrightarrow \bullet COOH_{(ads)} + OH^-$ ***eq. 2.21***

$\bullet COOH_{(ads)} + H^+ + e^- \leftrightarrow \bullet CO_{(ads)} + H_2O_{(l)}$ ***eq. 2.22***

$\bullet CO_{(ads)} \leftrightarrow CO_{(g)} + \bullet$ ***eq. 2.23***

The electrochemical CO_2 reduction, ECR, process follows the Eley-Rideal mechanism, where only one species undergoes adsorption.[35,36] Initial Tafel analysis data suggested that ***eq. 2.20*** and ***eq. 2.21***, could be the possible rate-determining steps (RDS) for ECR. However, recent work by Deng et al.[37] has shown that the RDS for CO formation is equation ***eq. 2.20***, while the RDS is independent of the pH. The ***eq. 2.20*** is a composite step that encompasses the crucial processes of $CO_{2(g)}$ diffusion over the catalyst layer and electron transfer. At lower current densities, the rate of electron transfer in ***eq. 2.20*** is the critical factor influencing the rate of ECR. At higher levels of polarization, of more than 200 mA cm^{-2}, the diffusion of $CO_{2(g)}$, as seen in ***eq. 2.20***, toward the active surface of the catalyst becomes the limiting factor for the ECR rate. Given the strong correlation between the catalyst's properties and the ECR performance, the Sabatier principle emerges as a crucial tool for predicting a catalyst's activity and product selectivity.[38] It asserts that for high catalytic activity, the interactions between the catalyst and the reaction species should exhibit an intermediate intensity, for the reaction to be favored. Figure 2.2a depicts a common volcano plot illustrating the activity versus the binding strength of CO, providing a useful visualization of the Sabatier principle for the ECR.[39,40] Where an optimal catalyst exhibits properties that reside at the peak of the volcano plot.

The parasitic hydrogen evolution reaction, HER, progresses at the cathode in parallel with the ECR. The generally accepted HER mechanism in alkaline and neutral media is exhibited below:

$H_2O + e^- \leftrightarrow H_{ads} + OH^-$, (Volmer step) ***eq. 2.24***

$H_{ads} + H_2O + e^- \leftrightarrow H_2 + OH^-$, (Heyrovsky step) ***eq. 2.25***

$2H_{ads} \leftrightarrow H_2$, (Tafel step) ***eq. 2.26***

The splitting of a water molecule and the adsorption of hydrogen on the surface of the electrode or catalyst is described by the Volmer step, ***eq. 2.24***, which always consists of the initial step of the HER. This is then followed by the production of hydrogen through either an electrochemical process, Heyrovsky step, ***eq. 2.25***, or a chemical process as in a Tafel step, ***eq. 2.26***. Numerous studies have exhibited that at low η, lower than -0.15 V, the HER goes through the Heyrovsky step, while the Tafel step follows in parallel. However, at high η, of more than -0.25 V, the electrode is considered overwhelmed by H_{ads}. The Tafel step becomes negligible, with the HER progressing through the Heyrovsky step, owing to its high rate constant.[41–43] Figure 2.2b summarizes in a volcano plot the tendency of various materials in catalyzing the ECR. The low thermodynamic potential of the HER, summarized in Table 2.1, and its faster overall kinetics, seen in Figure 2.2 a&b, strongly favor the reaction at the expense of ECR.

At lower polarization, the reactions' kinetics are majorly determined by the e-transfer. The function of a selective and efficient catalyst for the ECR is to successfully redirect the majority of the total current of the electrolyzer toward the ECR instead of the HER. It is worth noting that at a high current density of more than 300 mA cm^{-2}, both the ECR, ***eq. 2.23***, and HER, ***eq. 2.25***, rates are primarily governed by species desorption, with additional limitations imposed by mass transfer of the reactants. Considering the significantly higher diffusion coefficient of H_2, D_{H2}, compared to the CO_2 one, D_{CO2}, and CO one, D_{CO}[44], the faster mass transfer of the H_2 will inevitably favor the HER at high current densities. The polarization curves in Figure 2.2c provide a qualitative representation of the theoretical behavior of the parallel reactions. At lower reaction rates, ECR is favored by the catalyst's active centers so that the partial current density for the ECR, j_{CO}, is always larger than that for HER, j_{H2}. While at higher currents due to the effect of mass-transfer limitations on the reactions' species, HER takes over imposing the opposite condition.[45–47]

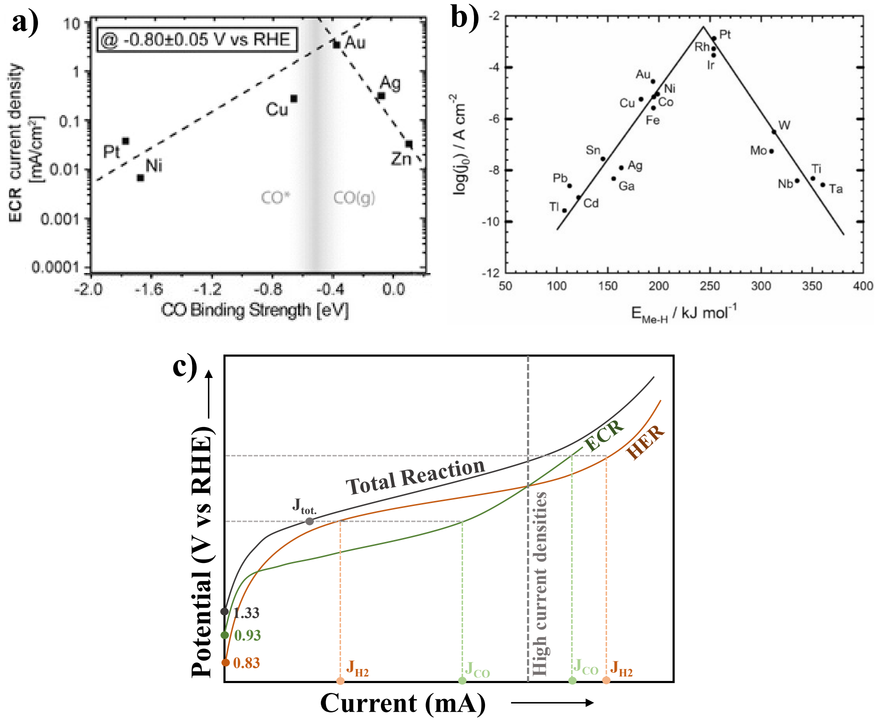

Figure 2.2. Catalyst properties and kinetic brake-down of the cathode reaction. a) Volcano plot of various materials for their ECR affinity, adopted from [40], b) Volcano plot of various materials for their HER affinity, adopted from [41], c) Qualitative deconvolution of the total cathodic polarization curve into the ECR and HER.

In examining the two cathodic reactions, ECR ***eq. 2.16*** and the parasitic HER ***eq. 2.17***, three key figures of merit determine the preference for either ECR or HER. The Faradaic Efficiency, FE, described in ***eq. 2.27***, quantifies the ratio of the theoretically calculated charge spent on product formation Q_{th}, calculated by the total charge passed, to the actual amount Q_{pr}, quantified by analytical techniques, see Chapter 3. The partial current density j_i signifies the rate of product formation, derived from the total current density flowing through the electrolyzer j and the FE for the specific product formation, described in ***eq. 2.28***. Evaluating the viability of the reaction, the energy efficiency, EE, of the electrolyzer for a specific product, ***eq. 2.29***, offers valuable insights. It articulates the thermodynamic efficiency of product formation, as expressed through the relation $\frac{\text{Eo}}{\text{Ecell}}$, relative to its kinetic efficiency FE.

$$\text{FE (\%)} = \frac{Qpr}{Qth} \qquad \textbf{\textit{eq. 2.27}}$$

$$j_i = j*\text{FE} \qquad \textbf{\textit{eq. 2.28}}$$

$$\text{EE (\%)} = \frac{\text{Eo}}{\text{Ecell}}\,\text{FE} \qquad \textbf{\textit{eq. 2.29}}$$

2.4 State-of-the-art Catalysts

The techno-economic advantages of the electrochemical CO_2-to-CO reduction have driven significant research into catalyst development for selective CO production.[48] Platinum-group metals (PGMs), known for their inherent selectivity in CO generation, have played a pivotal role in advancing the understanding of electrochemical reduction (ECR) understanding.[49–53] Chen et al.[54] achieved FE_{CO} of 96% at -0.35 V_{RHE} over 8 h, using Au in an H-cell. Their work illustrated how Au can facilitate the initial e-transfer by stabilizing the •COOH intermediate. Follow-up works exhibited similarly good ECR performance CO formation overpotential for Ag[55] and Pd[53] based materials. However, H-cell architecture introduced mass-transfer limitations, restricting partial current density for CO j_{CO}, of about ~50 mA cm^{-2}. [56–58] Using gas-diffusion electrodes (GDEs) in flow cells and membrane-electrode-assemblies (MEAs) electrolyzers, j_{CO} was recorded in the range of several hundreds of milliamperes.[59–61] The early work of Yamamoto et al.[62] exhibited the advantages of integrating Ag catalyst in such a system, recording a maximum partial j_{CO} of 100 mA cm^{-2}. Dinh et al.[63] incorporated an Ag layer over a PTFE membrane creating a stable GDE that delivered j_{CO} of 150 mA cm^{-2} for 100 h. Exhibiting the potential for stable electrolysis upon modulating the properties of the GDE. Monteiro et al.[64] recorded similar ECR performance using Au in low pH electrolytes, addressing the challenging aspect of acidic ECR. Oden et al.[11] exploited the synergistic effects of Ag and Au in a composite catalyst, recording a high rate of CO formation at j_{CO} of 180 mA cm^{-2}.

In light of the exceptional properties of noble metals, their scarcity and high cost have spurred the exploration of alternative materials. [162–164] Molecular and single-atom catalysts (SACs) have recently emerged as promising ECR catalysts.[65] Robert et al. [66] first exhibited the application potential of Co-based molecular catalyst recording high j_{CO} of 160 mA cm^{-2}.[67] In the same context, Nam et al.[68] developed Ni-SACs recording an equally high j_{CO}.[69] Despite the promising performance of these materials, their tedious synthesis procedure and limited stability, less than 10 h of ECR, pose challenges for their practical implementation. [70]

Zinc, Zn, a low-cost material, holds promise as a viable alternative to noble metals due to its widespread availability and inherent inclination for CO production.[71] However, the efficiency and selectivity of Zn in CO generation lag behind those observed with Au and Ag catalysts.[72] Various strategies have emerged to address these limitations, including creating high surface area [73,74], selective facets, and favorable morphology [75–77], all of which enhance the performance of Zn and ZnO-based materials in ECR.[78] Nanostructured metallic Zn demonstrates elevated catalytic activity and enhanced CO selectivity.[13,79,80] As shown by Luo et al.[81] demonstrated that highly porous Zn electrodes fabricated via electrochemical methods, integrated into a flow cell electrolyzer, achieved a j_{CO} of 160 mA cm^{-2} from the GDEs.[82] The same group developed oxide-derived Zn, OD-Zn, gas diffusion electrodes (GDEs), regulating the morphology and oxidation state of the catalyst to achieve a high j_{CO} of 180 mA cm^{-2} while enhancing catalytic activity.[83,84] Despite the promising performance of metallic Zn, studies indicate that ECR activity primarily originates from Zn^{+2} oxidation in the zinc oxide, ZnO, phase.[85–87] ZnO has proven to be a selective ECR catalyst in flow cell electrolyzers, exhibiting a CO faradaic efficiency FE_{CO} of over 80% and a j_{CO} of 100 mA cm^{-2}.[88,89] Optimizing the structure and properties of ZnO further enhances FE_{CO}

and j_{CO}, as demonstrated by late work by Zong et al.[75] The morphology of ZnO significantly influences its hydrophobicity [160], a critical attribute for gas diffusion electrodes employed in ECR.[90–95] Modulating and stabilizing the Zn^{+2} state is crucial [173] for electrocatalytic functions of ZnO-catalysts and promoting their activity for the ECR.[87,86] Despite the high reduction overpotential of ECR leading to partial reduction of ZnO to metallic Zn, [83,96,97] numerous studies underscore the potential of ZnO as an ECR catalyst. [98,82] As demonstrated by Stamatelos et.al [99], elaborated in Chapter 4., ZnO with an optimized morphology was integrated into a MEA, achieving FE_{CO} above 80% for over 100 h at high current densities, facilitated by a developed *in-situ* ZnO-phase regeneration protocol. Highlight the potential of ZnO-based materials as efficient catalysts across a wide range of ECR electrolyzers.[100,88,75,81]

Engineering Zn-based metal/metal-oxide heterostructures[101,102,103] is a promising strategy for developing catalysts with higher ECR activity.[104–106] Oxide-based materials are known to promote the ECR through the ‘direct-effect mechanism’ by lowering the activation potential for the formation of the intermediates.[107,108] Such heterostructures are known to exhibit varied electrocatalytic properties[109,110], dependent on the nature and properties of the different phases[111–113] of the composite catalyst material. [114–122] As shown by Luo et al.[123] a composite Cu-Zn catalyst could selectively catalyze the ECR with a FE_{CO} of 94% by lowering the activation barrier for the •COOH intermediate.[124] Moving beyond metallic heterostructures, Chen et al.[125,126] utilized various metal/ZnO interfaces that achieved equally high FE_{CO} in MEA electrolyzers. Their catalyst architecture induced e-delocalization, energetically favoring the CO formation path. Metal/metal-oxide heterostructures [127,128] provide a larger surface area for the ECR, with various interactions among the phases[129], that as shown by Stamatelos et.al[130] in Chapter 5., favor the catalyst’s activity and stability during continuous electrolysis. With the stability and selectivity creating a major ‘bottleneck’ towards applicable ECR, oxide-based catalyst substrates[227–231] hold potential for further enhancing the ECR activity by stabilizing the reaction’s intermediates and providing stable catalyst structures.[131–138] As such, heterostructures containing cerium oxide, CeO_2[139,140,141,142] have exhibited significant ECR activity, with electrocatalytic properties directly stemming from the various interactions of the heterostructure’s interphase.[143,144] Such inter-phasal interactions were illustrated by Zong et al.[145], using a heterostructured ZnO/CeO_2 catalyst that achieved an FE_{CO} of 90%. Proposing a Zn-O-Ce model of interactions, that stabilized the oxidation state for Zn^{+2}, favoring its ECR activity and suppressing HER. In the latest work of Stamatelos et.al[146], illustrated in Chapter 6., ternary oxide Zn–Ce–Ag catalysts were developed for practical CO_2-to-CO conversion, achieving a FE_{CO} of 90% at 200 mA cm^{-2} for 200 hours in a large-scale MEA electrolyzer with a 100 cm^2 active area. With the enhanced performance being attributed to CeO_2 stabilizing the ZnO phase, preventing agglomeration of the ECR-active sites.

Addressing the challenges in Zn-based catalysts for the ECR involves several key aspects regarding the catalysts’ robustness.[147,148] Catalyst stability is crucial for commercial applications, but current Zn-based catalysts often have a short lifespan, less than 40 h, for industrially relevant j_{CO} of more than 120 mA cm^{-2}, as exhibited in Figure 2.3. Investigating degradation mechanisms and exploring solutions, such as anchoring on specific substrates, is essential for improving stability. Lastly, the practical application of ECR faces hurdles like complex electron transfer, multiple pathways, and low CO_2 diffusion rates. Rational electrocatalyst design is necessary to overcome these challenges and enhance the efficiency of ECR while promoting a rational catalyst lifespan of more than 100 h.

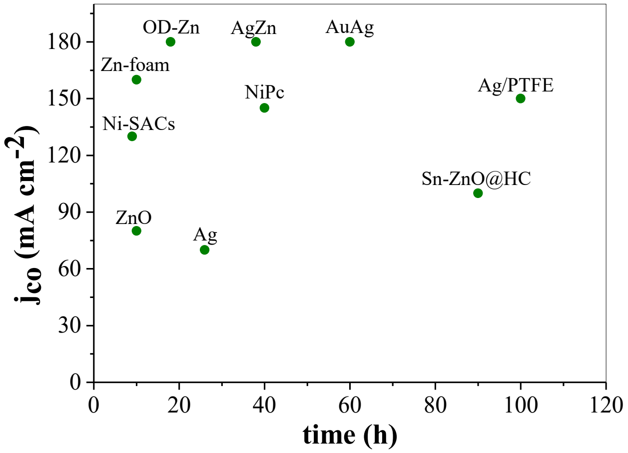

Figure 2.3. Graphical depiction illustrating the ECR efficiency, with a focus on j_{CO} and stability for both PGM and Zn-based catalysts. These catalysts were implemented in flow cells and MEA electrolyzers. The chart incorporates the latest performance data extracted from the literature, as referenced in sub-chapter 2.4.

2.5 Membrane Electrode Assembly

Membrane-electrode assemblies (MEAs), alternatively referred to as "zero-gap," "catholyte-free," or "gas-phase electrolysis," offers an effective approach to tackle the challenges associated with aqueous Gas Diffusion Electrode (GDE). The MEA design, commonly employed in fuel cells and water electrolyzers, has proven to be a widely utilized solution in electrochemical cells.[149] In a typical MEA system, gaseous humidified, at room temperature, CO_2 is directly supplied to the cathode. Usually, the oxygen evolution reaction OER, serves as the counterpart oxidation reaction at the anode.[150] The cathode and anode are tightly pressed to the two sides of a polymer electrolyte membrane, facilitating ion transfer while preventing product crossover. The cathode, membrane, and anode constitute the core components of the MEA electrolyzer architecture, as seen in Figure 2.4.[151]

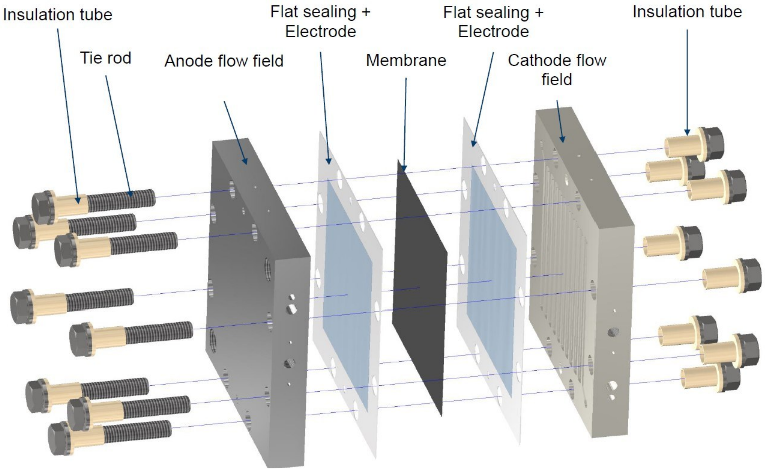

Figure 2.4. Schematic of the architecture and the components of an MEA electrolyzer. The drawings are representative of the MEA cell used for this work, as well as corresponding to the generally accepted MEA architecture.

End-Plates: The MEA's end-plates not only function as the cell's housing but also serve as the current collector. Constructed from Ti due to its favorable mechanical properties and stability at high overpotential, these end-plates play a crucial role.[152] For both the anode and cathode end plates, the distribution of the reagent stream is guided by the flow pattern engraved on the current collectors. While different flow patterns are viable, the meander pattern is the most prevalent. This design ensures the uniform distribution of streams over the electrodes, promoting consistent performance.[153,154]

Gas-Diffusion Electrodes (GDEs): GDEs present advantages over conventional planar electrodes, facilitating higher local concentrations of CO_2 and mitigating mass transport resistances. This leads to an accelerated reaction rate and an enhanced current density in Efficient Carbon Reduction, ECR, processes.[155] Typically, a GDE consists of a gas diffusion layer (GDL), a microporous layer (MPL), and the catalyst layer (CL) on top. The GDE operates by allowing CO_2 gas to diffuse through the GDL and MPL to reach the CL, where ECR occurs. Studies show that electrolysis using GDEs markedly improves reaction rates compared to traditional porous electrodes, effectively reducing the diffusion length of CO_2.[156] The GDL is commonly crafted from carbon fibers, while the MPL comprises of small carbon nanoparticles, of about ~20 nm diameter, that provoke a more even distribution of the CO_2 stream to the CL. Both the GDL and MPL undergo polytetrafluoroethylene (PTFE) treatment during manufacturing, ensuring crucial hydrophobicity[197] for optimal ECR performance. [157,158] The catalyst layer is prepared by depositing the catalytically active phase onto the MPL.[159] Among various commercial GDE types, the Freudenberg H23C6 stands out as one of the most effective and is utilized for this thesis.[160]

Ion exchange membrane: The membrane plays a crucial role as the ionic bridge between the anode and cathode, ensuring ionic contact and preventing the migration of ECR products to the anode, thus avoiding their re-oxidation in CO_2. There are three main types of membranes: anion exchange membrane (AEM), cation exchange membrane (CEM), and bipolar membrane (BPM). The choice of membrane type allows for the modulation of the local reaction microenvironment, influencing factors such as pH and reactant concentration, as mass transfer characteristics differ among membranes.[161] CEMs introduce an acidic environment, due to H^+ crossover, potentially promoting the HER. BPMs, composed of a laminated CEM and AEM, show promise for utilizing low-cost anode catalysts but introduce high overpotential due to their thickness of 250 µm.[162] AEMs exclusively permit the passage of anions like OH^-, CO_3^{-2}, effectively impeding the transport of other species and promoting an alkaline environment that suppresses the HER.[163,164] Consequently, AEMs are the most commonly used membranes in ECR electrolyzers. Among various membranes, Sustainion has emerged as the most commonly used and commercially available option.[165] Despite the growing research and development in AEMs, Sustainion is the membrane adopted by the majority of research groups.[163,166,167] Therefore, for this thesis, the Sustainion AEM, Sustainion® X37-50, was selected.

Anode: In this context, the predominant anodic reaction is the oxygen evolution reaction OER, facilitated by the Ir/IrO_x catalyst. The acknowledged mechanism and stability of both the OER and Ir-catalyst strategically position it as a favorable counter-reaction, allowing us to focus specifically on the challenging aspects of ECR.[168–170]

Chapter 3:
Experimental Methods

3.1 Introduction

The electrochemical reduction of CO_2, ECR, stands as a promising avenue for generating valuable products. However, the intricate nature of this process poses significant experimental challenges, demanding the utmost precision. The successful development and optimization of novel ECR catalysts rely not only on their accurate synthesis and characterization but also on the meticulous assessment of their performance in CO_2 reduction. This chapter elucidates the synthesis methodologies employed for crafting various catalyst materials and offers a comprehensive breakdown of the electrochemical techniques utilized for catalyst characterization.

At the heart of evaluating catalyst electrochemical traits lies the utilization of fundamental electrolyzer systems, such as the H-cell configuration. In contrast to extensively studied electrolysis mechanisms like the hydrogen evolution reaction, HER, or oxygen evolution reaction, OER, ECR leads to a diverse array of carbon C, oxygen O_2, and hydrogen H_2 containing products. Addressing mass-transport limitations and striving for enhanced reaction rates, gas-diffusion electrodes (GDEs) are harnessed and integrated into Flow-Cell or Membrane Electrode Assembly (MEA) electrolyzers.

Significantly, the selectivity of the products heavily depends on reaction rates, rendering the assessment of ECR performance beyond the scope of a conventional cyclic voltammogram (CV).[171] For this reason, the ECR performance of each material is determined at each current density separately. Product quantification is carried out using in-line gas chromatography (GC) and liquid chromatography (LC).[172,173]

The subsequent sections will delve into the specificities of each synthesis method, providing insights into their intricacies. The chapter will also meticulously detail the application of diverse electrochemical methods and their significance in unraveling the characteristics of the catalysts under scrutiny. Through this rigorous approach, the true potential of novel ECR catalysts emerges, contributing to the advancements in sustainable electrochemical processes.

3.2 Catalyst Synthesis

The synthesis of the different Zn-oxides was performed through facile wet-chemical techniques, at room temperature. The fabrication of the heterostructures binary and ternary Zn-based oxides followed the same synthesis path, employing a common precipitation method for the attachment of the add-phase.

3.2.1 Materials & Chemicals

Zinc nitrate hexahydrate $Zn(NO_3)_2{\cdot}6H_2O$ grade 99.99%, copper nitrate $Cu(NO_3)_2{\cdot}3H2O$, grade 99.99%, nickel nitrate $Ni(NO_3)_2{\cdot}6H2O$ grade 99.99%, cobalt nitrate $Co(NO_3)_2{\cdot}6H2O$ grade 99.99%, iron nitrate $Fe(NO_3)_2{\cdot}6H2O$ grade 99.99%, potassium hydroxide KOH grade 99%, zinc acetate $Zn(OCH_3)_2$ grade 99.99%, ethanol anhydrous, sodium perchlorate $NaClO_4$ grade 99.999%, potassium bicarbonate $KHCO_3$ grade 99%, silver nitrate $AgNO_3$ grade 99.99% and cerium sulfate anhydrous $Ce(SO_4)_2$ grade 99.99% were purchased from Sigma-Aldrich and used without further purification. Urea CH_4N_2O grade 99.99%, Iridium/Iridium Oxide nano-powder IrO_x, nanopowder grade 99.99%, silver nanopowder grade 99.99%, 20-40 nm were purchased from Alfa-Aesar and used without any purification. Demineralized MiliQ water. Carbon Paper Freudenberg H23C6, titanium fibers porous transport layer, Ti-

PTL, 500 μm thickness, Nafion dispersion 5 % wt/wt, alcohol-based, Ni-foam of 500 μm thickness, and Carbon Black Cabot Vulcan XC-72 were purchased from Fuel-Cell Store. Sustainion Membrane X37-50 grade RT, of 50 μm thickness was purchased from Dioxide Materials.

3.2.2 ZnO Allotropes

ZnO nanoparticles, NP. A 50 ml solution of 0.2 M $Zn(NO_3)_2$ was prepared. To that solution, 50 ml of 0.4 M KOH was added dropwise, under a stirring condition until the end of the process. The precipitant was collected via centrifugation and washed 3 times with MilliQ water and 1 time with ethanol. The obtained product was dried overnight at 70 °C, and calcined for 3 h at 500 °C, to form the crystalline phase of ZnO. The ZnO with random shape RS, was prepared using a similar procedure except for the addition of 50 ml of 1 M KOH instead of 0.4 M KOH. [174]

ZnO nanosheets, NS. Typically, 50 ml of 0.2 M zinc acetate $Zn(OCH_3)_2$ were added dropwise in a 50 ml solution of 0.4 M CH_4N_2O. The mixture was then refluxed at 90 °C for 2 h. The precipitant was washed collected and washed 3 times with water and 1 time with ethanol. The obtained product was dried overnight at 70 °C, and afterward calcined for 2 h at 400 °C, to form the crystalline phase of ZnO in the nanosheet morphology. [175]

ZnO nanorods, NR. In a typical synthesis, 0.89 g of $Zn(NO_3)$ and 0.54 g of urea CH_4N_2O were dissolved in a 100 ml mixture of water and ethanol, 80 ml/20 ml. To this mixture, 0.1 M of HNO_3 was added, until the pH was adjusted between 2.0-3.0. The resulting solution was boiled and refluxed for 8 h in a round-bottom flask. The resulting precipitant was collected and washed 3 times with water and 1 time with ethanol. The powder was dried overnight at 70 °C. High-temperature calcination is not needed since the allotrope powder is already crystalline. [176]

3.2.3 ZnO@Transition Metal Oxides

The polymeric precursor method was used to synthesize the ZnO samples. Briefly, $Zn(NO_3)_2$ was dissolved under constant stirring, followed by the formation of a polymer resin at 80°C. The polymeric resin formation occurs due to the addition of ethylene glycol and citric acid, 3:2 mass ratio, to the solution containing the metal ion Zn^{+2}. After polymeric precursor preparation, it was pre-calcined at 300°C for 2 hours. The material formed was ground in an agate mortar for particle homogenization and re-calcined at 500°C for 2 hours. The heterostructures were synthesized from the method described above. However, during the polymeric precursor formation step, a certain amount of $Cu(NO_3)_2$, $Cu(NO_3)_2$, $Co(NO_3)_2$ and $Fe(NO_3)_2$ precursor was added to form Zn/Cu, Zn/Ni, Zn/Co and Zn/Fe heterostructures in the 80/20 molar ratio of Zn:M, where Zn represents the zinc and Cu, Ni, Co, Fe, represents the presence of the respective transition metals.

3.2.4 ZnCeAg Ternary Oxide

CeO_2 nanoparticles, CeO_2-np. A 50 ml aqueous solution of 0.2 M $Ce(SO_4)_2$ was prepared, to which a solution of 0.5 M KOH was added dropwise, with a rate of 1 ml min^{-1}, under stirring conditions, until a pH value of 9 was reached. The precipitate was then collected via centrifugation and washed three times with MilliQ water and once with ethanol. The obtained product was then dried overnight at 70 °C, and calcined for 3 h at 500 °C under a static air atmosphere to form crystalline CeO_2.

cpZnCeX nanoparticles. A 50 ml aqueous solution with the appropriate molar ratios of $Ce(SO_4)_2$ and $Zn(NO_3)_2$ was prepared. The total molar amount of the precursors was constant at 0.1 moles. X refers to the content of Ce. We varied the amount of Ce [X= 5, 10, and 20 (%)]. To that mixture, a solution of 0.5 M KOH was added dropwise with a 1 ml min^{-1} rate, under stirring conditions, until a pH value of 9 was achieved. The precipitant was then collected via centrifugation and washed three times with MilliQ water and once with ethanol. The obtained product was dried overnight at 70 °C, and calcined for 3 h at 500 °C under a static air atmosphere to form the crystalline phases of the material.

csZnCeX nanoparticles. A 50 ml aqueous solution with the appropriate amount of core CeO_2–np and $Zn(NO_3)_2$ was prepared. This was then placed in a sonication bath for 60 min to form a uniform dispersion. The total molar amount of the precursors was constant at 0.1 moles. X refers to the content of Ce. We varied the amount of Ce [X= 5, 10, and 20 (%)]. To that dispersion, a solution of 0.5 M KOH was added dropwise with a rate of 1 ml min^{-1}, under stirring conditions, until a pH value of 9–10 was reached. The precipitant was collected via centrifugation and washed three times with MilliQ water and once with ethanol. The obtained product was dried overnight at 70 °C and calcined for 3 h at 500 °C under a static air atmosphere to form the crystalline phases of ZnO.

Ag@cpZnCe10 nanoparticles. A 50 ml aqueous solution with 100 mg of cpZnCe10 nanoparticles and 40 mg of $AgNO_3$ was prepared. For the material optimization, we varied the Ag quantity by altering the amount of $AgNO_3$ precursor. The dispersion was then placed in a sonication bath for 60 min to form a uniform dispersion. To this, a solution of 0.25 M KOH was added dropwise, with a rate of 1 ml min^{-1}, under stirring conditions, until a pH value of 9–10 was achieved. The precipitant was collected via centrifugation and washed three times with MilliQ water and once with ethanol. The obtained product was dried overnight at 70 °C, and afterwards calcined for 2 h at 250 °C under a static air atmosphere.

Ag@csZnCe10 nanoparticles. The synthesis of this material followed the same process as outlined above for the synthesis of the Ag@cpZnCeX nanoparticles. Instead of the precursor solution, cpZnCeX nanoparticles were used as the core material.

Ag@ZnO. In a typical synthesis, 100 mg of ZnO–np and $AgNO_3$ were dispersed in 50 ml of water, for 60 min in a sonication bath. In the dispersion, 0.25 M of KOH was added dropwise,at a rate of 1 ml min^{-1}, under stirring conditions, until a pH value of 9–10 was reached. We varied the $AgNO_3$ amount to achieve an Ag-doping of: 5, 10, and 15%. The precipitant was collected via centrifugation and washed three times with MilliQ water and once with ethanol. The obtained product was dried overnight at 70 °C, and calcined for 2 h at 250 °C under a static air atmosphere.

3.3 Catalyst Characterization

X-ray Diffractogram (XRD)

The crystalline phase of the pristine catalysts and the prepared GDEs were characterized by X-ray diffraction (XRD) using CuKα radiation in the 2θ range from 25 to 100°, employing a Shimadzu XRD-6000 diffractometer. [186–188]

X-ray Photoelectron Spectroscopy (XPS)

The surface compositions of the prepared catalysts were analyzed using X-ray photoelectron spectroscopy (XPS) Phi5000 VersaProbeII, ULVAC-Phi Inc., USA. The radiation source was Al K-alpha, monochromatic 1.486 keV, with X-ray setting: 50W, 15kV, 200µm spot. The survey spectra were obtained by applying 187.5 eV pass energy, 0.8 eV step, 100 ms/step, and the detailed spectra by applying 23.5 eV pass energy, 0.1 eV step, 100 ms/step. [177]

Electron Microscopy

The morphology of the catalyst powders and GDEs was observed with a scanning electron microscope (SEM). For this purpose, the Zeiss 1550 VP SEM was used with a Gemini column, at up to 30 keV. TEM and HRTEM measurements were conducted with a Philips CM 200 field emission gun. The accelerating voltage was 200 kV. To achieve "Z-contrast" conditions, a probe semi-angle of 25 mrad was used, with the detector having a 70 mrad inner collection angle.

Hydrophobicity

The inherent hydrophobicity of the catalyst layer was assessed with a Kruss DSA25 Drop Shape Analyzer. For the measurement 10 µl of MilliQ water was dropped on the catalyst layer. The measurement of the contact angle was done under static conditions (Cassie-Baxter).

Inductively Coupled Plasma Optical Emission Spectroscopy (ICP-OES)

The elemental composition of every catalyst material was investigated using inductively coupled plasma with optical emission spectroscopy (ICP-OES). The probes were dissolved in dilute nitric, HNO_3, acid and analyzed via ICP–OES iCAP 7600.

Raman spectroscopy

More details regarding the coordination and structure[127,178,179] of the materials were provided by Raman spectroscopy. [180–182] For that purpose, an iXR Raman Spectrometer (Thermo-Fisher Scientific) was used. The technique was applied to the powder form of the catalysts. The excitation wavelength of the laser was 600 nm. [223–227]

Brunauer-Emmett-Teller (BET)

The nitrogen (N_2) adsorption-desorption isotherm and the specific surface area (SSA) values calculated according to the Brunauer-Emmett-Teller (BET) method, were obtained at -196°C with a Micromeritics ASAP-2020 system. Before the analysis, the samples were thermally treated, degassed, at 80°C under a vacuum.

3.4 Electrodes Fabrication

All of the cathode gas diffusion electrodes (GDEs) were prepared on a Freudenberg H23C6 carbon paper with a microporous layer using an automatic spray-coating machine Sono-Tek, ExactaCoat. The ink was composed of 120 mg of catalyst powder, 30 mg of carbon black, 12 ml of isopropanol, 7.5 ml of Milli-Q water, and 158.3 μl of Nafion solution of 5% wt/wt. The ink was placed under Ultra-Turex at 33,000 rpm for 10 min and subsequently into a sonication ice bath for 60 min. The same ink recipe, in terms of the content of the solids and solvents ratio, was also used for the preparation of every other catalyst ink cited in this work. All of the catalyst-loaded cathode GDEs featured a loading of 1 mg cm^{-2}. After preparation, all of the different GDEs prepared were dried at 70 °C for 3 h. This mild heat treatment was intended to evaporate the residual surfactants from the ionomer suspension and dispersive media.

For all electrochemical measurements, both ECR performance in the MEAs and Tafel slopes, the GDEs used had a loading of 1 mg cm^{-2} of the catalyst material.

For the MEA anode, a Bekaert Ti fiber mesh was used as the porous transport layer (PTL). The original Ti-PTL was etched in concentrated boiling HCl of 1 M to break down the initial passivating TiO_x layer. The etched PTL was sprayed with IrO_x nanoparticles provided from Alfa-Aesar, to form the anode catalyst layer. The ink composition used for the anode was: 160 mg of IrO_x and 800 mg of Nafion ionomer, in ethanolic 5% w/w solution, dispersed in 60 ml of methanol. The ink was placed under Ultra-Turex at 33,000 rpm for 10 min and then placed in a sonication ice bath for 60 min. The loading of pure IrO_x was at 1 mg cm^{-2}.

For the Flow-Cell experiments, the counter electrode used, anode, was Ni-foam. The original Ni-foam was sequentially treated and cleaned in the following solutions: 10% HCl, Milli-Q water, and acetone anhydrous. The treated Ni-foam was dried at ambient temperature and placed in the flow-cell, during assembly.

3.5 Electrolyzers Set-Up

The CO_2 electrolyzer, operated through electrical energy, serves as a device for executing the electrochemical CO_2 reduction reaction, ECR. This reaction aims to convert incoming CO_2 into valuable chemicals. Despite notable progress witnessed in recent years concerning the evolution of advanced cell designs, the fundamental functions of the electrolyzer remain largely consistent. Structurally, the CO_2 electrolyzer comprises two distinct compartments: **1.** the cathode and **2.** the anode. These components are electrically interconnected to enable the flow of electrons, while an electrolyte layer is interposed between the electrodes to facilitate the movement of ions. To focus on the tedious ECR, we employ the well-studied and established oxygen evolution reaction, OER, as the anodic reaction of the electrolyzer.

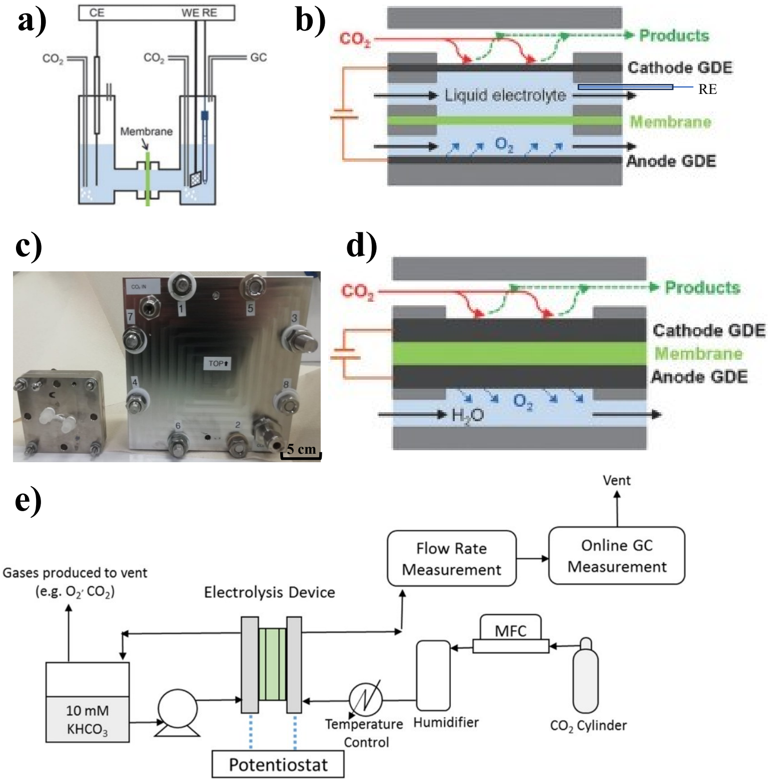

Figure 3.1 The different electrolyzer setups used for the investigation of the ECR. a) H-cell configuration, adopted from[183], b) flow-cell configuration, adopted from[183], c) photo of MEA cells used for this thesis, with active areas of 2 cm^2 and 100 cm^2 respectively, d) MEA cell configuration, adopted from[183], (e) experimental set-up used for evaluating the ECR performance of catalyst's using ECR electrolyzers, adopted from[184].

3.5.1 H-Cell

The electrolyzer set-up of Figure 3.1a, is widely used in the study of ECR, due to its simplicity. The working electrode (WE) consists of the cathode GDE. The reference electrode (RE) used is Ag/AgCl, providing direct measurements of the cathode overpotential η. This electrolyzer is considered a half-cell since the potential is moderated by the RE. The counter electrode (CE) used is a Pt wire, where the anodic OER takes place. In this thesis, this electrolyzer is only used for certain electrochemical characterization methods, like impedance spectroscopy and ECSA measurement. This cell can provide more steady conditions, meaning no bubble interference, during these measurements. The ECR is not studied in this cell because of the great mass-transfer limitations of this system. Additionally, the exposure of the backside of the working electrode to the electrolyte can induce voltage variations across the electrode's surface due to differing distances to the counter electrode at various points.[185]

3.5.2 Flow-Cell

The setup presented in Figure 3.1b, has the advantage of meandering the mass-transport limitations of CO_2 to the catalyst layer. The continuous circulation of electrolytes within the cell contributes further to providing CO_2 in the form of HCO_3^-. Employing a flow cell configuration offers the benefit of effective mass transport, yet the incessant flow induces considerable dilution of any liquid phase products generated, rendering their detection challenging unless they are present in substantial quantities. The cathodic working electrode (WE) consists of a catalyst-coated carbon paper gas-diffusion electrode (GDE). The reference electrode (RE) used is Ag/AgCl, providing direct measurements of the cathode overpotential η. The reference electrode was Ag/AgCl and the applied potentials were related with an RHE using the equation: $E_{RHE} = E_{Ag/AgCl} + 0.059PH + 0.1976$. The electrolyte used was 1 M KOH. This electrolyzer is still considered a half-cell since the potential is moderated concerning the RE. The counter electrode (CE) used is a Ni-foam piece, where the anodic OER in 1 M KOH takes place. An anion exchange membrane (AEM) is used to separate the anodic and cathodic compartments of the cell. The AEM ensures minimum product cross-over and re-oxidation, towards CO_2 in the anode compartment.[186] We used a commercially available flow-cell, purchased from Electro-Cell. The CO_2 was fluxed at a rate of 30 sccm and the electrolyte was circulated at a rate of 5 ml min^{-1}. The current collectors of the cell were made of Ti, owing to its stability at high redox potentials.

3.5.3 Membrane Electrode Assembly (MEA) Electrolyzer

The architecture of the MEA, zero-gap electrolyzers, seen in Figure 3.1c&d, is a direct translation of the fuel cell or the classic acidic or alkaline water electrolyzers. The direct contact of the cathode with the membrane and the anode reduces the ohmic drop, ensuring high CO_2 mass-transport rates at the cathode GDE. The cathodic working electrode (WE) consists of a catalyst-coated carbon paper gas-diffusion electrode (GDE). The cathode is fed with a gas stream of humidified CO_2 at room temperature. The anode consists of a Ti-substrate coated with IrO_x, catalyzing the OER in 0.1 M $KHCO_3$. The anode and cathode compartments are separated again by an AEM Sustainion X37-50 RT, to avoid product crossover. The end-plates and current collectors of the MEA are made of Ti, owning to its redox stability at higher cell potentials. The potential is directly measured between the cathode and anode plate, operating the ECR at single-cell conditions.[187] The CO_2 was humidified at room temperature before entering the cell. The PTFE gasket used had 400 μm thickness and the cell was assembled by applying three Nm torque to each of the electrolyzer's screws. The small MEA was bounded by four screws and the large one by eight. For the large MEA, a customized cell with an active area of 100 cm^2, 10x10 cm^2, was used. The assembly process was kept the same and the cathode, anode, anolyte, and membrane were the same as those used for the 2 cm^2 MEA. The PTFE gasket used had a thickness of 400 μm, maintaining same compression percentage for both cells, and the cell was assembled by applying 5 Nm of torque. The CO_2, fluxed at 1500 sccm, was humidified at room temperature before entering the cell. The large cell was heated to 40 ºC and 60 ºC, successively by inserting heating rods into its housing. The cathode materials were, in each case, the catalyst-loaded GDE that we sought to investigate. The catalyst layer of the anode and cathode faced the AEM membrane during the assembly of the cell.

3.5.4 Mechanical Pressure Distribution in the MEA

For a single MEA cell, the distribution of the mechanical pressure was determined by pressure-sensitive films that were obtained from Fujifilm Europa GmbH. The cells were assembled using PTFE foils of the same thickness as those used during the electrochemical experiments. The cells contained the electrode substrates of the anode and cathode, without any catalyst layer. The Fujifilm was placed in between the anode and cathode electrode substrates without adding any AEM. The original data were deconvoluted using the 'FPD-8010E' software.

3.6 Determination of GDE's Reaction Performance

The performance of an electrocatalytic process is commonly characterized by four main figures of merit including current density, Faradaic efficiency, energy efficiency, and stability. The determination of the above requires the precise quantification of the different products of the ECR.

3.6.1 Gas Chromatography (GC)

In both the flow-cell and MEA reactors, the analysis of CO_2 reduction products to determine the ECR efficiency of the catalyst materials.[188,189] The process involved inline gas chromatography PerkinElmer equipped with a thermal conductivity detector (TCD). The carrier gas, argon, grade 99.999%, propelled the gas mixture from the electrolyzer outlet through the GC capillary column. Packed with molecular sieves, the column effectively separated the gas mixture based on the varying interactions of gas molecules with the column filler. The distinct thermal conductivity of each gas molecule compared to the carrier gases generated an electrical signal, detected by the TCD. After calibration, this signal was translated into the concentration of the component in the gas mixture. The flow rate for each point on the polarization curve was measured at the gas outlet of the cell.

3.6.2 High-Performance Liquid Chromatography (HPLC)

Sample aliquot was collected in the cathode compartment of the flow cell following 30 minutes of stable ECR at selected current density and/or potential. The sample was injected into the chromatograph HPLC-LC-20AD, Shimadzu with an Aminex HPX-87H column, with dimensions 300 × 7.8 mm, capable of analyzing carboxylic acids and alcohols. A diluted solution of H_2SO_4 of 3.3 mmol L^{-1} was used as the mobile phase with a flow rate of 0.6 mL min−1. A sample volume of 20 μL was injected into the column loop. The column and detectors were kept at 40 °C. The HPLC separates the mixture's components, based on the same principles as discussed for the GC in 3.6.1. The chromatograph was equipped with a differential refractive index detector RID-10A that is suitable for the detection of alcohols, and a UV–Vis detector SPD-20A, deuterium lamp, $\lambda = 210$ nm, which is suitable for the analysis of carboxylic acids.

3.6.3 Faradaic Efficiency (FE) & Energy Efficiency (EE)

The Faradaic efficiency for gas products was calculated using the following formula:

$$\text{FE (\%)} = \frac{z \cdot c \cdot v \cdot F \cdot P}{I \cdot R \cdot T}$$

z = number of e^- needed for the product formation, 2 e^- for CO formation.

c= concentration of the product in the gas-outlet stream, determined by GC.

v= flow rate of the gas-outlet stream, measured in sccm.

F= 96485 C mol^{-1}, P=101325 Pa, R=8.314 J mol^{-1} K^{-1}, T= 298 K

I = total current passed through the cathode

The FE was calculated based on the gas flow rate measured at the outlet of the flow cell for the selected points of the polarization curve.

The Energy Efficiency (EE) for CO of the MEA set-up was calculated according to the following formula:

$$EE_{CO} = \frac{1.3}{Ecell} FE_{CO}$$

Where 1.3 V is the thermodynamically required potential for the electrolysis of CO_2 to CO, cathode, and the OER, anode.

E_{cell} = the full cell potential in the MEA set-up.

FE_{CO} = The Faradaic Efficiency towards CO for each point of operation.

The Faradaic efficiency for liquid products was calculated using the following formula:

$$\text{FE (\%)} = \frac{z \cdot c \cdot V \cdot F}{Q}$$

z = number of e^- needed for the product formation, 2 e^- for $HCOO^-$ formation.

c= concentration of the product in catholyte, determined by HPLC.

V= Volume of the catholyte & Q = total charge passed through the cathode

The FE was calculated based on the gas flow rate measured at the outlet of the flow cell for the selected points of the polarization curve.

3.6.4 Polarization Curve

In the flow-cell and MEA electrolyzer, the performance of the cathode GDE was recorded through a polarization curve. Before any polarization curve, in both cell setups, the GDE was activated by performing a cyclic voltammetry (CV). The CV window was: [-0.2 V, -2.2 V] vs Ag/AgCl for the flow cell & [0.5 V, 2.5 V] for the MEA. The polarization curve represents the current/voltage response of the GDE. For the flow cell, a different overpotential was applied to the GDE for 40 minutes. The average current density was recorded during this time. In the thesis, all values of the cathode overpotential are pristine, without iR correction. The product analysis, from both the gas sample and electrolyte aliquot, was performed after 35 minutes of ECR. In the MEA different current densities were applied to the GDE for 40 minutes. The average cell voltage was recorded during this time. In the thesis, all values of the MEA cell voltage are pristine, without iR correction. The product analysis of a gas sample was performed after 35 minutes of ECR. All electrochemical experiments were controlled through a Metrohm AUTOLAB potentiostat PGSTAT302N coupled with Nova software. The measurements for the 100 cm^2 MEA were controlled through a Metrohm AUTOLAB potentiostat PGSTAT302N coupled with a 20 A booster.

3.6.5 Stability Determination

The development of efficient ECR materials requires the determination of their performance under stable ECR conditions. The stability of the catalyst is associated with its ability to maintain a stable and high value of Faradaic efficiency (FE) during electrolysis time. The stability of each catalyst-coated GDE was assessed galvanostatically. A fixed current density value was applied to the cell and the voltage response was recorded. The products were collected and characterized in 1 h intervals. Metrohm AUTOLAB potentiostat PGSTAT302N that utilized Nova software.

3.7 Electrochemical Characterization of the Catalyst-Coated GDE

The electrochemical characteristics of the different catalyst-coated GDEs are strongly associated with their ECR performance. Namely, the characteristics analyzed were: the Electrochemically Active Surface Area (ECSA), Electrochemical Impedance Spectroscopy (EIS), and Tafel-Slopes. For the correct evaluation of the different properties, different electrolyzer setups were used. All electrochemical experiments were controlled through a Metrohm AUTOLAB potentiostat PGSTAT302N coupled with Nova software. For all electrochemical measurements for determining the ECR performance in the MEAs and Tafel slopes, the GDEs used had a loading of 1 mg cm^{-2} of the catalyst material.

3.7.1 Electrochemically Active Surface Area (ECSA)

The ECSA is strongly related to the intrinsic electrocatalytic activity of a catalyst. The measurement of the ECSA was performed in the H-cell, to avoid interference from electrolyte flux and/or bubble formation on the catalyst layer.[190,191] The cell compartments were filled with 0.1 M $NaClO_4$ being Ar saturated, as an electrolyte. This electrolyte was used to minimize any ion-characteristic adsorption and be able to eliminate the effect of the carbon paper, substrate.[192] The ECSA was measured after the catalyst-layer activation, with scan rates among 7.5-100 mV sec^{-1}. the measure of the ECSA was estimated through the double-layer capacitance C_{dl}. The survey CVs were obtained from -0.2 to 0.2 V vs Ag/AgCl, while the potential window selected for the Cdl calculation was –0.1 to 0.1 V vs Ag/AgCl. In that way, we ensured that the current recorded was only due to diffusion and not from any Faradaic process.

3.7.2 Electrochemical Impedance Spectroscopy (EIS)

In the flow cell, the EIS was performed on the GDEs' on-set potential (PEIS), to evaluate the catalyst's charge transfer resistance R_{ct}. In the cell, CO_2 was fluxed at 15 sccm and 1 M KOH circulated at 2 ml min^{-1}. The Nyquist plot was interpreted according to the fitting equivalent circuit of the process. The PEIS was measured in the frequency range of 10^5- $4 \cdot 10^{-2}$ Hz. In the MEA the EIS was measured at fixed current (GEIS), to assess the high-frequency resistance, HFR, introduced by the set-up. In the cell at humidified at RT CO_2 was fluxed at 15 sccm and 0.1 M $KHCO_3$ circulated in the anode at 3 ml min^{-}1. The GEIS was measured in a frequency range of 10 kHz-10 mHz.

3.7.3 Tafel-Slopes

The Tafel slope of a GDE can provide valuable information regarding the ECR conversion path toward a specific product.[193] In this thesis the target product was CO. The Tafel analysis for the different catalyst-coated GDEs was performed in the flow, to have more controlled ECR conditions and avoid the interference of the membrane and anode parts. [194] In the cell, CO_2 was fluxed at 15 sccm and 1 M KOH circulated at 2 ml min^{-1}. The Tafel slopes were evaluated around the kinetic region of the catalysts from -5 to -15 mA cm^{-2}. For each point, represented by a selected current density, of the Tafel analysis, the cell was left running for 40 minutes, and the product characterization, performed by GC sampling of the gas stream, was performed after 35 minutes of ECR. The partial current densities for CO j_{CO} were associated with the GDE's overpotential η to obtain the Tafel-Slopes.

Chapter 4:

ZnO Allotropes for the efficient CO_2-to-CO conversion

Disclaimer:

The content of this chapter is a product of an already published scientific work. The content of which is reproduced for the purposes of this Thesis and under permission of the corresponding Journal.

Ilias Stamatelos, Cao-Thang Dinh, Werner Lehnert, and Meital Shviro
ACS Applied Energy Materials 2022 *5* (11), 13928-13938

DOI: 10.1021/acsaem.2c02557

4.1 Abstract

The practical advancement of electrochemical CO_2 reduction, ECR, requires the creation of stable and selective catalysts, based on cost-effective and abundant materials is indispensable. In the course of this study, we have focused on the formulation of ECR catalysts specifically, based on ZnO, of diverse morphologies such as nanoparticles, nanorods, nanosheets, and irregular structures. Our findings indicate that ZnO nanorods distinctly exhibit the highest efficiency in transforming CO_2 into CO, displaying a substantial CO Faradaic efficiency, FE_{CO}, surpassing 80% across a current density span of 50-160 mA cm^{-2}, both in flow-cell and membrane electrode assembly (MEA) setups. However, the CO selectivity of ZnO-based catalysts gradually degrades over time, particularly under high current densities, exceeding 100 mA cm^{-2}, due to the gradual depletion of the ZnO phase. Addressing this, we devised an *in-situ* regeneration technique for the ZnO-catalyst, involving cyclic oxidations of the cathode during ECR. Employing this strategy, we have successfully demonstrated the conversion of CO_2 into CO, attaining a stable FE_{CO} exceeding 80% for a continuous period of 100 hours, at an elevated current density of 160 mA cm^{-2}.

4.2 Introduction

Zinc oxide, ZnO, is a versatile and cost-effective material renowned for its various applications, owing to its isotropic nature found in diverse allotropic structures.[73,74] These structures exhibit modified morphological and structural properties, such as shape, lattice defects, and oxygen vacancies.[75–77] As demonstrated by Yashimitsu et al.[195] The morphology of ZnO significantly influences its hydrophobicity, a critical attribute for Gas Diffusion Electrodes (GDEs) employed in the Electrochemical CO_2 Reduction, ECR.[90–95] Despite the ECR's high reduction overpotential causing partial reduction of ZnO to Zn metallic[83,96,97], as a non-Faradaic process[98], numerous studies emphasize the potential of ZnO as an ECR catalyst.[82] As exhibited in the work of Nguyen et al.[87] modulating and stabilizing the Zn^{+2} state is vital for the CO_2-to-CO conversion.[86]

While much research has been devoted to improving the performance of such Zn-based catalysts, most of these studies performed ECR in aqueous H-cell systems where the current densities are limited to below 50 mA cm^{-2}.[100] Recently, ZnO has also been employed as an electrocatalyst for the CO_2-to-CO conversion [86] exhibiting promising ECR performance, owing to its crystalline structure and active sites.[30] Further information on the ZnO activity was provided by the work of Zong et al.[75], identifying the oxygen vacancies, in the ZnO structure, to be responsible for enhancing the ECR activity of the material. Nonetheless, only a handful of works demonstrated the performance of ZnO catalysts at industrial-relevant current densities of more than 150 mA cm^{-2} [88,75,81], while omitting any reference to catalyst stability at high current densities. The current research on Zn-based catalysts indicates that these materials exhibit limited stability for current density above 80 mA cm^{-2}.[81]

This study concentrates on crafting ZnO-based catalysts of various morphologies, for the CO_2-to-CO conversion. By evaluating the materials' performance in flow-cell and membrane electrode assembly (MEA) electrolyzers, we recorded impressive CO selectivity exceeding 80%, at a current density of 200 mA cm^{-2}. Our material maintained high CO selectivity for around 10 hours before the ZnO phase was depleted. To extend lifespan, an innovative *in-situ* catalyst regeneration method was devised, ensuring consistent high CO Faradaic Efficiency of over 80% for more than 100 hours at 160 mA cm^{-2}.

4.3 Catalysts Characterization

Scanning electron microscopy (SEM) was used to investigate the morphologies of the prepared catalysts and confirm the successful synthesis of ZnO allotropes with different morphologies. The wet-chemical synthetic approach leads to the formation of ZnO with morphologies of nanoparticles NP, random-shape RS, nanosheets NS, and nanorods NR, as exhibited in Figure 4.1 A-D respectively. The NR exhibits a small diameter of 80 nm and a large aspect ratio of 20:1, length: diameter, and the NS exhibits an average thickness of 20 nm. The NP exhibits a small diameter of 20 nm, while the RS is formed in larger agglomerates, seen in Figure A1 of App. A. The X-ray diffraction results (XRD) in Figure 4.1E, reveal a well-defined crystallographic pattern that can be indexed to ZnO hexagonal wurtzite structure, according to JCPDS #75-576, without impurities, for all samples. As observed in Figure 4.1E, the XRD pattern of NS exhibits broader peaks compared to those of other allotropes. This characteristic is attributed to the 2D morphology of the NSs, as explained also by Scherer's equation and observed in other studies.[73]

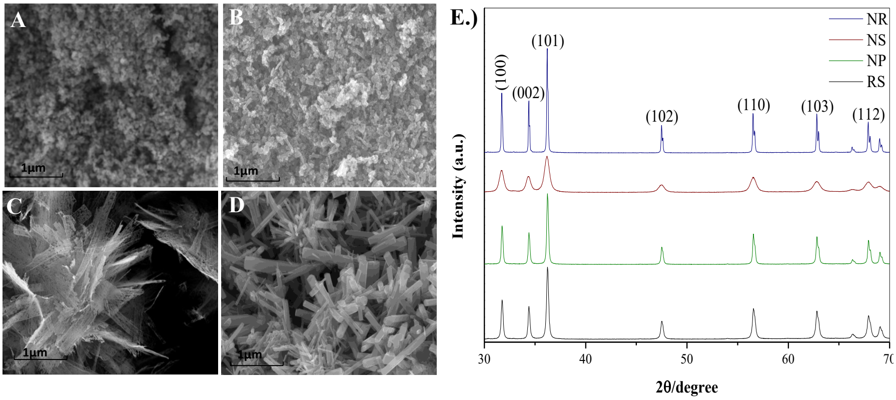

Figure 4.1. SEM and XRD characterization of the synthesized ZnO-based catalyst materials. A.) SEM image of ZnO-NP, B.) SEM image of ZnO-RS, C.) SEM image of ZnO-NS, D.) SEM image of ZnO-NR, E.) XRD diffractogram of all the ZnO powders with different morphology.

X-ray photoelectron spectroscopy (XPS) was used to study the chemical state of the ZnO catalysts at the surface, presented in Figure 4.2. All survey XPS spectra, found in Figure 4.2A, show characteristic peaks in the binding energy range of 1200-100 eV, confirming the presence of Zn and O and the absence of impurities. Additional peaks KLMM, K2s, K2p observed in the spectrum of ZnO NP, are due to the presence of potassium left over from the synthesis. As seen in Figure 4.2A, quantification of the elemental composition reveals differences in the amount of Zn and O atoms on the surface of each allotrope. The ZnO NR presents the highest ratio of Zn:O of 1.24:1, while the Zn:O ratio in the NS is calculated at 1.2:1. These two allotropes exhibit the highest percentage of Zn-atoms on their surface in comparison with the rest of the materials. The difference in the surface ratio of Zn:O can be attributed to the lattice vacancies, O-defects, and O-vacancies, different for each allotrope material.[76,77] Therefore, it can be concluded that the ZnO-NR presents more O-vacancies than the other ZnO-based catalysts.[75] The high-resolution Zn2p3 XPS in Figure 4.2B, also show differences in the binding energies of the characteristic Zn peaks. A difference of 0.7 eV in the position of the Zn-peaks can be observed among our materials. This can be attributed to the distinct difference in morphology, crystallinity, and oxygen vacancies in the materials' lattice, as observed in previous studies.[75,79,197–199] The high-resolution O1s XPS spectra of all allotropes show two deconvoluted peaks at 530 eV and 531.6 eV, which are attributed to the lattice oxygen and oxygen in the form of surface hydroxyl -OH, respectively. The deconvolution of the O-1s peaks, reveals a different ratio between lattice oxygen and surface –OH. From the high-resolution spectra, found in Figure A2 of App. A, the ZnO NR presents the highest amount of lattice-oxygen, revealing a clear crystalline structure on the surface.

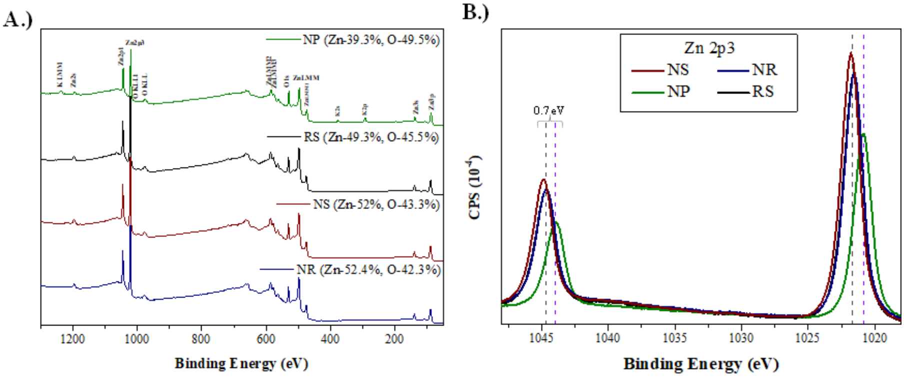

Figure 4.2. XPS characterization of the catalyst powders' surface A.) Survey spectra of all the ZnO-based materials, B.) High-resolution spectra for Zn2p3 of all the ZnO-based materials.

4.4 Performance in the Flow-Cell & Electrochemical Characterization

To evaluate the catalytic performance of ZnO with different morphologies, we first used a flow cell reactor and an alkaline catholyte and anolyte. Carbon monoxide, CO, Faradaic efficiency, FE_{CO}, and partial current density j_{CO} were measured in the potential range of –0.4 to –1.2 V_{RHE}. For comparison, the performance of commercial silver nanoparticles, Ag NP, which have been demonstrated as excellent catalysts for CO_2 reduction to CO, was also evaluated in the same testing conditions.

All ZnO samples show good CO selectivity at applied potential more positive than -0.8V_{RHE}, exhibiting FE_{CO} of around 80%, as summarized in Figure 4.3A. At more negative applied potentials of -1 and -1.2 V_{RHE}, the Zn NR and NS show the highest FE_{CO} of 90 %, which is comparable to the performance of Ag NPs. As observed in Figure 4.3B, ZnO NR shows the highest j_{CO} among all allotropes and at all tested applied potentials. At an applied potential of -1.2 V, ZnO NR exhibits a j_{CO} of -150mA cm^{-2}, while maintaining a good FE_{CO} of 83%. To further compare the intrinsic activity of ZnO allotropes, we measured the Tafel-Slopes for the three best ZnO morphologies NR, NP, and NS. For these measurements, the dependence of j_{CO} on the potentials was studied at a very low applied potential range of –0.4 to -0.6 V_{RHE} to avoid the effect of mass transport. As seen in Figure 4.3C, we observed similar Tafel-Slope values for the three allotropes, indicating similar reaction kinetics. However, ZnO NR shows the highest current exchange density of 8 mA cm^{-2}, implying its highest intrinsic activity and lower onset potential among the allotropes for the ECR.[194]

To understand the effect of the morphologies on ECR performance of ZnO allotropes, we measured the electrochemical surface area (ECSA) of the samples, after GDE activation. Among the allotropes, the NR exhibits the highest value of C_{dl} and hence ECSA, as indicated in Figure 4.3D. The ECSA characterization for other allotropes follows the performance trend observed in the polarization curves, previously encountered in Figure 4.3B, samples with the higher ECSA exhibit higher $j_{CO.}$

We performed Potentiostatic Impedance Spectroscopy (PEIS) measurement to study the charge transfer resistance, R_{ct}, induced by different ZnO allotropes, exhibited in App. A Figure A3. The ZnO-nanorod presents the lowest R_{ct} and overall resistivity towards the ECR, indicating a more favorable mass-transfer kinetics over the GDE, and a higher ECR activity of this allotrope. This result can be associated with the more active sites available on the nanorods, in agreement with the tendency exhibited by the rest of the electrochemical characterizations.

For ECR in the gas phase, GDE hydrophobicity can affect CO_2 and water transport and thus catalytic performance. The hydrophobicity of GDE from different ZnO allotropes was characterized by measuring the contact angles, seen in App. A Figure A4. The nanorod GDE exhibits a sharp increase in its inherent hydrophobicity and shows the most significant contact angles compared to the other ZnO GDEs. This property can be attributed to the different ionomer distributions in the allotropes due to the different ECSA of each GDE. Furthermore, this behavior can also be related to the different morphology itself, as this is a feature that alone can affect the wettability under static conditions.[91,195] Increased hydrophobicity in the catalyst layer has been shown to increase the ECR in flow cell systems by balancing the gas/liquid microenvironment above the catalyst layer.[90]

The physical and chemical changes of the ZnO catalyst during ECR were characterized after the ECR reaction at -160 mA cm^{-2}, for 10 hours. The post-mortem XRD spectra of ZnO NR after continuous operation showed a much lower intensity of ZnO peaks compared to pristine ZnO, found in App. A Figure A5. Additional peaks attributed to metallic Zn and $Zn(OH)_2$ were observed indicating the reduction of ZnO to metallic Zn during ECR. The presence of $Zn(OH)_2$ could be attributed to the oxidation of metallic Zn to the electrolyte, $KOH_{(aq.)}$, after the reaction. As illustrated in Figure A6 of the App. A, the morphology of the ZnO allotropes changed significantly after the ECR reaction. This is attributed to the simultaneous reduction of ZnO to Zn during the ECR reaction, resulting in this difference in morphology.[83] The conversion of the oxide phase into metallic, is a non-faradaic process proven to be responsible for alteration on the surface catalyst.[82,98]

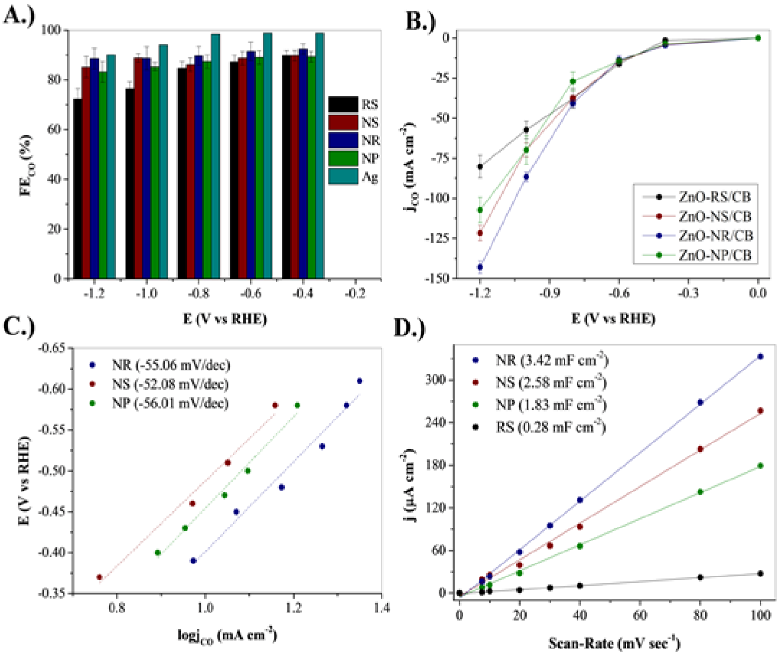

Figure 4.3. ECR performance of the different ZnO-based GDEs in flow-cell and electrochemical characterization. A.) Selectivity of the GDEs towards CO FE_{CO} in the potential window operated in the flow cell, B.) Partial current density j_{CO} of the catalyst-loaded GDEs in the flow cell, C.) Tafel-Slopes of the catalyst loaded GDEs, measured in the flow-cell set-up, D.) The C_{dl} of the different catalyst-loaded GDEs, measured in H-cell using 0.1 M $NaClO_4$, Ar saturated.

4.5 Performance & Stability in the MEA Cell

MEA electrolyzers have proven to be a promising platform for ECR technology because they reduce ohmic losses and provide high-energy efficiency. The cell architecture enables realistic operating conditions that are closer to a commercial application. To evaluate the performance of ZnO allotropes in the MEA cell configuration, as described in 3.5.3. The FE_{CO} was measured in a wide current density range of 30-200 mA cm^{-2} of the three allotropes that exhibited the best performance being the nanoparticles, nanosheets, nanorods in the flow cell configuration. As shown in Figure 4.4A-C, all three allotropes exhibited FE_{CO} above 80% in the current density range of 30-150 mA cm^{-2}. At higher current densities, an increase in FE for hydrogen was observed at NS and NP, while NR exhibits FEs for H_2 below 20%. As a result, ZnO NR maintains FE_{CO} above 80% at all tested current densities. Compared to NS and NP, ZnO NR also exhibits the lowest cell voltages at all current densities, further confirming its highest catalytic activity among the allotropes, displayed in Figure 4.4D. Due to its higher FE_{CO} and lower cell voltage, ZnO NR shows the highest CO energy conversion. It should be noted that as exhibited in Figures A7 & A8 of the App. A, ZnO NR also outperforms Ag NPs in terms of j_{CO} and CO energy efficiency EE_{CO}, in MEA cell configuration. Zn-based catalysts have not yet been used in an MEA system.

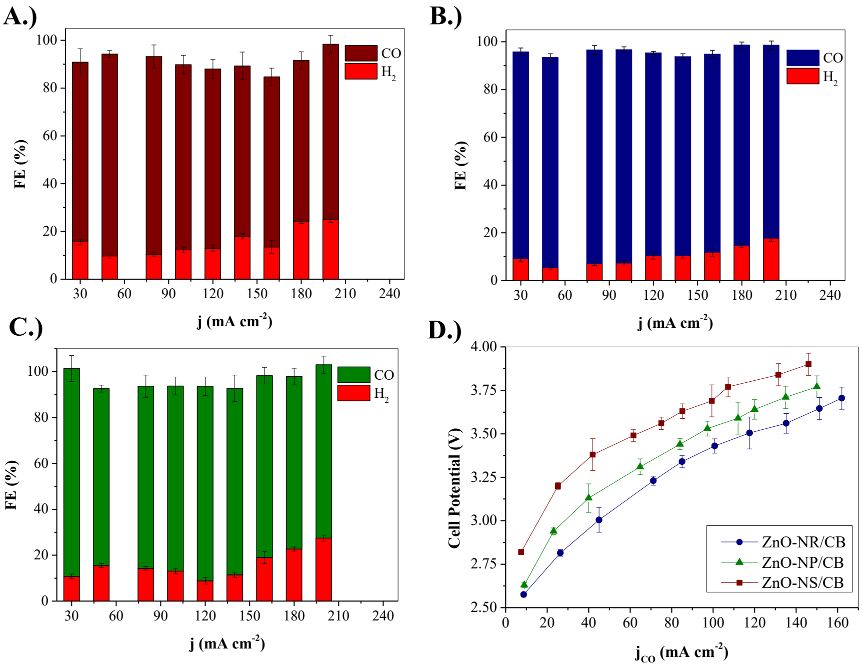

Figure 4.4. Evaluation of the ECR performance for the ZnO-based GDEs in the MEA system. A.) Selectivity FE_{CO} of the ZnO-NS GDE, B.) Selectivity FE_{CO} of the ZnO-NR GDE, C.) Selectivity FE_{CO} of the ZnO-NP GDE, D.) Polarization curves, in terms of partial current density towards CO j_{CO}, for the different catalyst-loaded GDEs.

To investigate the stability of the catalysts in the MEA cell configuration, we applied a constant current density of 160 mA cm^{-2} and measured the change in FE_{CO} and cell voltage over time, as demonstrated in App. A Figure A8 & A9. From Figure 4.5A, it can be seen that both NS and NP decrease by 50% of their initial FE_{CO} value after 10 hours of continuous reaction. In contrast, ZnO NR maintains its high CO of over 80% for the first 10 hours before dropping to 40% after 20 hours of reaction. We performed stability test at different current densities and found that the catalysts are more stable at lower current densities, summarized in Figure 4.5B. This result suggests that high operating current density, meaning high cell potential, induces physical and chemical changes in ZnO catalysts that lead to a decrease in CO selectivity. High cathodic overpotential is known to cause drastic depletion of ZnO, inducing its conversion into metallic Zn.[92] In addition, the overpotential is also related to the change in the properties of the carbon black NPs in the catalyst layer of the GDE, inducing changes in surface properties[93] and loss of hydrophobicity [157,158]. The degradation could also be associated with these changes occurring to the carbon paper properties. Previous studies have demonstrated that under ECR conditions, the GDE's hydrophobicity is seriously decreased and the electrolyte can penetrate through GDE and decrease the CO_2 diffusion, leading to the reduction in CO selectivity.[94,95]

As discussed in the 4.4 section, the ZnO catalysts undergo significant changes in morphology and oxidation state during ECR, due to the reduction of ZnO to metallic Zn, which induces the change in the morphology, including aggregation as captured in

Figure A6 at App. A. The same phenomenon can also be observed in the MEA system. As seen in Figure 4.5A, ZnO-NR GDE exhibited the longest inherent stability for continuous ECR operation. We performed SEM characterizations, displayed in Figure 4.5C&D, to investigate how the morphology of the ZnO-NR changes under the cathodic overpotential of the ECR. The first morphology alterations can be observed in Figure 4.5C, after 2 h of operation. The catalyst exhibits a structure that resembles the initial one, previously seen in Figure 4.1D. The longest operation time induces further changes in the morphology. In Figure 4.5D the morphology of the catalyst layer is shown after 10 h of ECR, where the threshold of stability deterioration is recorded. The catalyst layer exhibits a drastic change in its morphology, adopting a layered structure with uniform distribution. We reason that the high crystallinity and high ECSA of the ZnO-NR GDE are the main reasons for its high ECR stability because these two factors could help slow down the ZnO reduction and aggregation process. To prove that high ECSA is critical to ECR stability, we increased the catalyst loading of NR to 3 mg cm^{-2} and studied its stability at 160 mA cm^{-2} current density. Indeed, as seen in Figure 4.5E, the GDE maintains FE_{CO} over 80% for 50 h – a five-fold improvement compared to GDE with 1 mg cm^{-2} loading.

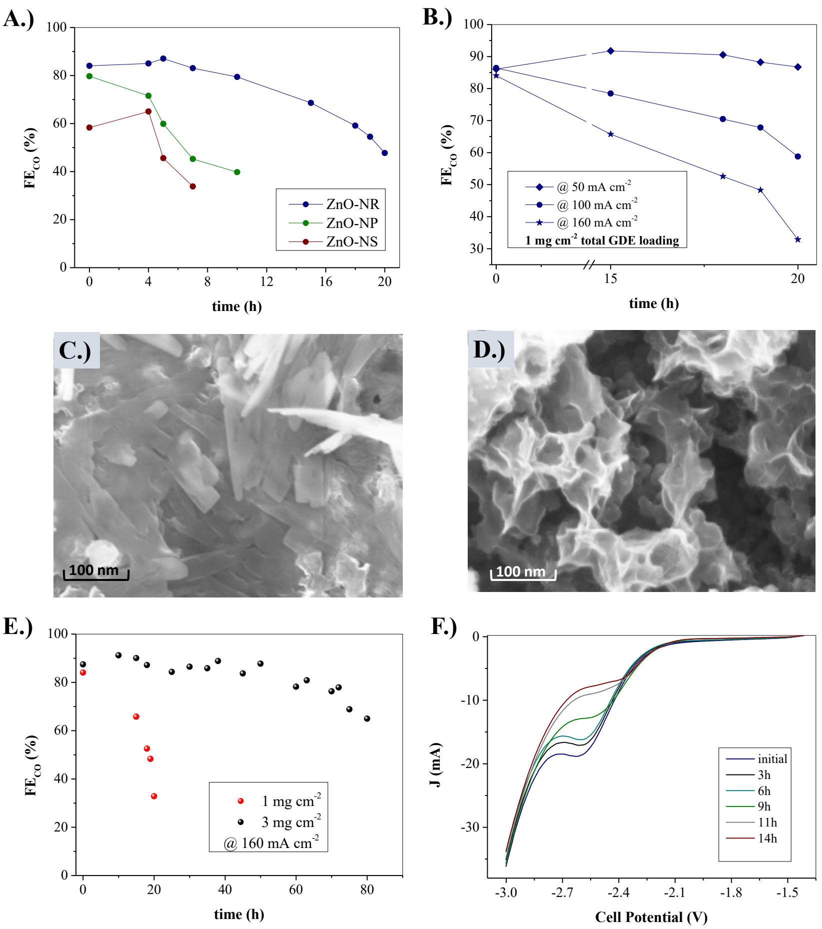

Figure 4.5. Stability and characteristics of the different ZnO-based GDEs in the MEA system. A.) Effect of the different morphology at the GDE stability at 160 mA cm^{-2}, B.) Effect of applying different current densities at the ZnO-NR GDE, C.) & D.) SEM images of the ZnO-NR GDE after 2 h and 10 h of continuous ECR respectively, at 160 mA cm^{-2}, E.) Stability of the ZnO-NR GDE at different catalyst loading, F.) Forward CV scans during continuous operation at 160 mA cm^{-2} of the ZnO-NR GDE, tracking the ZnO shoulder.

4.6 Improvement of Stability Through Novel MEA Operational Strategy

To better understand the changes occurring on the catalyst layer, in the MEA, we acquired the Cyclic-Voltammetries (CVs) of ZnO-NR GDE during the ECR in the MEA cell. The survey CV of the MEA detects the presence of ZnO, locating a shoulder peak at a voltage of 2.5 V, as indicated in Figure 4.5F and Figure A10 of App. A, which corresponds to the reduction of the ZnO.[96,97] The initial CV and the CV after 3 hours of operation, while the catalyst is still selectivity for CO, exhibit this distinct shoulder owing to the presence of ZnO. Throughout continuous operation, the ZnO-reduction shoulder exhibits a constant decrease in its intensity. While this shoulder disappeared after 14 hours of reaction, as observed in Figure 4.5F. This result underlines that the reduction of the ZnO phase does not only co-exist with the ECR[188,189] but also that the ECR activity is closely related to the existence of the ZnO phase.[86,87]

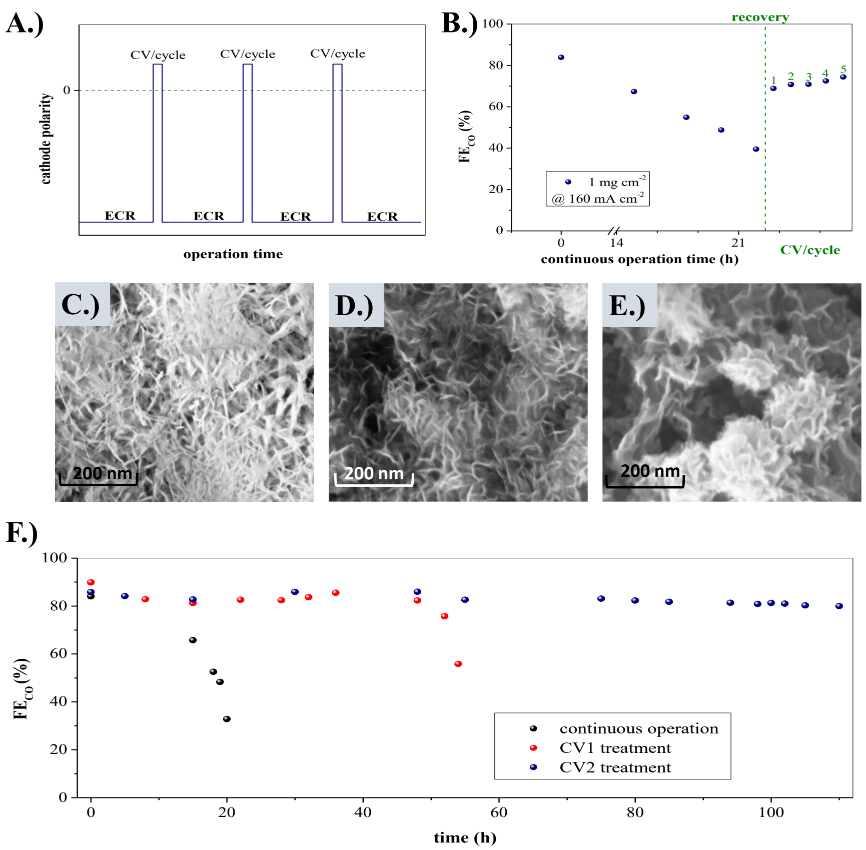

Figure 4.6. Stability and characteristics of the ZnO-NR by applying periodical *in-situ* electro-oxidation, during the ECR at 160 mA cm^{-2}, in the MEA system: A.) Schematic representation of the MEA operation strategy, B.) Recovery of the ZnO-NR GDE performance, by applying oxidation-CV cycles, after FE deterioration caused by continuous ECR operation, C.-E.) SEM images of the ZnO-NR GDE during our operation protocol in the MEA system after 5 h, 40 h, and 100 h respectively, F.) Long-term stability of the ZnO-NR GDE by applying our periodical CV oxidation strategy at different potential windows, CV treatment.

Inspired by the finding of the connection between the ZnO phase and GDE stability for ECR discussed above, and summarized in Figure 4.5B and 4.5F, we hypothesize that the ECR operation time can be extended if the ZnO phase can be maintained in the GDE. While increasing the loading of the catalyst can improve the catalyst stability, the FE for CO would decrease eventually because ZnO is inevitably reduced during the ECR process, as we demonstrated for the 3 mg cm^{-2} loading sample, as seen in Figure 4.5E. We sought to maintain the ZnO phase during ECR by employing an *in-situ* oxidation strategy in which the catalysts are periodically oxidized electrochemically, an operational strategy illustrated in Figure 4.6A. To test this concept, we first run ECR continuously at -160 mA cm^{-2} until the FE decreased from 83% to 40%, as described in

Figure 4.6B. Next, we performed two CVs in the potential range of -2– 0.5 V, illustrated in Figure A10 of App. A, to attempt to reconstruct the ZnO phase and recover the FE_{CO}. The potential window was chosen to ensure the oxidation of the formed metallic Zn into ZnO[97,200], while avoiding negative potentials that would favor the ECR. After the two CVs, we ran the reaction for 20 min at the same current density of 160 mA cm^{-2}, and found that the FE_{CO} was recovered, increasing from 40% to 65%. The FE_{CO} was further improved by repeating the CVs step, reaching 78% after 5 repeating cycles, with each cycle consisting of 2 CVs and 20 min of reaction at 160 mA cm^{-2}. Having discovered that FE_{CO} can be recovered with *in-situ* oxidation CVs, we sought to establish operational protocols that involve one oxidizing CV cycle followed by 1 h of continuous operation at 160 mA cm^{-2}. The CV potential window was adjusted to extend the operational time. When the oxidation window is -2– 0.5, CV1, FE_{CO} can be maintained for over 40 hours. Further increase of the potential window to -2 and 1 V, CV2, to increase oxidation current, the FE_{CO} was stable at over 80% for at least 100 h- an order of magnitude longer than that of continuous operation without *in-situ* oxidation step, as presented in Figure 4.6F. The SEM characterizations of the ZnO-NR GDE, seen in Figure 4.6C-E, reveal more about the structural changes on the catalyst layer, during our operation strategy. The ZnO-NR GDE can withhold for a longer time, of up to 40 h, a structure close to its original nano-rod-like morphology as captured in Figure 4.6C and D, due to our *in-situ* regeneration strategy. For longer reaction time, a uniform nano-layered structure is adopted, seen in Figure 4.6E, at 100 h of operation. Our *in-situ* approach has a direct impact on the catalyst structure, promoting a uniform distribution of the active Zn/ZnO phase and high surface area.

Our strategy enables our system to exhibit stability for more than 100 hours. Our results show that stable ECR can be achieved by balancing the oxidation and reduction conditions. The latest is associated with preserving both the existence and a high surface area, of the ECR-active Zn/ZnO interface. The oxidation step recovers the ZnO phase, which is present for more than 100 hours, as confirmed by the additional data presented in Figure A5 & A11 of App. A, during the long-term ECR reaction, by applying the periodical oxidation strategy.

4.7 Chapter Summary

In this section, we studied the catalytic performance of ZnO catalysts synthesized via facile wet-chemical techniques in ECR using flow cell and MEA reactors. ZnO catalysts with different morphologies achieve a high FE_{CO} of over 80% at current densities below 150 mA cm^{-2}. Among them, ZnO-NR exhibits the highest FE_{CO} of over 80% in both reactor types at 150–200 mA cm^{-2} and maintains stability for 10 hours at 160 mA cm^{-2}. FE_{CO} gradually declines due to ZnO phase depletion, but our in-situ regeneration strategy extends catalyst lifetime. We achieved a stable FE_{CO} over 80% for 100 hours at 160 mA cm^{-2} in MEA, surpassing the durability of alternative materials. This work highlights the potential of inexpensive ZnO-based catalysts for large-scale ECR.

Chapter 5:

Influence of ZnO Heterostructures on Electrochemical CO_2 Reduction

Disclaimer:

The content of this chapter is a product of an already published scientific work. The content of which is reproduced for the purposes of this Thesis and under permission of the corresponding Journal.

Ilias Stamatelos, Gelson T. S. T. da Silva, Caue Ribeiro, and Meital Shviro

ACS Applied Energy Materials 2023 6 (22), 11510-11520

DOI: 10.1021/acsaem.3c01791

.

5.1 Abstract

Feasible electrochemical CO_2 reduction, ECR, requires accessible and efficient catalyst materials. Herein, we prepared ZnO-based catalysts, decorated with various d-block metals like Cu, Ni, Co, Fe. Employing a Flow-Cell configuration, we assessed the ECR performance of these heterostructured catalyst materials. Our findings indicate that ZnO serves as an active catalyst substrate with tunable selectivity and stability, which are dependent on the properties of the formed heterostructures. Notably, the Cu-ZnO catalyst exhibited a 30-hour stability and a 77% CO selectivity at 100 mA cm^{-2}. Recording a three-fold improvement of its ECR stability, compared to pure ZnO. This study seeks to offer a foundational grasp of composite heterostructured materials' properties and electrochemical behavior. We demonstrated that heterostructure engineering presents a promising and cost-effective avenue for bolstering stability in ECR catalyst development.

5.2 Introduction

Despite the promising performance of zinc oxide, ZnO, based materials, for the ECR, stable and direct electrolysis at a current density j above 80 mA cm^{-2} still poses a challenge.[56–58] As demonstrated from our previous work, in Chapter 4, the depletion of the ZnO phase is the main reason for the stability deterioration of the material. As such, stabilizing the ZnO phase could prolong the stability of the material during ECR, without compromising its selectivity towards CO.

A common strategy for either improving the stability or steering the selectivity of the catalyst is the introduction of different phases.[102] Heterostructured catalysts may exhibit altered properties according to their structure and composition, dictated by the different phases.[114–119,201] ZnO is known to show a significant change in its electronic properties and structure when coupled with materials such as Co[121, 120], Ni[122], or Fe[114]. Despite these findings, ZnO-based heterostructures have not been investigated for ECR applications leaving unexplored the ECR-application potential for this class of materials. The latest work of Sikam et al.[108], explored through a first-principal study the electrochemical ECR behavior, of ZnO, coupled with d-block metal. Therefore, we decorated the ZnO surface with different d-block metals: Fe, Co, Ni, and Cu. Thus producing heterostructures of nanometric-scale, with potential application in the ECR. The samples were prepared by the polymeric precursor method and had their catalytic properties evaluated, for the ECR, in a continuous flow-cell electrolyzer. Our studies illustrated that the electrocatalytic activity is modulated and correlated by the structural and physical characteristics of the composite material. The electrochemical performance and characteristics of the composite materials for the ECR were investigated, pointing out that the introduction of copper over the ZnO results in the most ECR-active catalyst.

5.3 Catalysts Characterization

The X-ray diffractograms (XRD) of all synthesized materials are summarized in Figure 5.1A. The pure ZnO sample exhibits a highly crystalline structure, without any impurities in its crystal planes. The crystallographic pattern suggests that the ZnO phase is coordinated into a hexagonal wurtzite structure, according to JCPDS #75-576. The rest of the ZnO-based samples were synthesized by introducing small amounts of the selected transition metal ions. Thus, the samples Zn/Cu, Zn/Ni, Zn/Co, and Zn/Fe show diffraction peaks that can be indexed to the structure monoclinic, tenorite phase as in JCPDS #41-254, cubic-bunsenite phase like JCPDS #47-1049, cubic relevant to JCPDS #65-3103, and cubic-magnetite phase correlated with JCPDS #79-419, respectively.

These results indicate that the addition, constant 20%, of the d-block metals, to the zinc precursor strains the ZnO crystalline lattice over the doping limit. It leads, after calcination, to the formation of a secondary phase, thus suggesting the heterojunction formation.

The segregation of the secondary phase and the impact of the introduced phases on the vibrational properties of the ZnO were investigated by Raman scattering spectroscopy, ass seen in Figure 5.1B. Pristine ZnO has narrow and well-defined peaks, with symmetry described by the point group C_{6v}. The strongest peaks at 99 cm^{-1} and 437 cm^{-1} are associated with the E_2 vibration mode, $E_{2\ low}$ due to Zn sub-lattice vibration and $E_{2\ high}$ due to oxygen atoms vibration, respectively,[202] and the peak at 330 cm^{-1} are associated with $E_{2\ high} - E_{2\ low}$ vibration mode. These active Raman signals are sensitive to crystal stress and the formation of defects. The Raman scattering for Fe^{2+}, Co^{2+}, Ni^{2+}, and Cu^{2+} containing ZnO shows a suppression of the characteristic active vibrational modes for the hexagonal wurtzite ZnO and the appearance of signals for the vibrational modes of the different oxides based on each transition metal ion. The spectra of the ZnO samples coupled with Fe^{2+} and Co^{2+} ions show a more significant change in the shape and intensity of the peak than with Ni^{2+} and Cu^{2+}. This behavior would also justify the microstrain ε, alterations caused in the ZnO crystal plane, summarized in Table B1 of App. B. Higher ε is observed in the ZnO-plane of the Co- and Fe- composite materials, than the rest of the composite materials. Indicating a higher degree of distortion in the ZnO-plane caused by the Fe^{2+} and Co^{2+} ions. It regards the higher permeability of smaller ions in the structure, replacing more Zn^{2+} sites and inducing disorder in the crystalline lattice, which leads to the disruption of the translational periodicity. Moreover, these deformations can be due to the formation of Fe_2O_3, Co_3O_4, NiO, and CuO nanoparticles over the ZnO surface.[203]

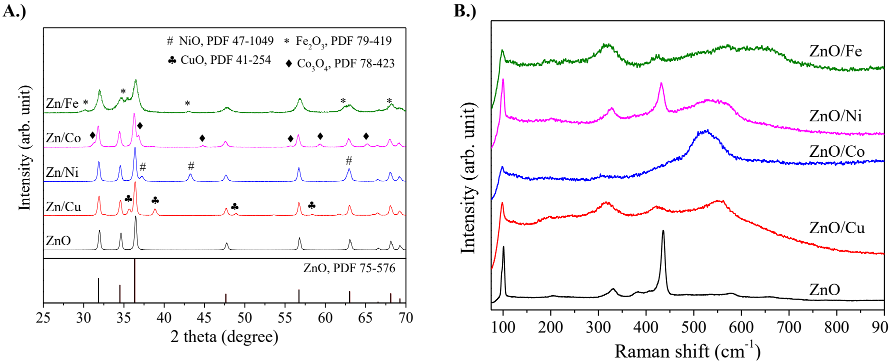

Figure 5.1. Structural characterization of the synthesized composite heterostructured catalyst materials. A.) XRD diffractograms of the catalyst materials, B.) Raman spectra of the of the catalyst materials.

X-ray photoelectron spectroscopy (XPS) was performed to study the oxidation state of the heterostructured ZnO samples, confirming that all the d-block additives are in their oxide form rather than metallic.[116] The high-resolution XPS of the d-block metals indicate their existence in various oxidation-state pointing to heterostructures of distinct phases. The high-resolution Ni spectrum, at Figure 5.2A, shows peaks in two distinct regions. The first and most intense signal was well-fitted and revealed two deconvolutions, a profile characteristic of the Ni=O bond of NiO. Similarly, the intense signal in the second region, attributed to the signal from the metal satellite peak, suggests that the sample is dominated by the Ni^{2+} ions characteristic of the NiO product.[117] The Fe-XPS, Figure 5.2B, points out the presence of Fe mainly in the oxidation state +3.[118] The magnetite Fe_2O_3 phase, mainly constitutes the Fe-based phase of the ZnO/Fe material. The high-resolution Co 2p XPS spectra of Figure 5.2C, display two significant peaks at 779.6 and 789.3 eV, ascribed to the typical Co $2p_{3/2}$ and Co $2p_{1/2}$ orbitals. The signal at 779.6 could be deconvoluted in two different peaks that indicate the presence of Co^{3+} and Co^{2+} cations. The other peak at 789.3 eV was well-fitted and confirmed the satellite signal of the cobalt species. The presence of both Co^{3+} and Co^{2+} ions in cobalt oxide is linked to the presence of the Co_3O_4 crystalline phase considered the most stable phase for cobalt oxide.[201] The Cu XPS of Figure 5.2D, reveals the Cu^{2+} oxidation state.[119, 204], indicating the existence of CuO as the main heterostructured phase of the ZnO/Cu catalyst.[111] The formation of Cu-hydroxide species, as seen from the O-XPS spectra of the App. B Figure B1, partially contributes to the dominance of the Cu^{+2}. The metal-hydroxide species observed in the High-Resolution XPSs of all heterostructured catalysts, summarized in Figure 5.2, are leftover species after calcination. The organic-derived oxygen observed in the O-XPS originates from the metal-acetate precursors used during synthesis. The Zn-XPS, seen in App. B Figure B1C, of the different samples shows no alterations in the electronic state of ZnO. They indicate clear phase separation and no doping interaction between the material's ZnO and the metal-oxide phase.

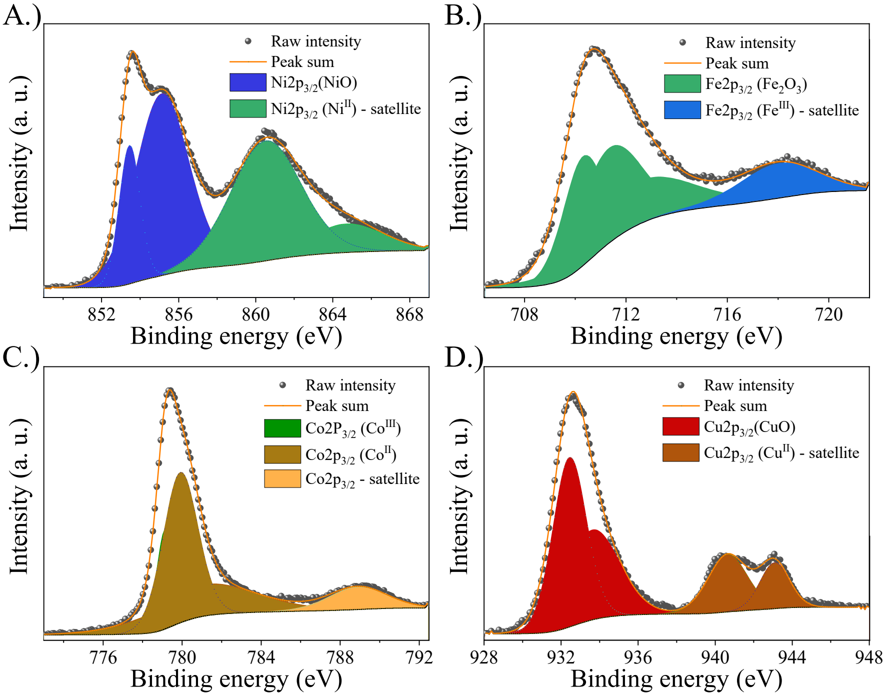

Figure 5.2. XPS spectra of the as-prepared catalyst powders. A.) High-resolution spectra of the Ni-ZnO, B.) High-resolution spectra of the Fe-ZnO, C.) High-resolution spectra of the Co-ZnO, D.) High-resolution spectra of the Cu-ZnO.

The SEM micrographs, found in App. B Figure B1A, display the morphologies of the unmodified ZnO and ZnO-based heterojunctions. There is no significant difference in the morphology of ZnO with and without the d-block metals, indicating that there was possibly the growth of a secondary phase with morphology similar to pure ZnO, an effect promoted by the polymeric precursors' method, which makes its identification by SEM difficult. Using STEM-EDX, seen in Figure 5.3, more details about the structure of each sample could be revealed. It can be seen that the introduction of d-block metals, leads to the formation of metal islands over the main ZnO substrate. The formation of surface islands differs in terms of size and surface distribution, for the different metals examined. The copper and nickel oxides tend to form larger particles, while cobalt and iron oxides are more evenly dispersed over the ZnO surface. The latest may be related to a higher tendency to Co and Fe diffusion in ZnO structure, increasing the surface interaction.[205] Although the previous results confirm that the metals have segregated as heterojunctions, the dispersion of these islands may affect the activity since the catalytic sites are different.

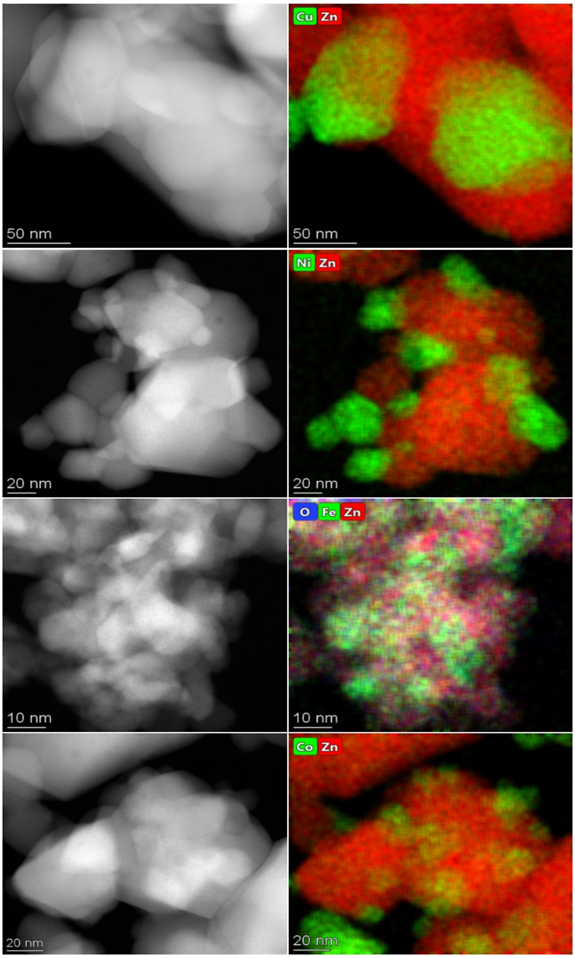

Figure 5.3. STEM elemental mapping analysis of the ZnO-heterostructured catalyst materials. The ZnO coupled with CuxO, NiO, Fe2O3, and Co3O4 phases is presented from top to bottom.

5.4 Performance in the Flow-Cell & Electrochemical Characterization

The detailed selectivity of the ECR of all catalyst materials is summarized in Figure 5.4. The differences observed in the product distribution are attributed to the effect of the electrocatalytic activity, caused by the d-metal islands. As expected, the pure ZnO nanoparticles, as seen in Figure 5.4A, exhibit high selectivity towards CO, FE_{CO}, while their tendency to produce formate, $HCOO^-$, is moderate, owing to the strongly alkaline environment used in the flow cell.[88] The introduction of d-block metals enhances H_2 production or favors the path of formate production, depending on the element. Co-ZnO, illustrated in Figure 5.4B, exhibits decreased H_2 production, indicating stronger activity towards the ECR. The presence of Co-islands enhances the formate production while the CO production exhibits a slight decrease, in comparison with the pure ZnO. On the other hand, Fe-ZnO and Ni-ZnO, depicted in Figure 5.4C and 5.4D respectively, exhibit no selectivity towards $HCOO^-$ formation, indicating that the presence of these d-metals suppresses this catalytic path, at alkaline pH, favoring only CO and H_2 production. Nonetheless, both Fe-ZnO and Ni-ZnO exhibit low selectivity towards CO, recording a higher production rate of H_2. The composite Cu-ZnO catalyst, seen in Figure 5.4E, is identified to primarily form CO with high selectivity, of about ~70%, and secondarily $HCCO^-$. This catalyst exhibits noticeable ECR activity owing to its low tendency of H_2 formation. Copper and Cu-based GDEs are reported to form C_+ products.[206,207] Nonetheless, previous studies have associated the selective formation of CO and $HCOO^-$, with the presence of Cu^{+1} phase over the catalyst surface.[111–113] The latest can be associated with the Cu-surface properties and the low amount of Cu, of 20%, at our Cu-ZnO catalyst. As seen in the XPS study, found in Figure 5.2A, the surface Cu is in majority in the Cu^{+1} state, coexisting with the Cu^{+2} as well. As seen in Figure 5.4F, the pure ZnO presents the highest FE_{CO} while the rest of the heterostructured materials, apart from the Fe-ZnO, present similar FE_{CO}. This can be explained by recognizing ZnO as the main active catalyst phase for CO. ZnO is present in all of the composite materials and dominant while consisting of 80% of their mass. The lower FE_{CO} recorded was for the Fe-ZnO. The latest result is associated with the known high activity of Fe for HER[109,110] and with the diminishment of active ZnO site owing to the uniform distribution of Fe, as seen in Figure 5.3. The ECR performance and selectivity of the catalysts were summarized in Figure 5.4F in terms of partial current density for CO formation since this is the main product of the catalysts. The polarization curves indicate that the Cu-ZnO and ZnO GDEs are the most active for the ECR and especially for CO formation. The Cu-ZnO catalyst records a maximum j_{CO} of -120 mA cm^{-2}, while the least performing catalyst for ECR is the Fe-ZnO with j_{CO} of -60 mA cm^{-2} at the same overpotential of -1.2 V_{RHE}. The improved catalytic performance of the composite materials is affected by factors such as catalyst dimensionality, surface chemistry, electron transport pathway, and morphology.[70]

A similar trend in the electrocatalytic performance of the GDEs, as seen in Figure 5.4F, can be also observed in App. B Figure B2. The polarization curves, under ECR and HER conditions, were measured under the same gas flow rates, to simulate a similar gas-dynamic environment. The ZnO-GDE presents higher current densities for ECR, coming following its greater sensitivity towards ECR, seen in Figure 5.4A. While the Fe- and Co- ZnO GDEs are more active under HER-favoring conditions, owing to the presence of the Fe- and Co- centers. The Ni-ZnO exhibits higher current densities for the ECR than the HER. Despite that the Ni and NiO phases are known electrocatalysts for the HER [208], the low HER activity of this catalyst can be attributed to the formation of the β-$Ni(OH)_2$ phase.[209,210] The XPS spectra for the Ni-ZnO material, shown in Figure 5.2, clearly show the formation of $Ni(OH)_2$, while the XRD peaks, presented in

Figure 5.1, indicate the formation of the β-$Ni(OH)_2$ phase with the characteristic (101) and (111) plane orientations.

The hydrophobicity of the catalyst layer plays a major role in the performance of the GDEs for the ECR.[197,211,212] In our GDEs the measurements of the contact angle, presented in App. B Figure B3, reveal similar hydrophobic environments for all of the electrodes. Hence, the differences in the catalytic performance are to be attributed only to the properties of the catalyst materials and not to any differences in the physical properties of the GDEs.

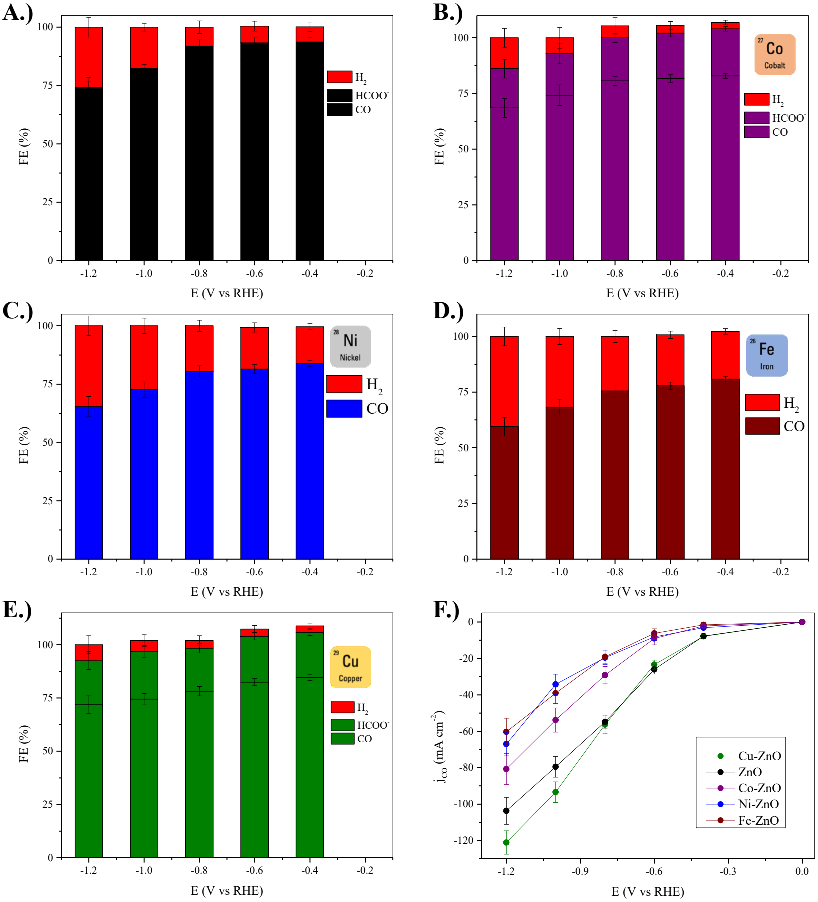

Figure 5.4. Product selectivity and performance of the catalyst-loaded GDEs. The measurements were conducted in the Flow-Cell, in alkaline 1 M KOH. A.) ZnO, B.) Co-ZnO, C.) Ni-ZnO, D.) Fe-ZnO, E.) Cu-ZnO, F.) Polarization curves of the partial current densities j_{CO}, for the catalyst loaded-GDEs.

A common factor for all of our materials is their tendency to form mainly CO, a feature quantified through their selectivity, summarized in Figure 5.5A. We sought to explore more this trend through the electrochemical characterization of the GDEs. The Tafel-Slopes, presented in Figure 5.5B, provide more details about the materials' ECR kinetics towards CO since this is the main product of all prepared materials. The Cu-ZnO GDE exhibits the fastest kinetics for the CO formation, with a slope of -61.76

mV/dec, while the pure ZnO GDE exhibits -82.66 mV/dec. The rest of the d-block metal ZnO GDEs present a higher kinetic barrier for the CO formation, following the performance tendency observed in the polarization curves, shown in Figure 5.4F. The Cu-ZnO presents even faster kinetics for the CO formation even though this catalyst favors also the *OCHO formation path.[28] The Cu-ZnO GDE exhibits the highest internal exchange current density, which is associated with the lowest overpotential that Cu-ZnO structures are reported to induce for the ECR[29,30] and the contribution of Cu in CO formation. For the rest of the heterostructured GDEs, the slower kinetics are attributed to the enhanced HER rate, arising from the exposed d-block metallic centers. For these materials, the lower exchange current density, hence ECR onset potential, seems to be associated with the coverage of the ZnO active sites by the d-block metal islands, as exhibited in Figure 5.3.

The electrochemical surface area (ECSA) shown in Figure 5.5C, of the catalyst-loaded GDEs follows a similar trend to the performance recorded in the polarization curves. Even though most of the catalyst-loaded GDEs showed similar values of double-layer capacitance C_{dl}, the Fe-ZnO GDE recorded the highest value of C_{dl}. The latest can be associated with the structure of the composite Fe-ZnO material, previously shown in Figure 5.3. Indicating a fine and uniform contribution of the Fe-centers over the ZnO core. A similar trend with the ECSA can be also observed in the results of the BET analysis, summarized in App. B Figure B4. The specific surface area of the catalysts, determined by N_2 physisorption, indicates that the structure and the distribution of the d-block metals also affect the physical surface area. The influence of both the type and quantity of exposed d-block phases on the catalyst's Electrocatalytic Reduction, ECR, activity is evident in the active Turnover Frequency for CO, TOF_{CO}. The App. B Table B2 provides a concise summary of the TOF_{CO} values for various materials. The ZnO catalyst reveals an intermediate concentration of active sites μ, of 9.83•1017 cm^{-2}, yielding a TOF_{CO} value of 0.32 s^{-1}, which can be attributed to its selectivity and j_{CO} at -1.2 V_{RHE}. Composite materials, incorporating Fe-, Co-, and Ni-phases, exhibit a heightened concentration of μ due to their refined morphology and the extensive surface area of the additional phases, encountered at Figure 5.3. Nonetheless, the lower Faradaic Efficiency for CO, FE_{CO}, of these materials, as shown in Figure 5.4F, results in significantly lower TOF_{CO} values: 0.142, 0.215, 0.176 s^{-1} respectively, compared to ZnO. This observation underscores that the ZnO phase is the sole active contributor to CO formation. The Cu/ZnO catalyst boasts the highest TOF_{CO} value of 0.41 s^{-1}, indicating its exceptional intrinsic capability for CO formation. The slightly lower value of μ=8.77•1017 cm^{-2}, in comparison to the ZnO catalyst, can be attributed to its morphology and surface characteristics. This suggests that the Cu phase serves as a co-catalyst in the formation of CO, working in conjunction with the active ZnO phase.

The analysis of the impedance spectra presented in Figure 5.5D of the GDEs, revealed more about the resistance and activity of most of the catalyst-loaded GDEs. The charge transfer resistance R_{ct}, of the materials is relatable with their activity towards ECR. The R_{ct} of the Cu-ZnO GDE stands out with a value of 6 Ω, exhibiting a clear difference from the rest of the materials. The pure ZnO GDE also exhibits a low R_{ct} of 9 Ω, with the rest of the materials exhibiting higher R_{ct}. The latest is related to the catalytic performance observed for these materials, as seen in Figure 4.4F, and the Tafel-Slopes summarized in Figure 5.5B. These changes in the electronic properties of ZnO can be attributed to the simultaneous thermal-oxidative crystallization of ZnO and TMO (transition metal oxide). Smaller ions, like Fe and Co, permeate more easily and cause less stress to the crystalline structure of ZnO, before forming metal oxide islands on the ZnO surface, these ions can also be incorporated into the crystalline lattice. Affecting surface properties, catalytic activity, of the composite catalyst due to the HER favoring nature of these block metals, and important materials properties like resistance.

The catalytic performance of the composite materials is proven to be affected by factors such as catalyst dimensionality, surface chemistry, electron transport pathway, and morphology.[70] Concurring to the influence of the metal-oxide heterostructures in the ECR activity.

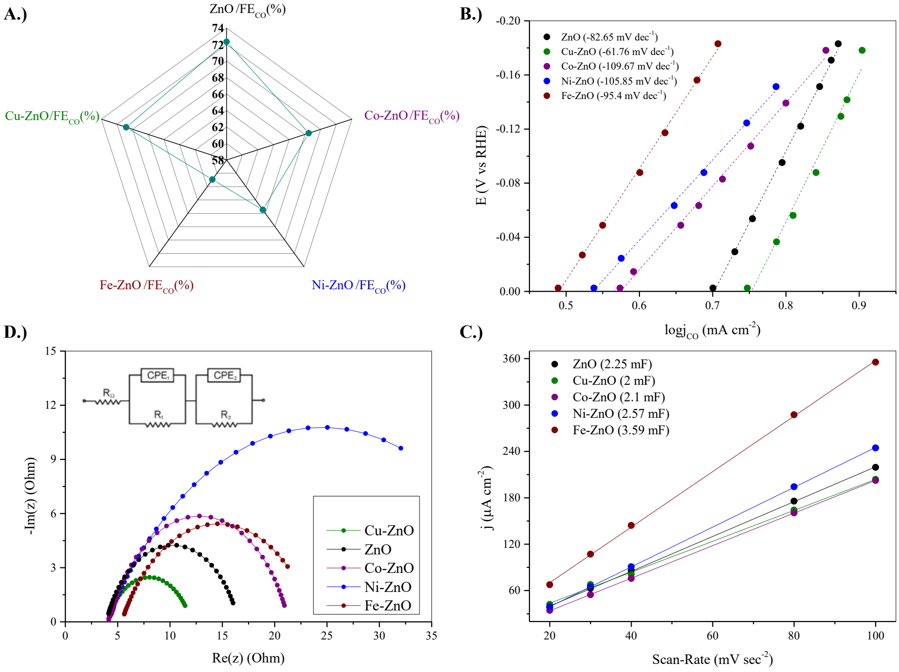

Figure 5.5. Comparison of the ECR activity and electrochemical characterization of the catalyst-loaded GDEs. A.) Comparison of the FE_{CO} at -1.2 V_{RHE}, B.) Tafel-Slopes for the CO formation, C.) ECSA assessment, measured in an H-cell in 0.1 M $NaClO_4$ Ar saturated, D.) Potentiostatic impedance measurements of the catalyst-loaded GDEs, measured at on-set potential.

5.5 Stability of Catalysts in the Flow-Cell

The electrocatalytic activity can be related to the coordination mode with which the molecules interact on the material's surface. These materials preferentially induce the coordination of CO_2 by oxygen atoms in either a monodentate or bidentate mode. Under these conditions, it is expected that ZnO exists in partly its metallic form and the form of zincate, ZnO_2^{-2}, species[110,213], making it favorable for two-electron transfer and supporting the formation of the observed products CO, HCOOH, and H_2. As illustrated by the excerpts' of Pourbaix , found in App. B Figure B5, the high ECR overpotential induces the non-faradaic transition of both ZnO and the d-block metal-oxide phases into their metallic. In the work of Sikam et al.[103], d-block metals of Cu and Co are expected to contribute to a higher rate of H_2 and $HCOO^-$ formation for that 20% of these phases, while Ni and Fe have prone catalytic centers for HER[214–216]. The ECR activity of the materials, exhibited in Figure 5.4F, and the Tafel analysis, presented in Figure 5.5B, concur with the correlation of CO selectivity and the availability of ZnO-catalytic centers regarding kinetics and onset potential. This indicates that the ZnO acts as an active catalyst substrate, interacting with the introduced heterostructured phases.

To assess the stability of the catalyst materials, we performed ECR at 100 mA cm^{-2}. High current densities are required for applicable ECR systems. In Figure 5.6A, the stability of the different catalyst-coated GDEs is summarized. The electrochemical response of the materials reveals that the addition of the d-block affects the lifetime of the catalyst-loaded GDEs differently. The ZnO-GDE exhibits a stability of 20 h at a FE$_{CO}$ of 75%. The drop in the FE$_{CO}$ can be associated with the eventual depletion observed in the ZnO-phase, observed in Figure 6B, which is mainly responsible for the CO selectivity.[83,85] The agglomerate formation, observed in Figure B7 of App. B, over the ZnO-GDE during ECR is further deteriorating its activity. Introducing Co-, Ni- and Fe-oxide phases worsens the catalyst stability towards CO. These GDEs were stable only for 12 h of ECR, recording lower FE$_{CO}$ of 65%, 55%, and 50 % respectively. These heterostructured catalysts' lower FE$_{CO}$ and stability are related to the influence of the Co-, Ni- and Fe-phases that inhibit the CO formation, shown in Figure 5.4. The depletion of the ZnO phase is also accompanied by the formation of Ni-, Co- & Fe-metal and metal-hydroxides phases, as shown in Figure 5.6B, that promote the HER.

The Cu-ZnO GDE exhibited the most extended stability of 30 h, recording FE$_{CO}$ of 77%. We reason that adding Cu promotes the CO formation path, as illustrated in Figure 5.4F&5.5B, along with the ZnO phase.[123,217] The post-mortem XRD in Figure 5.6B, indicates that the Cu-Zn-O heterostructure retains the Cu-phase and partially the catalytically active ZnO phase. The SEM/EDX characterization in Figure 5.6C&D illustrates gradual formation aggregation and phase separation through the ECR. These morphological alterations induce further the degradation of the GDE. The SEM/EDX of the initial Cu-ZnO GDE, in Figure B6 of App. B, reveals a uniform phase distribution throughout the catalyst layer. After 15 h of ECR, partial separation of the Cu- and Zn-phases is recorded, with the Cu-phase being coordinated in separate agglomerations, as clearly shown in Figure 5.6C. After 30 h of electrolysis, shown in Figure 5.6D, phase separation is strongly observed, with the Zn- and Cu-phase forming large agglomerates, as depicted in Figures B6 & B7 of App. B.

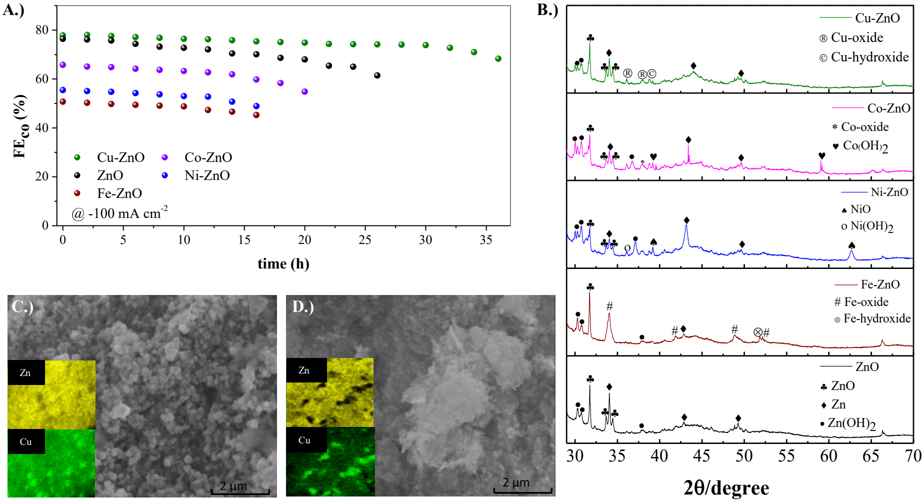

Figure 5.6. Effect of ECR stability at constant current of -100 mA cm^{-2} ECR. A.) Stability of the catalyst-loaded GDEs in the Flow-Cell, B.) XRD diffractogram of the catalyst-coated GDEs

after the stability experiment, C.) SEM and EDX images of the Cu-ZnO GDE after 15 h of electrolysis, D.) SEM and EDX images of the Cu-ZnO GDE after 30 h of electrolysis.

5.6 Chapter Summary

This study focuses on investigating the ECR performance and electrochemical characteristics of composite materials consisting of ZnO-d-block metal oxide ZnO@MO, heterostructures. The ECR performance of the catalysts was correlated with their structural and physicochemical characteristics, which resulted from the interactions between the substrate and the different phases. Our results demonstrate that ZnO is an efficient active catalyst substrate with tunable ECR properties depending on the formed heterostructures. The Cu-ZnO catalyst exhibited a stability of 30 hours and a selectivity of 77% for CO at a current density of 100 mA cm^{-2} in a Flow-Cell configuration, overshooting the durability of similar ECR materials. This study pioneers the use of ZnO@MO structures as ECR catalysts, providing fundamental insights into their functionality in ECR processes. Furthermore, by evaluating the stability and performance of the catalysts in a Flow-Cell configuration, we demonstrate their potential for practical and stable ECR in flow-by electrolyzer setups.

Chapter 6:

Ternary ZnCeAg Oxide for Stable & Selective CO_2-to-CO conversion

Disclaimer:

The content of this chapter is a product of an already published scientific work. The content of which is reproduced for the purposes of this Thesis and under permission of the corresponding Journal.

Ilias Stamatelos, Fabian Scheepers, Joachim Pasel, Cao-Thang Dinh, Detlef Stolten,

Applied Catalysis B: Environment and Energy,Volume 353,2024,124062,

ISSN 0926-3373

6.1 Abstract

Catalyst materials with high stability and selectivity, based on inexpensive materials, are vital for practical electrochemical carbon dioxide, CO_2, reduction, ECR. In this study, we report ternary Zn-Ce-Ag catalysts for selective and stable CO_2-to-CO conversion at high current densities on a large scale. We found that ZnO catalysts are relatively selective for CO_2-to-CO conversion, but are only stable for less than 20 hours at current densities over 100 mA cm^{-2} due to the reduction of the Zn oxide phase, along with the ECR. Combining ZnO with CeO_2 significantly improves the stability of the catalysts, maintaining a CO Faradaic efficiency FE_{CO}, of 80% for 100 hours at the current density of 200 mA cm^{-2}. By introducing a small amount of silver, less than 10 wt.%, to form ternary Ag-Ce-Zn catalysts, both CO selectivity and stability are significantly improved: the developed catalysts exhibit a high FE_{CO} of 90% at 200 mA cm^{-2} and are stable for 200 hours. We attribute the enhanced CO_2-to-CO conversion efficiency to the abundance of stable interfacial areas of various metal-oxide interactions, which are critical for ECR. To demonstrate the potential for practical application, we performed the ECR in a large electrochemical cell, with an active surface area of 100 cm^2. The system delivers an FE_{CO} of 90% at 200 mA cm^{-2} for an extended operation time of 200 hours.

6.2 Introduction

As seen in Chapter 5, an additional phase can synergistically catalyze the ECR and also actively contribute to stabilizing the ZnO phase. Cerium oxide, CeO_2, has attracted a lot of research interest as an active catalyst-supporting material, with applications for the ECR.[131–133] CeO_2 actively contributes to the ECR by enhancing CO_2 adsorption[134] which is a major step for the overall ECR process.[135,136] CeO_2-based ECR catalysts can be used for the formation of a wide range of products, depending on their constitution.[108,137] The role of the CeO_2-phase was initially demonstrated by Hong et. al.[143] using a copper-cerium oxide, Cu-CeO_2 catalyst. They demonstrated that the Cu/CeO_2 interface stabilizes the Cu^{+1} state during the ECR, promoting C_{2+} selectivity.[144] Zong et.al.[145] further studied the role of the CeO_2-phase in a zinc-cerium oxide, ZnO/CeO_2 catalyst. The strong Zn-O-Ce interactions stabilized the Zn^{+2} oxidation state during ECR. The ZnO/CeO_2 catalyst recorded a maximum partial current density for the CO j_{CO} of -150 mA cm^{-2} with nonetheless limited stability. Fabrication of silver–metal oxide, Ag-MO, interfaces is known to promote CO_2–to–CO conversion.[124] Bhalothia et al.[127] synthesized a ZnO/Ag catalyst of high CO selectivity. The Ag–ZnO heterostructure promotes high ECR activity.[128] The function of the Ag–MO heterostructure was highlighted by Fu et.al.[138] Using a Cr_2O_3/Ag catalyst, they recorded high FE_{CO} of 90% and prolonged ECR stability of more than 25 h. The CO_2–to–CO turnover was promoted over the Ag–Cr_2O_3 interphase. During ECR, the Cr_2O_3 substrate maintained the Cr^{+3} state, eliminating structural degradation and favoring prolonged ECR.

In this work, we developed selective and stable Zn-Ce-Ag oxide catalysts for the CO_2-to-CO conversion. Exploiting the ECR-active ZnO and Ag phases, we sought to increase the CO selectivity. The stable CeO_2-phase aided in stabilizing the oxidation state of Zn^{+2} and moderating the agglomeration rate of the ZnO- and Ag-phase. Our materials were evaluated directly in a membrane electrode assembly (MEA) electrolyzer, allowing us to operate at high current densities. Initially, we optimized the structure and composition of the ZnO-CeO_2 catalyst, which exhibited a CO Faradaic Efficiency, FE_{CO} of 80% at 200 mA cm^{-2} for 100 h. By adorning this material with a low amount of about 5% of silver, Ag, we recorded 90% FE_{CO} at 200 mA cm^{-2} for 200 h of continuous ECR operation. We exhibited the real application potential of our material by showcasing its performance in a large MEA electrolyzer with a 100 cm^2 active area recording equally high performance and stability.

6.3 ZnCe Oxide Characterization

As described in 6.2, the co-precipitation, cp, of the Zn and Ce precursors was used to form a uniform material with a high contact area of the different Zn and Ce phases. The materials resulting from this approach were cpZnCe(5–20), about their Ce content , exhibited in App. C at Figure C1. Sequential precipitation was used, aiming for the formation of a core-shell, cs, structure of the Zn and Ce phases.

High-Resolution Transition Electron Microscopy (HRTEM) was used to characterize the morphology and structure of Zn-Ce oxide catalysts synthesized using the two different synthesis approaches, summarized in Figure 6.1a-d. With the gradual co-precipitation approach, a composite oxide with two distinct phases of ZnO and CeO_2 was obtained, as shown in Figure 6.1a, b. The distinct phases in the form of nanoclusters of 5 nm radius were evenly distributed throughout the material's structure, shown in Figure C5 of App. C. This mixed-phase structure enabled a large interfacial area between the ZnO and CeO_2 crystal planes. The catalyst synthesized via the sequential precipitation approach results in a core-shell architecture, captured in Figure 6.1c, d. The material consisted of CeO_2 nanoparticle cores covered with a thick layer of 12 nm thickness, of ZnO. The HRTEM images, presented in Figure 5.1a-d, suggest that the preparation of the different materials was successfully undertaken.

To confirm the crystalline structures of the catalysts, we performed X-ray diffraction (XRD) on the catalyst materials, presented in Figure 6.1e. The ZnO phase was identified as having a hexagonal wurtzite structure, as to the PDF No. 01-089-0510, whereas the CeO_2 phase could be indexed into the fluorite-hexagonal structure, according to PDF No. 34-0394 & 23-1048[218,219], in both samples, regardless of the synthesis methods used.

The Survey XPS of csZnCe10 and cpZnCe10, found in App. C Figure C2, reveals differences in the surface constitution of each catalyst. The actual elemental composition of all samples was determined using Inductively Coupled Plasma–Optical Emission Spectroscopy (ICP–OES) and can be accurately seen in Table C1. The cpZnCe10 surface exhibits a similar Zn/Ce ratio, with the elemental constitution recorded for the material. This feature reveals a uniform phase distribution over the material's core and surface, adopted through the co-precipitation synthesis approach. The Survey-XPS of the csZnCe10 reveals a much lower Ce concentration over the catalyst's surface. The different composition of the csZnCe10 surface relates to its core-shell architecture, adopted through the sequential precipitation approach, majorly exposing the ZnO phase. The comparison of the Zn-XPS, shown in Figure 6.1f, of the two samples suggests that Zn remains in the same oxidation state. The Zn–XPS for the cpZnCe10 displays a shifting of 0.7 eV to the Zn–2p3 binding energy (BE). The close contact of the ZnO and CeO_2 phases, at their interface, induces changes in the local electronic structure of the catalyst.[86,197–199] These interfacial interactions are mainly present in the cpZnCe10 material, owing to its architecture, illustrated in Figure 6.1a, b. The sequential depletion of the electronic density around the Zn atoms is associated with the positive shift in the BE. The O-XPS, found in Figure 6.1g, of the materials displays a clear difference like the O-bonds over the materials' surfaces. For the cpZnCe10, the O1s-spectrum reveals a high concentration of oxygen disorders, ascribed collectively to vacancies and lattice defects V_o. The O1s-spectrum of the csZnCe10 suggests a lower concentration of V_o. The surface bonded-O was mainly spent in the Zn-oxide phase, accounting for 34.3%, which was related to the observed core-shell architecture of the sample, shown in Figure 6.1 c, d. The positive 0.3 eV shift of the O-XPS for the cpZnCe10, indicates depletion of the e^- density around the O-atoms. This behavior is associated with the strong interfacial interactions between the ZnO and CeO_2 phases, which is favored in the cpZnCe10 morphology.[139,140] The Ce–XPS of Figure 6.1h, indicates that Ce exists in the Ce^{+3} and Ce^{+4} states at different concentrations for each sample. The Ce–XPS of the cpZnCe10 records higher Ce^{+3} concentrations of 21.3%, than in the csZnCe10, which correlates with the increased V_O observed in the cpZnCe10, as seen in Figure 6.1g. The absence of a binding energy shift implies that the Ce atoms experience a similar coordination environment, for the different architectures. This suggests that the interactions between the ZnO and CeO_2 phases primarily affect the Zn and O species, leading to detectable shifts in their XPS signals. While the Ce atoms remain relatively unaffected. owning to the Ce redox stability.[141,142] The differences in the coordination environment and electronic state of the surface atoms are majorly attributed to the different architectures of the materials, promoting synergistic interactions among the ZnO and CeO_2 phases.[145,134,220]

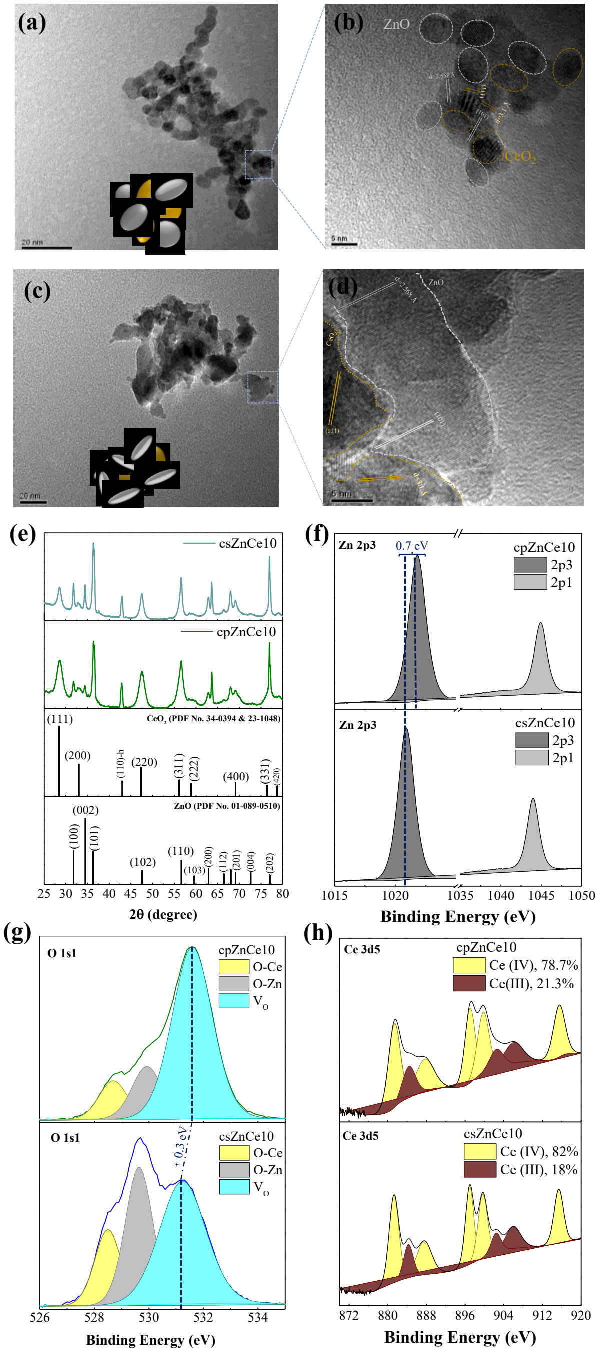

Figure 6.1. Structural and physicochemical characterization of the Zn–Ce oxide catalyst powders. (a, b) HRTEM images of the cpZnCe10 catalyst powder, (c, d) HRTEM images of the csZnCe10 catalyst powder, (e) XRD diffractogram of the catalyst materials, (f) high-resolution zinc Zn2p3 XPS of the catalysts, (g) high-resolution oxygen O1s1 XPS of the catalysts, (h) high-resolution cerium Ce3d5 XPS of the catalysts.

6.4 Performance & Stability of the ZnCe Oxide in the MEA

We evaluated the electrocatalytic activity of the prepared samples for the ECR using an MEA cell. To evaluate the performance of the catalysts in the MEA cell configuration, we constructed the MEA from catalyst-coated GDEs, an anion exchange membrane, and an IrOx/Ti felt as the anode. First, we sought to study the effect of the Ce amount on the ECR performance in both catalyst structures. In the cp samples, increasing the amount of Ce led to an increase in the reaction overpotential η, and a decrease in the FE for CO, FE_{CO}, as summarized in App. C Figure C3. Among the cp samples, cpZnCe10-GDE exhibited the highest partial current density for CO j_{CO}, of 140 mA cm^{-2}. A similar trend was observed in cs samples, with csZnCe10-GDE exhibiting the highest performance, as shown in App. C Figure C4, recording 150 mA cm^{-2} of j_{CO}. The effect of catalyst structure on the ECR performance is summarized in Figure 6.2a–d. The introduction of Ce resulted in a partial reduction of the FE_{CO} in comparison to the ZnO-GDE, found in Figure 6.2a–c. The csZnCe10-GDE records a higher j_{CO} of 150 mA cm^{-2} and lower overpotential, shown in Figure 6.2d.

To investigate the effect of the introduction of Ce on the stability of ZnO-based catalysts, we applied a constant current density of 200 mA cm^{-2} to the MEA electrolyzer and monitored the changes in the products over time. As shown in Figure 6.2e, ZnO–GDE was stable for less than 10 hours at a current density of 200 mA cm^{-2}. The introduction of Ce greatly improves the stability of the catalyst, effectively prolonging the ECR's lifetime in comparison to the pure ZnO–GDE. The cpZnCe10-GDE maintained a stable FE_{CO} of over 70% for more than 90 hours.

Following the long-term ECR, the GDEs were analyzed using Scanning-Electron-Microscopy (SEM) and HRTEM. The long-term ECR was halted for the csZnCe10-GDE at 85 h and for the cpZnCe10-GDE at 105 h, when the FE_{CO} dropped below 70%. As exhibited in App. C Figure C6, both the cpZnCe10 and csZnCe10 GDES form agglomerates, of 50 nm diameter, comprising mainly small CeO_2 particles, of 10 nm size, and the Zn/ZnO phase. Potassium carbonate salts are also a reason for the GDE's degradation, derived from the 0.1 M $KHCO_3$ anolyte. The salt formation relates to the potassium ions', K^+, crossover, through the AEM, towards the cathode GDE. The SEM and HRTEM images of the post-mortem csZnCe10-GDEs, found in the App. C Figure C6, reveals that the catalyst was severely agglomerated, forming large agglomerates of ~100 nm. The architecture appears to have had a direct impact on the stability of the GDEs. The post-mortem XRD analysis of the cpZnCe10 and csZnCe10 GDEs, revealed that ZnO was partially converted into metallic-Zn, whereas the CeO_2 phase remained practically stable.

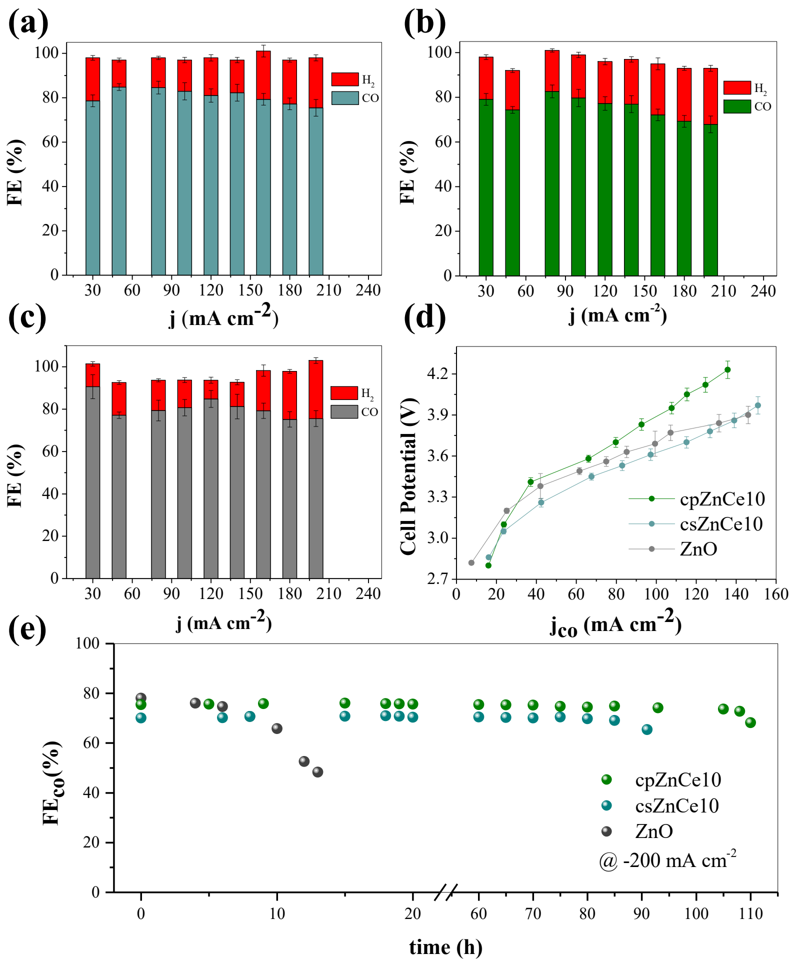

Figure 6.2. ECR performance in the MEA of the Zn–Ce oxide catalyst-loaded GDEs and of the baseline ZnO–GDE. (a) Selectivity FE_{CO} of the csZnCe10–GDE, (b) selectivity FE_{CO} of the cpZnCe10-GDE, (c) selectivity FE_{CO} of the ZnO–GDE, (d) polarization curves, in terms of the partial current density for CO j_{CO}, of the different catalyst-loaded GDEs, (e) stability of the catalyst-loaded GDEs in the MEA system at 200 mA cm^{-2}.

6.5 ZnCeAg Oxide Characterization

The results presented above suggest that adding Cerium oxide can stabilize ZnO catalysts for ECR, but that this also decreases CO selectivity. To improve CO selectivity, we doped Zn–Ce catalysts with silver, Ag, which is known for its selective CO formation, and has also been used for that purpose in various metal/metal-oxide catalysts.[104,125,138] To form Ag NPs over the Zn–Ce surface, we employed an additional precipitation step, explained in Chapter 3. The Ag introduced into the cpZnCe10 and csZnCe10 samples resulted in the Ag@cpZnCe10 and Ag@csZnCe10 samples, respectively.

The XRD patterns of the Ag@cpZnCe10 and Ag@csZnCe10 samples, presented in Figure 6.3a, reveal that the ZnO phase remains coordinated in the wurtzite system, according to PDF No. 01-089-0510, and the CeO_2 is indexed into the fluorite-hexagonal structure, as to PDF No. 34-0394 & 23-1048. As was also observed, in Figure 6.1e, for the cpZnCe10 and csZnCe10 samples. The Ag introduced is in its metallic form, coordinated in the face-centered cubic, fcc, system, according to PDF No. 04-0783. The HRTEM images in Figure 6.3b–d of the Ag@cpZnCe10 catalyst, confirm the presence of Ag NPs smaller than 5 nm. The Ag@cpZnCe10 morphology induces the contact of the phases in the ternary oxide. Figure 6.3e represents the final morphology of the Ag@cpZnCe10, as observed from the HRTEM. This architecture favors the contact of the Zn and Ce phases, consisting the core of the material, and with the Ag phase, comprising the shell of the material.

Raman spectroscopy was employed to provide more details regarding the metal/metal-oxide interactions in the catalyst materials. The Raman spectra, presented in Figure 6.3f, of all of the samples reveal the main characteristic peaks of the Zn–O, attributed to wurtzite-structured ZnO [221], with a distinct peak even in the ternary oxide samples. The broadening of the Zn–O peak in ternary oxides is attributed to interactions with Ag–O, which results in Raman peaks occurring at closely neighboring wavenumbers. The CeO_2 phase exhibits distinct excitation peaks, attributed to the Ce–O, fluorite structure, vibrations.[222–226] However, in the Ag@csZncs10 sample, the fluorite excitation peak is attenuated due to the broad multi-phonon Raman peak. The Raman spectra of the cpZnCe10 sample exhibited additional excitation peaks, corresponding to a high concentration of V_o and lattice defects in the material, observed at 650 and 1090 cm^{-1} respectively. The spectra of the Ag@csZnCe10 and Ag@cpZnCe10 samples indicate strong Zn–Ag–O[127,178,179] interactions in both materials.[180–182] The Ag@cpZnCe10 spectrum records the additional D_2 peak at 900 cm^{-1}, ascribed to Ag–Ce–O interactions, revealing a high contact area across all of its phases. [178,227–231]

The high-resolution Ag-XPS in Figure 6.3g, exhibits a positive shift of 0.9 eV in the Ag-3d5 binding energy (BE) attributed to the Ag@cpZnCe10 catalyst. This behavior suggests strong Ag–O between Ag and oxygen atoms from the ZnO-CeO_2 matrix. The Ag–Ce–O Raman interactions in Figure 6.3h, also contribute further to the shifting of the BE. These interactions could involve the formation of bonds of a similar nature or surface coordination complexes, shifting the charge density around the Ag-atoms.[177] The high-resolution O-XPS of the materials in Figure 6.3h, reveals higher concentrations of V_o than in the Ag@csZnCe10 spectra. This behavior agrees with the high concentration of V_o observed in the Raman spectra of the Ag@cpZnCe10 and the cpZnCe10 matrix. The positive shift of the O-XPS signal for the Ag@cpZnCe10 in Figure 6.1g, is consistent with the shift observed for the O-XPS of the cpZnCe10 matrix. The larger 0.5 eV shift of the Ag@cpZnCe10, O-XPS in Figure 6.3h, is associated with the additional interaction of the Ag-atoms with the O-species. The interactions between the Ag and the ZnO-CeO_2 matrix led to the creation of additional V_o in the material. The presence of V_o alters the electronic environment of neighboring O-atoms, leading to the positive shift of the spectra.

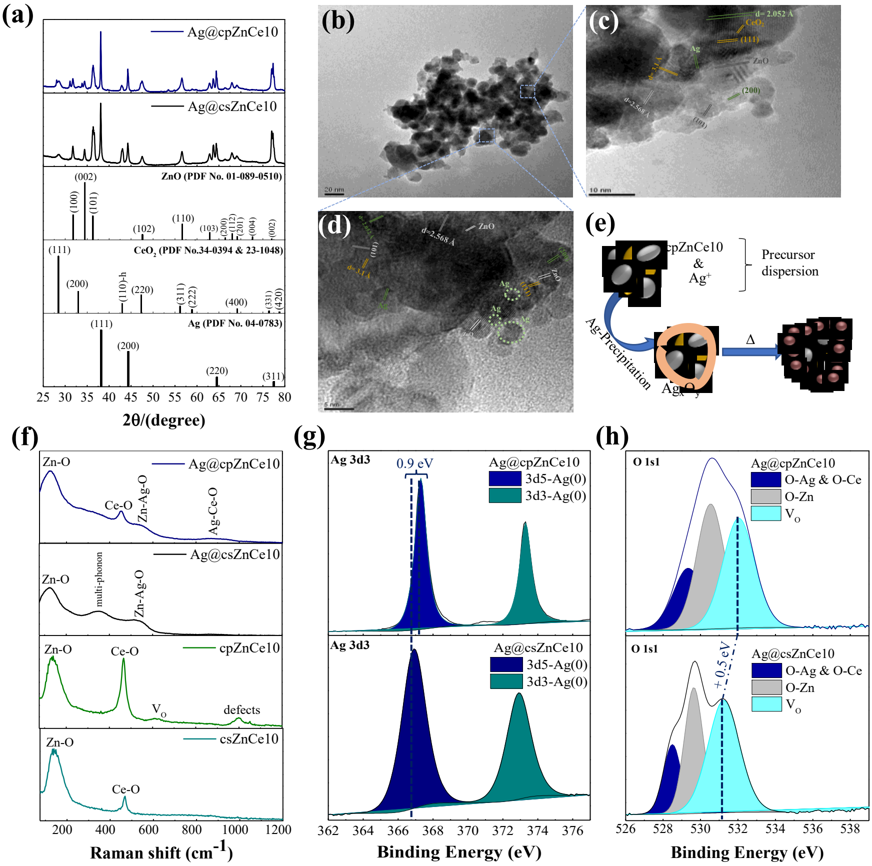

Figure 6.3. Structural and physicochemical characterization of the Zn–Ce–Ag oxide catalyst powders. (a) XRD diffractogram of the different catalyst powders, (b–d) HRTEM images of the Ag@cpZnCe10 catalyst powder, (e) graphical illustration of the synthesis route for the Ag@cpZnCe10 catalyst, (f) Raman spectra for both the ternary and Zn–Ce oxide catalyst powders, (g) high-resolution oxygen O1s1 XPS of the Ag@cpZnCe10 and Ag@csZnCe10 catalysts, (h) high-resolution silver Ag3d3 XPS of the Ag@cpZnCe10 and Ag@csZnCe10 catalysts.

6.6 Performance of the ZnCeAg Oxide in the MEA

Based on the results presented in section 6.4, we chose cpZnCe10-GDE, which exhibits the highest stability, as the starting material for optimizing the amount of Ag loading in the range of 5–30 wt.%. The addition of Ag over the initial catalyst material drastically increases the FE_{CO}. The variation of the Ag content does not significantly affect the FE_{CO} of the GDEs. On the other hand, Ag loading was found to affect the cell voltage, as shown in the polarization curves, as summarized in App. C Figure C8. A sample with 5wt.% Ag loading shows the lowest overpotential η, and reaches the highest j_{CO}. The potentiostatic electrochemical impedance spectroscopy (PEIS) of these samples, exhibited in App. C Figure C9, reveals that a 5wt%Ag, as in the sample Ag@ZnCe10, exhibits the lowest charge transfer resistance R_{ct}. A higher Ag content increases the catalyst's R_{ct} by inhibiting the electrocatalytic functions of the created metal/metal–

oxide interfaces of the material, seen in Figure 6.3c,f.[129,138] For comparison, we also performed the ECR test using the Ag@csZnCe10 sample derived from the csZnCe10 catalyst covered with Ag, with a 5wt. % content. The PEIS results of our catalyst materials are summarized in App. C Figure C9, illustrate that the function of the metal/metal–oxide interfaces and the presence of Ag actively improves the R_{ct} of the materials, especially that of the Ag@cpZnCe10.

Upon the introduction of Ag over the initial catalyst materials cpZnCe10, csZnCe10, and ZnO, there is a significant improvement in the FE_{CO}, as summarized in Figure 6.4a–c. The catalyst-loaded GDEs reach an FE_{CO} of 90% at a high current density of 200 mA cm^{-2}. The polarization curves shown in Figure 6.4d, indicate that the catalyst materials reach a high j_{CO} of above 150 mA cm^{-2}. The Ag@cpZnCe10-GDE reaches the highest j_{CO} of 180 mA cm^{-2}, introducing at the same time the lowest overpotential for the CO_2-to-CO conversion. The stability of the ternary oxide catalysts, shown in Figure 6.4e, was drastically improved after the introduction of Ag. Both the Ag@cpZnCe10 and Ag@csZnCe10 exhibit drastically improved ECR stability. The Ag@cpZnCe10-GDE recorded the longest ECR stability, of 200 h at 200 mA cm^{-2}, maintaining 90% FE_{CO}. The improved ECR performance of the Ag@cpZnCe10 compared to its cpZnCe10 precursor could be attributed to the effect of Ag in the ternary oxide. The Ag-nanoparticles, formed in the ternary oxide, provide additional active sites, promoting the ECR activity. The Ag@cpZnCe10 morphology favors the formation of additional Zn-Ag-O and Ce-Ag-O interactions, as illustrated in Figure 6.3f, which provide additional ECR active sites, making the Ag@cpZnCe10 the most active catalyst from our ternary oxides.

The measured PEIS of the catalyst-loaded GDEs, summarized in App. C Figure C9, reveals differences in the charge transfer resistance R_{ct} introduced by each catalyst. The Ag@cpZnCe10-GDE introduces the lower R_{ct} of 5.2 Ω, implying a lower ECR overpotential. The material's ECSA, shown in App. C Figure C9, indicates that the Ag-containing samples exhibit higher surface areas than the Ce–Zn oxide counterparts. The Ag@cpZnCe10 has the highest C_{dl}, hence ECSA, implying higher concentrations of catalytically active sites. The Tafel slope analysis of the catalyst-loaded GDEs, presented in App. C Figure C9, suggests that the Ag@cpZnCe10 exhibits the fastest kinetics for the CO with a slope of -42 mV/dec and the highest exchange current density of 4.73 mA cm^{-2}. The Ag@csZnCe10 exhibits lower ECR kinetics than the Ag@csZnCe10, with a slope of -46 mV/dec and R_{ct} of 10.1 Ω. These results indicate that the morphology of the Ag@cpZnCe10 favors the creation of additional Ag-ZnO and Ag-Ce-O interactions as seen in Figure 6.3f, as opposed to the Ag@csZnCe10, further enhancing the performance of the Ag@cpZnCe10. Both the cpZnCe10 and csZnCe10 precursors exhibit lower ECR activity with Tafel-Slopes of -57 mV/dec and -51 mV/dec respectively, and R_{ct} of 22.3 Ω and 18.4 Ω respectively. The faster Tafel kinetics and reduced R_{ct} of the ternary oxide catalysts, support their higher ECR activity shown in Figure 6.2d, e, as a result of the Ag-addition.

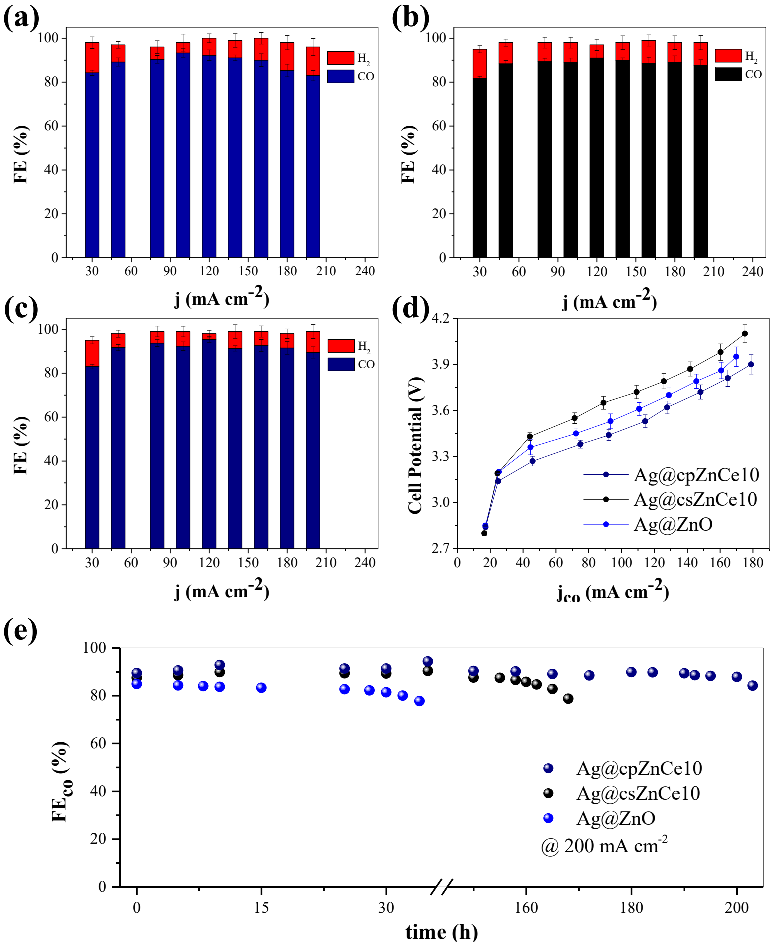

Figure 6.4. ECR performance in the MEA electrolyzer of the Zn–Ce–Ag oxide catalyst-loaded GDEs and of the baseline Ag@ZnO-GDE. (a) Selectivity FE_{CO} of the Ag@cpZnCe10-GDE, (b) selectivity FE_{CO} of the Ag@csZnCe10-GDE, (c) selectivity FE_{CO} of the Ag@ZnO-GDE, (d) polarization curves, in terms of the partial current density of CO j_{CO}, of the different catalyst-loaded GDEs, (e) stability of the catalyst-loaded GDEs in the MEA system at 200 mA cm^{-2}.

6.7 ZnCeAg Oxide Stability in the MEA

The increased Ag@cpZnCe10 ECR stability compelled us to understand the structural changes of the catalysts during the ECR reaction. We characterized the catalysts before and after the stability test. Initially, the Ag@cpZnCe10 exhibited a uniform elemental distribution, as seen in App. C Figure C11, owing to the small particle size comprising each of the catalyst's phases, as seen in Figure 6.3d. After 100 h of ECR, the Ag@cpZnCe10 adopts an altered morphology, shown in Figure 6.5a. Dark-field SEM (DF-SEM) can only differentiate between Ce and Zn/Ag due to their large difference in atomic weights. The DF-SEM reveals that the CeO_2 phase begins separating from the initially homogeneous ternary oxide structure, captured in Figure C11 of App. C. Through the ECR, the Ag and ZnO phases merge into nano-plate structures, whereas the CeO_2 phase coordinates smaller, separated nano-particles. After 200 h of ECR electrolysis, the CeO_2 phase separation becomes more evident, with the CeO_2 agglomerates increasing in size, depicted in Figure 6.5b, c. The ECR-active ZnO–Ag phase retains a nano-plate structure after 200 h of ECR. The XRD diffractograms of the Ag@cpZnCe10 GDEs after 200 h of ECR, shown in Figure 6.5d, indicate the formation of metallic Zn, $Zn(OH)_2$, and $Ce(OH)_3$. These phase transitions, captured in Figure 6.5a–c are correlated with the altered morphology adopted by the Ag@cpZnCe10. The post-ECR high-resolution O1s1-XPS of the Ag@cpZnCe10, in Figure 6.5e, shows that surface oxygen is increasingly spent in bonds of a hydroxide nature. The concentration of the O–Ce and O–Ag surface bonds remains constant, confirming that the Ag and CeO_2 phases retain their stability during the ECR. To investigate the changes that occur in the CeO_2 phase, we examined the effect of 100 h ECR, at 200 mA cm^{-2}, on a CeO_2–GDE. The physicochemical changes of the CeO_2 were isolated on the partial Ce^{+4}-to-Ce^{+3} reduction, shown in Figure C12 of App. C, which took place as a non-Faradaic process alongside the ECR.[147,148] These changes are associated with the CeO_2 phase being coordinated in fine nano-particle structures, seen in App. C Figure C11. The CeO_2 phase underwent the same structural changes in both the Ag@cpZnCe10–GDE and CeO_2–GDE during the ECR.

Despite the Ag@cpZnCe10 and Ag@csZnCe10 catalysts having the same composition, their different architectures appeared to affect their ECR stability significantly. The long-term stability of the Ag@cpZnCe10–GDE indicates that its architecture favors ECR stability. The Ag@csZnCe10 morphology changes in a different aspect during long-term ECR. While Figure C11 of App. C, reveals that the initially structured architecture, coordinates the Ag–ZnO agglomerates after 160 h of ECR, covering the CeO_2 cores. The co-precipitation synthesis approach of the Ag@cpZnCe10 induces the uniform distribution of the phases, promoting the role of the CeO_2 in stabilizing the ECR-active ZnO–Ag phase. It can therefore be illustrated that the ECR-inert CeO_2 assumes the role of a spacer in the composite Ag@cpZnCe10 catalyst. In this respect, the CeO_2 nano-particles withhold the aggregation of the ECR-active ZnO–Ag phase. Observing the *post-mortem* characterization of the Ag@ZnO GDE shown in App. C Figure C11 for after 30 h of ECR, we can see the formation of large agglomerates. The absence of CeO_2 led to the quick aggregation of the ZnO and Ag phases. It becomes clear that the prolonged stability of the Ag@cpZnCe10 is not only based on the CeO_2 stabilizing the ZnO oxidation state through the ECR, as seen through Figure 6.5d, but also on the function of the CeO_2 nanoparticles as spacers, procrastinating agglomerates formation. The stability of the CeO_2 phase and the associated interactions, previously seen in Figure 6.3f, are responsible for the long-term stability of the Ag@cpZnCe10 catalyst. [177]

The Ag@cpZnCe10 GDE exhibits much longer stability than its cpZnCe10 precursor. As previously discussed, the degradation progress is similar for both materials. In the Ag@cpZnCe10, the additional Ag-metallic and the resulting ZnO-Ag & Ag-Ce-O sites provide additional ECR-active sites. These additional phases enhance the ECR during long-time operation, mitigating the effect of the degradation process. Prolonged ECR leads to phase migration, clearly illustrated in Figure 6.5a–c, making the role of CeO_2 as a spacer become less effective. While, as seen in Figure 6.5d, the ZnO–Ag ECR-active phase becomes agglomerated, whereas the formation of Zn/$Zn(OH)_2$ further undermines the ECR activity of the Ag@cpZnCe10 GDE.

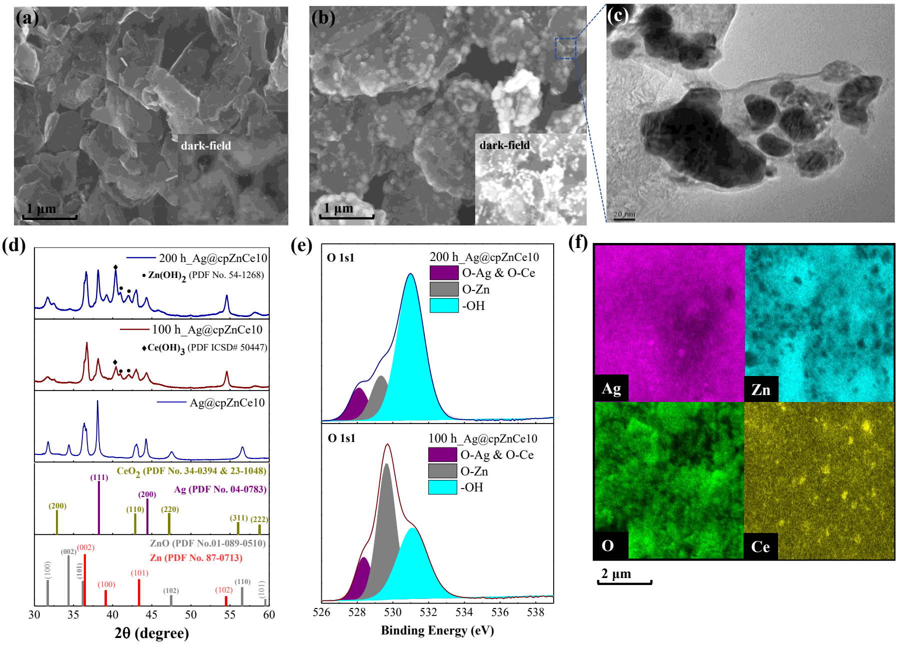

Figure 6.5. Post-mortem characterization of the Ag@cpZnCe10–GDE at different times, after ECR at 200 mA cm^{-2} in an MEA electrolyzer. (a) SEM/dark-field-SEM after 100 h of ECR, (b) SEM/dark-field-SEM after 200 h of ECR, (c) HRTEM image of the catalyst after 200 h of ECR, (d) XRD-diffractograms of the catalyst-loaded GDEs after 200 h and 100 h of ECR, (e) high-resolution O-XPS after 200 h and 100 h of ECR, (f) EDX images of the Ag@cpZnCe10–GDE after 200 h of ECR.

6.8 Performance & Stability in the 100 cm^2 MEA

Electrolysis at elevated temperatures, in the range 60-80 °C, is widely adopted in various electrochemical systems, including PEM, AEM, and Fuel Cells. This practice aims to expedite the reaction kinetics and lower overall cell potential, effectively reducing the energy requirements of the electrochemical process. This renders the process more feasible for real-world industrial applications. For these reasons, we sought to evaluate the performance of our ECR catalysts at higher temperatures. We performed the reaction in a 100 cm^2 electrolyzer to gauge their performance under industrially-relevant conditions. As shown in Figure 6.6a, at room temperature, we obtained similar performance as in the small MEA in terms of both j_{CO} and FE_{CO}. At 40 °C, the FE_{CO} was limited to around 80%, whereas at 60 °C the selectivity was stabilized at 70% for CO, as illustrated in Figure 6.6b&c respectively. Although lower cell potentials, as summarized in Figure 6.6d were obtained at higher temperatures, FE_{CO} decreased due to the increase of HER kinetics along with the ECR. At 60 °C, the maximum j_{CO} recorded was 150 mA cm^{-2} at a full-cell potential of 3.2 V, significantly lower than the potential recorded at room temperature. The effect of the temperature on the system's overpotential was also evident from the galvanostatic impedance spectroscopy (GEIS) performed, and illustrated in Figure C14 of App. C. The GEIS of the MEA exhibited a decrease in the system's electrical resistance, following the temperature increase. We performed the ECR, at room temperature, applying 200 mA cm^{-2} for 200 h to investigate the stability of the scaled-up system. As seen in Figure 6.6e, throughout the electrolysis period, the system maintained a stable FE_{CO} of 90% and an energy efficiency for CO, EE_{CO}, of 27%.

The distribution of the mechanical pressure over the active area of the MEA, illustrated in Figure C14 of App. C, was further assessed. In the large MEA, both the imprints of the cathode and anode flow-fields were visible, indicating a uniform distribution of mechanical pressure, with the pressure in between the cathode's channels being below 3 MPa. This analysis ensures that no mechanical overpressure was built into the 100 cm^2 active area, which could have been caused by the scaled-up cell architecture. The low pressure in the cathode channels ensured no deformation of the soft carbon paper that could prevent CO_2 delivery to the cathode catalyst layer. The uniform pressure distribution indicates that the anode and cathode electrodes were in contact and electrochemically active in the entire active area of the MEA. After long-term ECR electrolysis of 200 h, the resistance of the MEA increased, as exhibited in App. C at Figure C14. This feature is associated with the catalyst's agglomeration and degradation processes, as previously seen in Figure 5.5b, c, along with carbonate precipitants on the cathode catalyst layer, shown in Figure C15 at App. C, undermining the MEA's ECR activity.

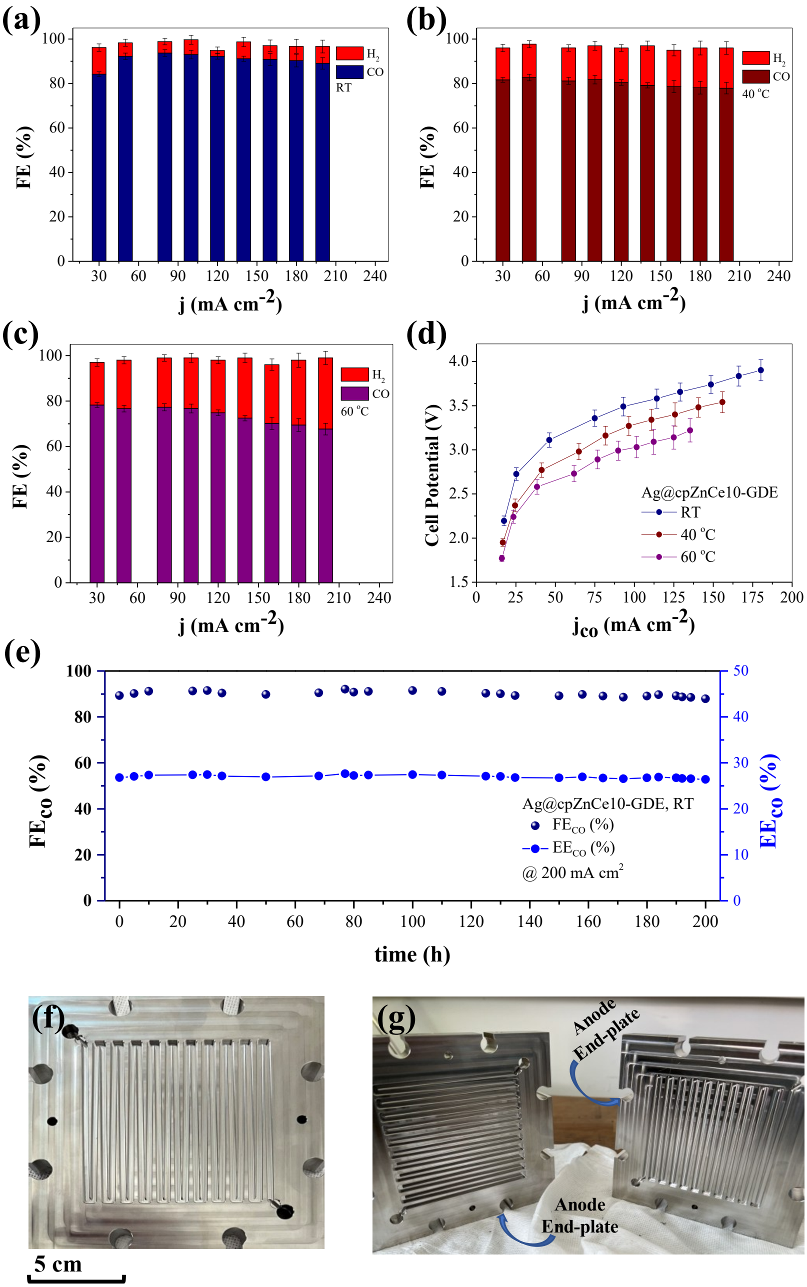

Figure 6.6. ECR performance of the Ag@cpZnCe10-GDE in the large MEA, of 100 cm^2 active area. (a) FE_{CO} of the Ag@cpZnCe10-GDE at room temperature (RT), (b) FE_{CO} of the Ag@cpZnCe10–GDE at 40 ºC, (c) FE_{CO} of the Ag@cpZnCe10-GDE at 40 ºC, (d) polarization curves for j_{CO}, of the Ag@cpZnCe10-GDE at different temperatures, (e) stability of the Ag@cpZnCe10–GDE at 200 mA cm^{-2} at room temperature, (f) image of the flow-field of the 100 cm^2 MEA electrolyzer, (g) image of the two end-plates and current collectors of the 100 cm^2 MEA electrolyzer.

6.9 Chapter Summary

We developed a stable and selective catalyst for CO_2-to-CO conversion based on ternary Zn–Ce–Ag components. We found a composite material of Ce– and Zn–oxide could maintain the ZnO phase, leading to a stable CO_2-to-CO conversion at 200 mA cm^{-2} for 100 hours. However, the FE_{CO} of the Zn–Ce binary catalysts was relatively low, below 80% in the tested current range of 100–200 mA cm^{-2}. To improve the CO selectivity of Zn–Ce, we developed Zn–Ce–Ag ternary oxide catalysts that exhibited a stable FE_{CO} of 90% at 200 mA cm^{-2} for 200 hours. The strong interactions between the different phases cooperatively enhanced the ECR performance, while our results suggested that the enhanced stability of the catalyst mainly originated from the contribution of the CeO_2 phase. The redox stability of CeO_2 aided in both maintaining its structure and also stabilizing the ZnO, during ECR. Most importantly, CeO_2 acted as a spacer moderating the agglomeration of the active Zn–O–Ag phase, prolonging the catalyst's lifetime. We further demonstrated the potential for the practical application of our Zn–Ce–Ag catalysts by performing ECR using a large MEA electrolyzer with a 100 cm^2 active area. A similar trend was also observed with the large-scale electrolyzer in which the catalysts were not only selective, recording FE_{CO} of 90%, but also stable for 200 hours at the tested current density of 200 mA cm^{-2}, significantly surpassing the ECR performance of known catalysts. Our work represents a significant step towards practical CO_2-to-CO conversion utilizing inexpensive catalysts.

Chapter 7:
Summary & Discussion of the Main Results

This section summarizes and analyzes the main results from chapters 4-6 of the thesis, aiming to clarify our research goals and achievements. The comparison of our findings with the existing literature focuses on assessing our electrochemical carbon dioxide reduction, ECR, methodology's robustness compared to the current state-of-the-art. Comparing our results with existing literature helps gauge the novelty and significance of our work. This contributes to our understanding of ECR and highlights our methodology's advancements in the field.

7.1 Optimizing the ZnO ECR Activity.

The stability and activity of ZnO and its allotropes for the ECR were examined in this study. The catalytic process of ZnO was ascribed to its diverse morphologies, including nanoparticles, nanorods, nanosheets, and random shapes, with ZnO nanorods exhibiting the highest activity. They emerged as the most efficient catalyst, boosting CO Faradaic efficiency FE_{CO} to over 80%, in the current density range of 50-160 mA cm^{-2}, in both flow-cell and membrane electrode assembly (MEA) reactors. Their high FE_{CO} was attributed to their elevated surface area, crystallinity, and oxygen vacancies.

Nevertheless, a gradual decline in CO selectivity was noted over time, particularly at high current densities, owing to the depletion of the ZnO phase. This feature is associated with the gradual reduction of the ZnO phase into Zn metallic, due to the high cathodic potential. To tackle this challenge, an innovative *in-situ* regeneration strategy was devised.

The employed strategy encompassed initial continuous ECR operation until the FE_{CO} dropped below 80%, signifying catalyst degradation. Subsequently, two Cyclic Voltammetries (CV) were executed to oxidize metallic Zn to the ZnO phase. This regenerated the catalytic activity, with stable FE_{CO} above 80% for 100 hours at a current density of 160 mA cm^{-2}.

Overall, this *in-situ* regeneration strategy successfully countered the degradation of ZnO catalysts, prolonging their structural integrity and catalytic activity during ECR. Our strategy managed to record ECR performance that, as illustrated in Figure 7.1, surpassed the durability of various alternative materials used for CO_2-to-CO formation. These findings hold promise for practical applications in sustainable fuel and chemical traits production, contributing to the advancement of practical CO_2 utilization technologies and fostering a more sustainable future.

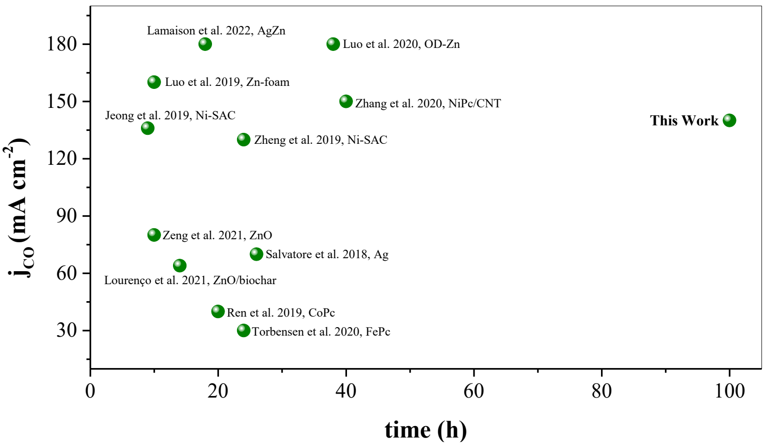

Figure 7.1. Comparison of the stability and partial current density for CO j_{CO} for state-of-the-art materials and high-performance Zn-based catalysts, for the ECR. Performance recorded in flow-cell and MEA electrolyzers.

7.2 ECR activity of ZnO-based heterostructures

Our previous research has highlighted the depletion of the ZnO phase as a key issue in stability during ECR. To stabilize ZnO without compromising CO selectivity, we investigated heterostructured catalysts with d-block metals: Cu, Ni, Co, Fe. We aimed to stabilize the ZnO phase, achieving continuous electrolysis at high current densities, without the need for *in-situ* regeneration, by reversing the cell bias.

These materials displayed varying electrochemical traits, influenced by the type and distribution of the d-block metals oxides, and their interactions with the ZnO phase. The ECR activity of each composite material greatly depended on the heterostructures created. Affecting key parameters for the catalyst's ECR performance, like product distribution & selectivity, active surface area, and durability.

Compared to pure ZnO, the Cu-ZnO catalyst showed a three-fold improvement in stability. The addition of d-block metals, like Cu, Ni, Co, and Fe, enhanced catalyst stability by resisting degradation during ECR. The Cu-ZnO catalyst, lasting 30 hours at 100 mA cm^{-2} in a flow cell, exhibited the longest stability versus other Zn-based heterostructured catalysts, as depicted in Figure 7.2. This was attributed to synergistic effects between added metals and ZnO, mitigating site degradation and preventing phase separation.

Unlike prior studies that focused on single-component or binary metal catalysts, ours explores composite heterostructures, offering tunable selectivity and improved stability. It advances understanding of composite catalyst materials, promising for sustainable energy conversion and environmental remediation.

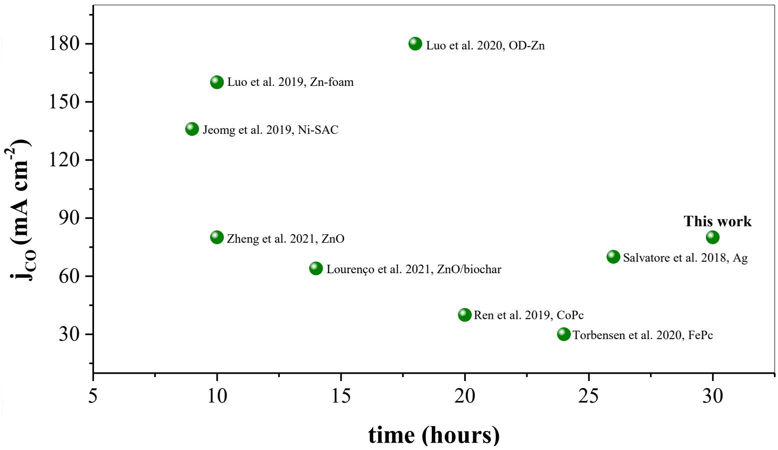

Figure 7.2. Comparison of the stability and partial current density for CO j_{CO} for state-of-the-art materials Zn-based heterostructured catalysts, for the ECR. Performance recorded in flow-cell type electrolyzers.

7.3 Stable ternary Zn-based oxide

In this study, CeO_2 was found to play a crucial role in stabilizing the ZnO interface, thereby maintaining the ZnO phase and leading to a stable CO_2-to-CO conversion. Strong Zn-O-Ce interactions were observed to stabilize the Zn^{2+} oxidation state during the electrochemical CO_2 reduction process, ECR, contributing to the stability and selectivity of the catalyst for CO_2-to-CO conversion. Additionally, the chemical stability of CeO_2 was noted to allow it to maintain its structure during ECR, which in turn contributed to the stability and selectivity of the catalyst. The morphology of the composite materials was found to favor a strong contact among the ZnO and CeO_2 phases. CeO_2 contributed to enhancing CO_2 adsorption, which is a major step for the overall ECR process.

The different phases in the catalyst, such as CeO_2, ZnO, and Ag, were observed to play a role in prolonging the lifetime of the catalyst. The redox stability of CeO_2 was found to aid in maintaining its electrochemical performance, contributing to the stability and selectivity of the catalyst. Additionally, the strong interactions between the different phases were noted to cooperatively enhance the ECR performance, leading to prolonged stability and improved faradaic efficiency for CO_2-to-CO conversion. The performance and stability of ternary oxide catalysts were drastically improved after the introduction of Ag. The ZnO/Ag heterostructure provided a higher concentration of ECR active sites, promoting the CO_2-to-CO conversion. The observed interactions of the CeO_2 with the Ag and ZnO phases, hindered the agglomerate formation, improving the stability of the catalyst.

In conclusion, the study demonstrated that the interactions of the different CeO_2, ZnO, and Ag phases in the catalyst significantly enhanced the stability, selectivity, and efficiency of the ECR process. Our recent findings, capture in Figure 7.3, represent a remarkable leap forward from the current state-of-the-art in the sustainable conversion of CO_2-to-CO conversion. This is evidenced by its successful integration into a 100 cm^2 MEA, demonstrating its potential for real-world application.

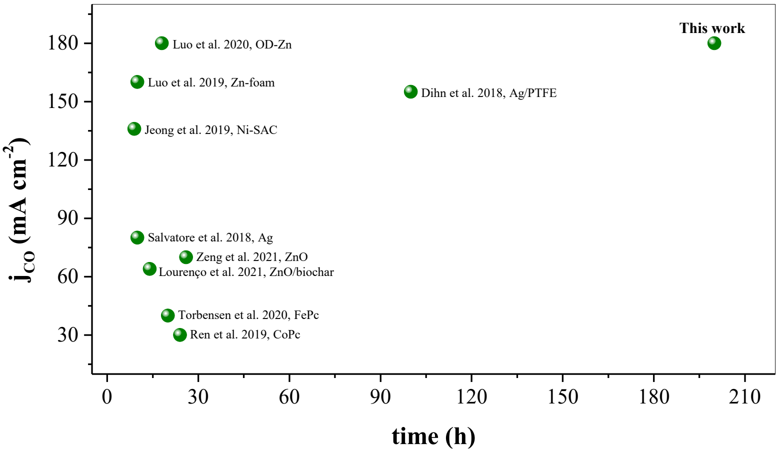

Figure 7.3. Comparison of the stability and partial current density for CO j_{CO} for state-of-the-art materials for the ECR. Performance recorded in flow-cell and MEA electrolyzers.

Chapter 8:
Conclusions

Overall, this work stemmed from the urgent need to develop efficient and stable catalysts for the electrochemical CO_2 reduction, ECR, a critical step in addressing global climate change. The choice to work with Zn-based materials was driven by their abundance, low cost, and promising catalytic properties, making them an attractive candidate for CO_2 reduction applications.

Throughout this work, highly efficient catalysts for the CO_2-to-CO conversion were engineered. By initially optimizing the ECR activity of plain ZnO, in Chapter 4, the groundwork for subsequent progress was laid, with significant advancements in the ECR performance being recorded in the process. Heterostructured ZnO with d-block metals was crafted in Chapter 5, yielding valuable insights into the function and properties of such materials and providing crucial insights into their tunable properties. Ultimately, the robust and stable ternary ZnCeAg-oxide was developed in Chapter 6, marking a significant milestone in the pursuit of selective and stable ECR and a breakthrough in the development of stable and efficient catalysts for CO_2 reduction.

Throughout this work, the transition was consistently made from fundamental optimization and exploration of novel heterostructures to the ultimate development of a highly stable and functioning ECR system. The scaled-up MEA of 100 cm^2 showcased in Chapter 6, represents a critical step towards practical application. This demonstration underscores the potential for large-scale implementation of our catalyst, highlighting its significance in real-world ECR systems.

The overall significance of our work lies in its contribution to addressing the main challenges in the field of ECR. By developing efficient and stable catalysts, we have made significant progress in overcoming the crucial bottlenecks of selectivity & stability, toward more sustainable and economically viable ECR systems.

In summary, this research has not only yielded valuable scientific insights but has also made significant strides in addressing the pressing challenges in the field of CO_2 reduction. The development of efficient Zn-based catalysts and the successful demonstration of their practical utility marks a pivotal advancement in the quest for sustainable CO_2 conversion technologies.

References

(1) Podrojková, N.; Sans, V.; Oriňak, A.; Oriňaková, R. Recent Developments in the Modelling of Heterogeneous Catalysts for CO2 Conversion to Chemicals. *ChemCatChem* **2020**, *12* (7), 1802–1825. https://doi.org/10.1002/cctc.201901879.

(2) Garg, S.; Li, M.; Weber, A. Z.; Ge, L.; Li, L.; Rudolph, V.; Wang, G.; Rufford, T. E. Advances and Challenges in Electrochemical CO2 Reduction Processes: An Engineering and Design Perspective Looking beyond New Catalyst Materials. *J. Mater. Chem. A* **2020**, *8* (4), 1511–1544. https://doi.org/10.1039/C9TA13298H.

(3) Birdja, Y. Y.; Pérez-Gallent, E.; Figueiredo, M. C.; Göttle, A. J.; Calle-Vallejo, F.; Koper, M. T. M. Advances and Challenges in Understanding the Electrocatalytic Conversion of Carbon Dioxide to Fuels. *Nat Energy* **2019**, *4* (9), 732–745. https://doi.org/10.1038/s41560-019-0450-y.

(4) Yang, Q.; Wu, Q.; Liu, Y.; Luo, S.; Wu, X.; Zhao, X.; Zou, H.; Long, B.; Chen, W.; Liao, Y.; Li, L.; Shen, P. K.; Duan, L.; Quan, Z. Novel Bi-Doped Amorphous SnOx Nanoshells for Efficient Electrochemical CO2 Reduction into Formate at Low Overpotentials. *Advanced Materials* **2020**, *32* (36), 2002822. https://doi.org/10.1002/adma.202002822.

(5) Jouny, M.; Luc, W.; Jiao, F. Correction to “General Techno-Economic Analysis of CO2 Electrolysis Systems.” *Ind. Eng. Chem. Res.* **2020**, *59* (16), 8121–8123. https://doi.org/10.1021/acs.iecr.0c01513.

(6) Park, S.; Wijaya, D. T.; Na, J.; Lee, C. W. Towards the Large-Scale Electrochemical Reduction of Carbon Dioxide. *Catalysts* **2021**, *11* (2), 253. https://doi.org/10.3390/catal11020253.

(7) Verma, S.; Kim, B.; Jhong, H.-R. “Molly”; Ma, S.; Kenis, P. J. A. A Gross-Margin Model for Defining Technoeconomic Benchmarks in the Electroreduction of CO2. *ChemSusChem* **2016**, *9* (15), 1972–1979. https://doi.org/10.1002/cssc.201600394.

(8) Philips, M. F.; Gruter, G.-J. M.; Koper, M. T. M.; Schouten, K. J. P. Optimizing the Electrochemical Reduction of CO2 to Formate: A State-of-the-Art Analysis. *ACS Sustainable Chem. Eng.* **2020**, *8* (41), 15430–15444. https://doi.org/10.1021/acssuschemeng.0c05215.

(9) Hori, Y.; Wakebe, H.; Tsukamoto, T.; Koga, O. Electrocatalytic Process of CO Selectivity in Electrochemical Reduction of CO2 at Metal Electrodes in Aqueous Media. *Electrochimica Acta* **1994**, *39* (11), 1833–1839. https://doi.org/10.1016/0013-4686(94)85172-7.

(10) Yang, K.; Kas, R.; Smith, W. A.; Burdyny, T. Role of the Carbon-Based Gas Diffusion Layer on Flooding in a Gas Diffusion Electrode Cell for Electrochemical CO2 Reduction. *ACS Energy Lett.* **2021**, *6* (1), 33–40. https://doi.org/10.1021/acsenergylett.0c02184.

(11) Ozden, A.; Liu, Y.; Dinh, C.-T.; Li, J.; Ou, P.; García de Arquer, F. P.; Sargent, E. H.; Sinton, D. Gold Adparticles on Silver Combine Low Overpotential and High Selectivity in Electrochemical CO2 Conversion. *ACS Appl. Energy Mater.* **2021**, *4* (8), 7504–7512. https://doi.org/10.1021/acsaem.1c01577.

(12) Kauffman, D. R.; Alfonso, D.; Matranga, C.; Qian, H.; Jin, R. Experimental and Computational Investigation of Au25 Clusters and CO2: A Unique Interaction and Enhanced Electrocatalytic Activity. *J. Am. Chem. Soc.* **2012**, *134* (24), 10237–10243. https://doi.org/10.1021/ja303259q.

(13) Rosen, J.; Hutchings, G. S.; Lu, Q.; Forest, R. V.; Moore, A.; Jiao, F. Electrodeposited Zn Dendrites with Enhanced CO Selectivity for Electrocatalytic CO2 Reduction. *ACS Catal.* **2015**, *5* (8), 4586–4591. https://doi.org/10.1021/acscatal.5b00922.

(14) Weekes, D. M.; Salvatore, D. A.; Reyes, A.; Huang, A.; Berlinguette, C. P. Electrolytic CO2 Reduction in a Flow Cell. *Acc. Chem. Res.* **2018**, *51* (4), 910–918. https://doi.org/10.1021/acs.accounts.8b00010.

(15) Zheng, T.; Jiang, K.; Wang, H. Recent Advances in Electrochemical CO2-to-CO Conversion on Heterogeneous Catalysts. *Advanced Materials* **2018**, *30* (48), 1802066. https://doi.org/10.1002/adma.201802066.

(16) He, M.; Sun, Y.; Han, B. Green Carbon Science: Efficient Carbon Resource Processing, Utilization, and Recycling towards Carbon Neutrality. *Angewandte Chemie* **2022**, *134* (15), e202112835. https://doi.org/10.1002/ange.202112835.

(17) Zheng, T.; Zhang, M.; Wu, L.; Guo, S.; Liu, X.; Zhao, J.; Xue, W.; Li, J.; Liu, C.; Li, X.; Jiang, Q.; Bao, J.; Zeng, J.; Yu, T.; Xia, C. Upcycling CO2 into Energy-Rich Long-Chain Compounds via Electrochemical and Metabolic Engineering. *Nat Catal* **2022**, *5* (5), 388–396. https://doi.org/10.1038/s41929-022-00775-6.

(18) Behr, A.; Agar, D. W.; Jörissen, J.; Vorholt, A. J. Elektrochemische Verfahren. In *Einführung in die Technische Chemie*; Behr, A., Agar, D. W., Jörissen, J., Vorholt, A. J., Eds.; Springer: Berlin, Heidelberg, 2016; pp 253–270. https://doi.org/10.1007/978-3-662-52856-3_19.

(19) Schmickler, W.; Santos, E. Theoretical Considerations of Electron-Transfer Reactions. In *Interfacial Electrochemistry*; Schmickler, W., Santos, E., Eds.; Springer: Berlin, Heidelberg, 2010; pp 99–115. https://doi.org/10.1007/978-3-642-04937-8_10.

(20) Zoski, C. G. *Handbook of Electrochemistry*; Elsevier, 2006.

(21) Verma, S.; Kim, B.; Jhong, H.-R. “Molly”; Ma, S.; Kenis, P. J. A. A Gross-Margin Model for Defining Technoeconomic Benchmarks in the Electroreduction of CO2. *ChemSusChem* **2016**, *9* (15), 1972–1979. https://doi.org/10.1002/cssc.201600394.

(22) Kortlever, R.; Shen, J.; Schouten, K. J. P.; Calle-Vallejo, F.; Koper, M. T. M. Catalysts and Reaction Pathways for the Electrochemical Reduction of Carbon Dioxide. *J. Phys. Chem. Lett.* **2015**, *6* (20), 4073–4082. https://doi.org/10.1021/acs.jpclett.5b01559.

(23) Durst, J.; Siebel, A.; Simon, C.; Hasché, F.; Herranz, J.; Gasteiger, H. A. New Insights into the Electrochemical Hydrogen Oxidation and Evolution Reaction Mechanism. *Energy Environ. Sci.* **2014**, *7* (7), 2255–2260. https://doi.org/10.1039/C4EE00440J.

(24) Gattrell, M.; Gupta, N.; Co, A. A Review of the Aqueous Electrochemical Reduction of CO2 to Hydrocarbons at Copper. *Journal of Electroanalytical Chemistry* **2006**, *594* (1), 1–19. https://doi.org/10.1016/j.jelechem.2006.05.013.

(25) Handoko, A. D.; Wei, F.; Jenndy; Yeo, B. S.; Seh, Z. W. Understanding Heterogeneous Electrocatalytic Carbon Dioxide Reduction through Operando Techniques. *Nat Catal* **2018**, *1* (12), 922–934. https://doi.org/10.1038/s41929-018-0182-6.

(26) Peterson, A. A.; Abild-Pedersen, F.; Studt, F.; Rossmeisl, J.; Nørskov, J. K. How Copper Catalyzes the Electroreduction of Carbon Dioxide into Hydrocarbon Fuels. *Energy Environ. Sci.* **2010**, *3* (9), 1311–1315. https://doi.org/10.1039/C0EE00071J.

(27) Li, W.; Tian, H.; Ma, L.; Wang, Y.; Liu, X.; Gao, X. Low-Temperature Water Electrolysis: Fundamentals, Progress, and New Strategies. *Materials Advances* **2022**, *3* (14), 5598–5644. https://doi.org/10.1039/D2MA00185C.

(28) Gupta, K.; Bersani, M.; Darr, J. A. Highly Efficient Electro-Reduction of CO2 to Formic Acid by Nano-Copper. *J. Mater. Chem. A* **2016**, *4* (36), 13786–13794. https://doi.org/10.1039/C6TA04874A.

(29) Zhu, S.; Ren, X.; Li, X.; Niu, X.; Wang, M.; Xu, S.; Wang, Z.; Han, Y.; Wang, Q. Core-Shell ZnO@Cu2O as Catalyst to Enhance the Electrochemical Reduction of Carbon Dioxide to C2 Products. *Catalysts* **2021**, *11* (5), 535. https://doi.org/10.3390/catal11050535.

(30) Zhang, T.; Li, Z.; Zhang, J.; Wu, J. Enhance CO2-to-C2+ Products Yield through Spatial Management of CO Transport in Cu/ZnO Tandem Electrodes. *Journal of Catalysis* **2020**, *387*, 163–169. https://doi.org/10.1016/j.jcat.2020.05.002.

(31) Qin, B.; Li, Y.; Fu, H.; Wang, H.; Chen, S.; Liu, Z.; Peng, F. Electrochemical Reduction of CO2 into Tunable Syngas Production by Regulating the Crystal Facets of Earth-Abundant Zn Catalyst. *ACS Appl. Mater. Interfaces* **2018**, *10* (24), 20530–20539. https://doi.org/10.1021/acsami.8b04809.

(32) Peterson, A. A.; Nørskov, J. K. Activity Descriptors for CO2 Electroreduction to Methane on Transition-Metal Catalysts. *J. Phys. Chem. Lett.* **2012**, *3* (2), 251–258. https://doi.org/10.1021/jz201461p.

(33) Liu, X.; Xiao, J.; Peng, H.; Hong, X.; Chan, K.; Nørskov, J. K. Understanding Trends in Electrochemical Carbon Dioxide Reduction Rates. *Nature Communications* **2017**, *8* (1), 15438. https://doi.org/10.1038/ncomms15438.

(34) Hansen, H. A.; Varley, J. B.; Peterson, A. A.; Nørskov, J. K. Understanding Trends in the Electrocatalytic Activity of Metals and Enzymes for CO2 Reduction to CO. *J. Phys. Chem. Lett.* **2013**, *4* (3), 388–392. https://doi.org/10.1021/jz3021155.

(35) Cheng, T.; Xiao, H.; Goddard, W. A. I. Reaction Mechanisms for the Electrochemical Reduction of CO2 to CO and Formate on the Cu(100) Surface at 298 K from Quantum Mechanics Free Energy Calculations with Explicit Water. *J. Am. Chem. Soc.* **2016**, *138* (42), 13802–13805. https://doi.org/10.1021/jacs.6b08534.

(36) Liang, S.; Huang, L.; Gao, Y.; Wang, Q.; Liu, B. Electrochemical Reduction of CO2 to CO over Transition Metal/N-Doped Carbon Catalysts: The Active Sites and Reaction Mechanism. *Advanced Science* **2021**, *8* (24), 2102886. https://doi.org/10.1002/advs.202102886.

(37) Deng, W.; Zhang, P.; Seger, B.; Gong, J. Unraveling the Rate-Limiting Step of Two-Electron Transfer Electrochemical Reduction of Carbon Dioxide. *Nat Commun* **2022**, *13* (1), 803. https://doi.org/10.1038/s41467-022-28436-z.

(38) Kari, J.; Olsen, J. P.; Jensen, K.; Badino, S. F.; Krogh, K. B. R. M.; Borch, K.; Westh, P. Sabatier Principle for Interfacial (Heterogeneous) Enzyme Catalysis. *ACS Catal.* **2018**, *8* (12), 11966–11972. https://doi.org/10.1021/acscatal.8b03547.

(39) Medford, A. J.; Vojvodic, A.; Hummelshøj, J. S.; Voss, J.; Abild-Pedersen, F.; Studt, F.; Bligaard, T.; Nilsson, A.; Nørskov, J. K. From the Sabatier Principle to a Predictive Theory of Transition-Metal Heterogeneous Catalysis. *Journal of Catalysis* **2015**, *328*, 36–42. https://doi.org/10.1016/j.jcat.2014.12.033.

(40) Zhu, D. D.; Liu, J. L.; Qiao, S. Z. Recent Advances in Inorganic Heterogeneous Electrocatalysts for Reduction of Carbon Dioxide. *Advanced Materials* **2016**, *28* (18), 3423–3452. https://doi.org/10.1002/adma.201504766.

(41) Ďurovič, M.; Hnát, J.; Bouzek, K. Electrocatalysts for the Hydrogen Evolution Reaction in Alkaline and Neutral Media. A Comparative Review. *Journal of Power Sources* **2021**, *493*, 229708. https://doi.org/10.1016/j.jpowsour.2021.229708.

(42) Jakšić, J. M.; Vojnović, M. V.; Krstajić, N. V. Kinetic Analysis of Hydrogen Evolution at Ni–Mo Alloy Electrodes. *Electrochimica Acta* **2000**, *45* (25), 4151–4158. https://doi.org/10.1016/S0013-4686(00)00549-1.

(43) Conway, B. E.; Tilak, B. V. Interfacial Processes Involving Electrocatalytic Evolution and Oxidation of H2, and the Role of Chemisorbed H. *Electrochimica Acta* **2002**, *47* (22), 3571–3594. https://doi.org/10.1016/S0013-4686(02)00329-8.

(44) Marrero, T. R.; Mason, E. A. Gaseous Diffusion Coefficients. *Journal of Physical and Chemical Reference Data* **2009**, *1* (1), 3–118. https://doi.org/10.1063/1.3253094.

(45) Casebolt DiDomenico, R.; Levine, K.; Reimanis, L.; Abruña, H. D.; Hanrath, T. Mechanistic Insights into the Formation of CO and C2 Products in Electrochemical CO2 Reduction–The Role of Sequential Charge Transfer and Chemical Reactions. *ACS Catal.* **2023**, *13* (7), 4938–4948. https://doi.org/10.1021/acscatal.2c06043.

(46) Zheng, W.; Wang, D.; Zhang, Y.; Zheng, S.; Yang, B.; Li, Z.; Rodriguez, R. D.; Zhang, T.; Lei, L.; Yao, S.; Hou, Y. Promoting Industrial-Level CO2 Electroreduction Kinetics via

Accelerating Proton Feeding on a Metal-Free Aerogel Electrocatalyst. *Nano Energy* **2023**, *105*, 107980. https://doi.org/10.1016/j.nanoen.2022.107980.

(47) Yang, W.; Xue, Z.; Yang, J.; Xian, J.; Liu, Q.; Fan, Y.; Zheng, K.; Liao, P.; Su, H.; Liu, Q.; Li, G.; Su, C.-Y. Fe Nanoparticles Embedded in N-Doped Porous Carbon for Enhanced Electrocatalytic CO2 Reduction and Zn-CO2 Battery. *Chinese Journal of Catalysis* **2023**, *48*, 185–194. https://doi.org/10.1016/S1872-2067(23)64415-8.

(48) Bagemihl, I.; Cammann, L.; Pérez-Fortes, M.; van Steijn, V.; van Ommen, J. R. Techno-Economic Assessment of CO2 Electrolysis: How Interdependencies between Model Variables Propagate Across Different Modeling Scales. *ACS Sustainable Chem. Eng.* **2023**, *11* (27), 10130–10141. https://doi.org/10.1021/acssuschemeng.3c02226.

(49) Koh, J. H.; Jeon, H. S.; Jee, M. S.; Nursanto, E. B.; Lee, H.; Hwang, Y. J.; Min, B. K. Oxygen Plasma Induced Hierarchically Structured Gold Electrocatalyst for Selective Reduction of Carbon Dioxide to Carbon Monoxide. *J. Phys. Chem. C* **2015**, *119* (2), 883–889. https://doi.org/10.1021/jp509967m.

(50) Jee, M. S.; Kim, H.; Jeon, H. S.; Chae, K. H.; Cho, J.; Min, B. K.; Hwang, Y. J. Stable Surface Oxygen on Nanostructured Silver for Efficient CO2 Electroreduction. *Catalysis Today* **2017**, *288*, 48–53. https://doi.org/10.1016/j.cattod.2016.09.026.

(51) Mistry, H.; Choi, Y.-W.; Bagger, A.; Scholten, F.; Bonifacio, C. S.; Sinev, I.; Divins, N. J.; Zegkinoglou, I.; Jeon, H. S.; Kisslinger, K.; Stach, E. A.; Yang, J. C.; Rossmeisl, J.; Roldan Cuenya, B. Enhanced Carbon Dioxide Electroreduction to Carbon Monoxide over Defect-Rich Plasma-Activated Silver Catalysts. *Angewandte Chemie International Edition* **2017**, *56* (38), 11394–11398. https://doi.org/10.1002/anie.201704613.

(52) Gao, D.; Zhou, H.; Wang, J.; Miao, S.; Yang, F.; Wang, G.; Wang, J.; Bao, X. Size-Dependent Electrocatalytic Reduction of CO2 over Pd Nanoparticles. *J. Am. Chem. Soc.* **2015**, *137* (13), 4288–4291. https://doi.org/10.1021/jacs.5b00046.

(53) Huang, H.; Jia, H.; Liu, Z.; Gao, P.; Zhao, J.; Luo, Z.; Yang, J.; Zeng, J. Understanding of Strain Effects in the Electrochemical Reduction of CO2: Using Pd Nanostructures as an Ideal Platform. *Angewandte Chemie International Edition* **2017**, *56* (13), 3594–3598. https://doi.org/10.1002/anie.201612617.

(54) Chen, Y.; Li, C. W.; Kanan, M. W. Aqueous CO2 Reduction at Very Low Overpotential on Oxide-Derived Au Nanoparticles. *J. Am. Chem. Soc.* **2012**, *134* (49), 19969–19972. https://doi.org/10.1021/ja309317u.

(55) Ma, M.; Trześniewski, B. J.; Xie, J.; Smith, W. A. Selective and Efficient Reduction of Carbon Dioxide to Carbon Monoxide on Oxide-Derived Nanostructured Silver Electrocatalysts. *Angewandte Chemie International Edition* **2016**, *55* (33), 9748–9752. https://doi.org/10.1002/anie.201604654.

(56) Jiang, X.; Cai, F.; Gao, D.; Dong, J.; Miao, S.; Wang, G.; Bao, X. Electrocatalytic Reduction of Carbon Dioxide over Reduced Nanoporous Zinc Oxide. *Electrochemistry Communications* **2016**, *68*, 67–70. https://doi.org/10.1016/j.elecom.2016.05.003.

(57) Luo, W.; Zhang, J.; Li, M.; Züttel, A. Boosting CO Production in Electrocatalytic CO_2 Reduction on Highly Porous Zn Catalysts. *ACS Catal.* **2019**, *9* (5), 3783–3791. https://doi.org/10.1021/acscatal.8b05109.

(58) Qi, Z.; Biener, J.; Biener, M. Surface Oxide-Derived Nanoporous Gold Catalysts for Electrochemical CO_2-to-CO Reduction. *ACS Appl. Energy Mater.* **2019**, *2* (11), 7717–7721. https://doi.org/10.1021/acsaem.9b00355.

(59) Verma, S.; Lu, X.; Ma, S.; Masel, R. I.; Kenis, P. J. A. The Effect of Electrolyte Composition on the Electroreduction of CO2 to CO on Ag Based Gas Diffusion Electrodes. *Phys. Chem. Chem. Phys.* **2016**, *18* (10), 7075–7084. https://doi.org/10.1039/C5CP05665A.

(60) Rosen, B. A.; Salehi-Khojin, A.; Thorson, M. R.; Zhu, W.; Whipple, D. T.; Kenis, P. J. A.; Masel, R. I. Ionic Liquid–Mediated Selective Conversion of CO2 to CO at Low

Overpotentials. *Science* **2011**, *334* (6056), 643–644. https://doi.org/10.1126/science.1209786.

(61) Dufek, E. J.; Lister, T. E.; McIlwain, M. E. Influence of Electrolytes and Membranes on Cell Operation for Syn-Gas Production. *Electrochem. Solid-State Lett.* **2012**, *15* (4), B48. https://doi.org/10.1149/2.010204esl.

(62) Yamamoto, T.; Tryk, D. A.; Fujishima, A.; Ohata, H. Production of Syngas plus Oxygen from CO2 in a Gas-Diffusion Electrode-Based Electrolytic Cell. *Electrochimica Acta* **2002**, *47* (20), 3327–3334. https://doi.org/10.1016/S0013-4686(02)00253-0.

(63) Dinh, C.-T.; García de Arquer, F. P.; Sinton, D.; Sargent, E. H. High Rate, Selective, and Stable Electroreduction of CO2 to CO in Basic and Neutral Media. *ACS Energy Lett.* **2018**, *3* (11), 2835–2840. https://doi.org/10.1021/acsenergylett.8b01734.

(64) Monteiro, M. C. O.; Philips, M. F.; Schouten, K. J. P.; Koper, M. T. M. Efficiency and Selectivity of CO2 Reduction to CO on Gold Gas Diffusion Electrodes in Acidic Media. *Nat Commun* **2021**, *12* (1), 4943. https://doi.org/10.1038/s41467-021-24936-6.

(65) Sun, L.; Reddu, V.; Fisher, A. C.; Wang, X. Electrocatalytic Reduction of Carbon Dioxide: Opportunities with Heterogeneous Molecular Catalysts. *Energy Environ. Sci.* **2020**, *13* (2), 374–403. https://doi.org/10.1039/C9EE03660A.

(66) Torbensen, K.; Han, C.; Boudy, B.; von Wolff, N.; Bertail, C.; Braun, W.; Robert, M. Iron Porphyrin Allows Fast and Selective Electrocatalytic Conversion of CO2 to CO in a Flow Cell. *Chemistry – A European Journal* **2020**, *26* (14), 3034–3038. https://doi.org/10.1002/chem.202000160.

(67) Ren, S.; Joulié, D.; Salvatore, D.; Torbensen, K.; Wang, M.; Robert, M.; Berlinguette, C. P. Molecular Electrocatalysts Can Mediate Fast, Selective CO2 Reduction in a Flow Cell. *Science* **2019**, *365* (6451), 367–369. https://doi.org/10.1126/science.aax4608.

(68) Jeong, H.-Y.; Balamurugan, M.; Choutipalli, V. S. K.; Jeong, E.; Subramanian, V.; Sim, U.; Nam, K. T. Achieving Highly Efficient CO2 to CO Electroreduction Exceeding 300 mA Cm−2 with Single-Atom Nickel Electrocatalysts. *J. Mater. Chem. A* **2019**, *7* (17), 10651–10661. https://doi.org/10.1039/C9TA02405K.

(69) Zheng, T.; Jiang, K.; Ta, N.; Hu, Y.; Zeng, J.; Liu, J.; Wang, H. Large-Scale and Highly Selective CO2 Electrocatalytic Reduction on Nickel Single-Atom Catalyst. *Joule* **2019**, *3* (1), 265–278. https://doi.org/10.1016/j.joule.2018.10.015.

(70) Lin, J.; Yan, S.; Zhang, C.; Hu, Q.; Cheng, Z. Electroreduction of CO2 toward High Current Density. *Processes* **2022**, *10* (5), 826. https://doi.org/10.3390/pr10050826.

(71) Hori, Y.; Kikuchi, K.; Suzuki, S. Production of Co and Ch4 in Electrochemical Reduction of Co2 at Metal Electrodes in Aqueous Hydrogencarbonate Solution. *Chem. Lett.* **1985**, *14* (11), 1695–1698. https://doi.org/10.1246/cl.1985.1695.

(72) Hori, Y. Electrochemical CO2 Reduction on Metal Electrodes. In *Modern Aspects of Electrochemistry*; Vayenas, C. G., White, R. E., Gamboa-Aldeco, M. E., Eds.; Modern Aspects of Electrochemistry; Springer: New York, NY, 2008; pp 89–189. https://doi.org/10.1007/978-0-387-49489-0_3.

(73) Li, J.; Fan, H.; Jia, X. Multilayered ZnO Nanosheets with 3D Porous Architectures: Synthesis and Gas Sensing Application. *J. Phys. Chem. C* **2010**, *114* (35), 14684–14691. https://doi.org/10.1021/jp100792c.

(74) Chubarov, M.; Choudhury, T. H.; Zhang, X.; Redwing, J. M. In-Plane x-Ray Diffraction for Characterization of Monolayer and Few-Layer Transition Metal Dichalcogenide Films. *Nanotechnology* **2018**, *29* (5), 055706. https://doi.org/10.1088/1361-6528/aaa1bd.

(75) Zong, X.; Jin, Y.; Li, Y.; Zhang, X.; Zhang, S.; Xie, H.; Zhang, J.; Xiong, Y. Morphology-Controllable ZnO Catalysts Enriched with Oxygen-Vacancies for Boosting CO2 Electroreduction to CO. *Journal of CO2 Utilization* **2022**, *61*, 102051. https://doi.org/10.1016/j.jcou.2022.102051.

(76) Bera, S.; Mittal, V. K.; Venkata Krishnan, R.; Saravanan, T.; Velmurugan, S.; Nagarajan, K.; Narasimhan, S. V. XPS Analysis of UxCe1−xO2±δ and Determination of Oxygen to Metal Ratio. *Journal of Nuclear Materials* **2009**, *393* (1), 120–125. https://doi.org/10.1016/j.jnucmat.2009.05.015.

(77) Kadari, A.; Schemme, T.; Kadri, D.; Wollschläger, J. XPS and Morphological Properties of Cr2O3 Thin Films Grown by Thermal Evaporation Method. *Results in Physics* **2017**, *7*, 3124–3129. https://doi.org/10.1016/j.rinp.2017.08.036.

(78) Qin, B.; Li, Y.; Fu, H.; Wang, H.; Chen, S.; Liu, Z.; Peng, F. Electrochemical Reduction of CO2 into Tunable Syngas Production by Regulating the Crystal Facets of Earth-Abundant Zn Catalyst. *ACS Appl. Mater. Interfaces* **2018**, *10* (24), 20530–20539. https://doi.org/10.1021/acsami.8b04809.

(79) Won, D. H.; Shin, H.; Koh, J.; Chung, J.; Lee, H. S.; Kim, H.; Woo, S. I. Highly Efficient, Selective, and Stable CO2 Electroreduction on a Hexagonal Zn Catalyst. *Angewandte Chemie International Edition* **2016**, *55* (32), 9297–9300. https://doi.org/10.1002/anie.201602888.

(80) Xiao, J.; Gao, M.-R.; Liu, S.; Luo, J.-L. Hexagonal Zn Nanoplates Enclosed by Zn(100) and Zn(002) Facets for Highly Selective CO2 Electroreduction to CO. *ACS Appl. Mater. Interfaces* **2020**, *12* (28), 31431–31438. https://doi.org/10.1021/acsami.0c06891.

(81) Luo, W.; Zhang, J.; Li, M.; Züttel, A. Boosting CO Production in Electrocatalytic CO2 Reduction on Highly Porous Zn Catalysts. *ACS Catal.* **2019**, *9* (5), 3783–3791. https://doi.org/10.1021/acscatal.8b05109.

(82) Wang, J.; Zhu, Z.; Wei, X.; Li, Z.; Chen, J. S.; Wu, R.; Wei, Z. Hydrogen-Mediated Synthesis of 3D Hierarchical Porous Zinc Catalyst for CO2 Electroreduction with High Current Density. *J. Phys. Chem. C* **2021**. https://doi.org/10.1021/acs.jpcc.1c07498.

(83) Luo, W.; Zhang, Q.; Zhang, J.; Moioli, E.; Zhao, K.; Züttel, A. Electrochemical Reconstruction of ZnO for Selective Reduction of CO2 to CO. *Applied Catalysis B: Environmental* **2020**, *273*, 119060. https://doi.org/10.1016/j.apcatb.2020.119060.

(84) Han, K.; Ngene, P.; Jongh, P. de. Structure Dependent Product Selectivity for CO2 Electroreduction on ZnO Derived Catalysts. *ChemCatChem n/a* (n/a). https://doi.org/10.1002/cctc.202001710.

(85) Xiang, Q.; Li, F.; Wang, J.; Chen, W.; Miao, Q.; Zhang, Q.; Tao, P.; Song, C.; Shang, W.; Zhu, H.; Deng, T.; Wu, J. Heterostructure of ZnO Nanosheets/Zn with a Highly Enhanced Edge Surface for Efficient CO2 Electrochemical Reduction to CO. *ACS Appl. Mater. Interfaces* **2021**, *13* (9), 10837–10844. https://doi.org/10.1021/acsami.0c20302.

(86) Geng, Z.; Kong, X.; Chen, W.; Su, H.; Liu, Y.; Cai, F.; Wang, G.; Zeng, J. Oxygen Vacancies in ZnO Nanosheets Enhance CO2 Electrochemical Reduction to CO. *Angewandte Chemie International Edition* **2018**, *57* (21), 6054–6059. https://doi.org/10.1002/anie.201711255.

(87) Nguyen, D. L. T.; Jee, M. S.; Won, D. H.; Jung, H.; Oh, H.-S.; Min, B. K.; Hwang, Y. J. Selective CO2 Reduction on Zinc Electrocatalyst: The Effect of Zinc Oxidation State Induced by Pretreatment Environment. *ACS Sustainable Chem. Eng.* **2017**, *5* (12), 11377–11386. https://doi.org/10.1021/acssuschemeng.7b02460.

(88) Zeng, J.; Fontana, M.; Sacco, A.; Sassone, D.; Pirri, C. F. A Study of the Effect of Electrode Composition on the Electrochemical Reduction of CO2. *Catalysis Today* **2021**. https://doi.org/10.1016/j.cattod.2021.07.014.

(89) Lourenço, M. A. O.; Zeng, J.; Jagdale, P.; Castellino, M.; Sacco, A.; Farkhondehfal, M. A.; Pirri, C. F. Biochar/Zinc Oxide Composites as Effective Catalysts for Electrochemical CO2 Reduction. *ACS Sustainable Chem. Eng.* **2021**, *9* (15), 5445–5453. https://doi.org/10.1021/acssuschemeng.1c00837.

(90) Xing, Z.; Hu, L.; Ripatti, D. S.; Hu, X.; Feng, X. Enhancing Carbon Dioxide Gas-Diffusion Electrolysis by Creating a Hydrophobic Catalyst Microenvironment. *Nat Commun* **2021**, *12* (1), 136. https://doi.org/10.1038/s41467-020-20397-5.

(91) Hosseini, S.; Savaloni, H.; Gholipour Shahraki, M. Influence of Surface Morphology and Nano-Structure on Hydrophobicity: A Molecular Dynamics Approach. *Applied Surface Science* **2019**, *485*, 536–546. https://doi.org/10.1016/j.apsusc.2019.04.236.

(92) Jiang, X.; Cai, F.; Gao, D.; Dong, J.; Miao, S.; Wang, G.; Bao, X. Electrocatalytic Reduction of Carbon Dioxide over Reduced Nanoporous Zinc Oxide. *Electrochemistry Communications* **2016**, *68*, 67–70. https://doi.org/10.1016/j.elecom.2016.05.003.

(93) Pérez-Rodríguez, S.; Pastor, E.; Lázaro, M. J. Electrochemical Behavior of the Carbon Black Vulcan XC-72R: Influence of the Surface Chemistry. *International Journal of Hydrogen Energy* **2018**, *43* (16), 7911–7922. https://doi.org/10.1016/j.ijhydene.2018.03.040.

(94) Dinh, C.-T.; Burdyny, T.; Kibria, M. G.; Seifitokaldani, A.; Gabardo, C. M.; García de Arquer, F. P.; Kiani, A.; Edwards, J. P.; De Luna, P.; Bushuyev, O. S.; Zou, C.; Quintero-Bermudez, R.; Pang, Y.; Sinton, D.; Sargent, E. H. CO2 Electroreduction to Ethylene via Hydroxide-Mediated Copper Catalysis at an Abrupt Interface. *Science* **2018**, *360* (6390), 783–787. https://doi.org/10.1126/science.aas9100.

(95) Ma, W.; Xie, S.; Liu, T.; Fan, Q.; Ye, J.; Sun, F.; Jiang, Z.; Zhang, Q.; Cheng, J.; Wang, Y. Electrocatalytic Reduction of CO2 to Ethylene and Ethanol through Hydrogen-Assisted C–C Coupling over Fluorine-Modified Copper. *Nat Catal* **2020**, *3* (6), 478–487. https://doi.org/10.1038/s41929-020-0450-0.

(96) Maikap, A.; Mukherjee, K.; Mondal, B.; Mandal, N. Zinc Oxide Thin Film Based Nonenzymatic Electrochemical Sensor for the Detection of Trace Level Catechol. *RSC Adv.* **2016**, *6* (69), 64611–64616. https://doi.org/10.1039/C6RA09598D.

(97) Fatin, S. O.; Lim, H. N.; Tan, W. T.; Huang, N. M. Comparison of Photocatalytic Activity and Cyclic Voltammetry of Zinc Oxide and Titanium Dioxide Nanoparticles toward Degradation of Methylene Blue. *Int. J. Electrochem. Sci.* **2012**, *7*, 11.

(98) Löffler, M.; Mayrhofer, K. J. J.; Katsounaros, I. Oxide Reduction Precedes Carbon Dioxide Reduction on Oxide-Derived Copper Electrodes. *J. Phys. Chem. C* **2021**, *125* (3), 1833–1838. https://doi.org/10.1021/acs.jpcc.0c09107.

(99) Stamatelos, I.; Dinh, C.-T.; Lehnert, W.; Shviro, M. Zn-Based Catalysts for Selective and Stable Electrochemical CO2 Reduction at High Current Densities. *ACS Appl. Energy Mater.* **2022**, *5* (11), 13928–13938. https://doi.org/10.1021/acsaem.2c02557.

(100) Zhang, T.; Li, X.; Qiu, Y.; Su, P.; Xu, W.; Zhong, H.; Zhang, H. Multilayered Zn Nanosheets as an Electrocatalyst for Efficient Electrochemical Reduction of CO2. *Journal of Catalysis* **2018**, *357*, 154–162. https://doi.org/10.1016/j.jcat.2017.11.003.

(101) Feng, X.; Jiang, K.; Fan, S.; Kanan, M. W. Grain-Boundary-Dependent CO2 Electroreduction Activity. *J. Am. Chem. Soc.* **2015**, *137* (14), 4606–4609. https://doi.org/10.1021/ja5130513.

(102) Albo, J.; Sáez, A.; Solla-Gullón, J.; Montiel, V.; Irabien, A. Production of Methanol from CO2 Electroreduction at Cu2O and Cu2O/ZnO-Based Electrodes in Aqueous Solution. *Applied Catalysis B: Environmental* **2015**, *176–177*, 709–717. https://doi.org/10.1016/j.apcatb.2015.04.055.

(103) Effect of 3d-Transition Metals Doped in ZnO Monolayers on the CO2 Electrochemical Reduction to Valuable Products: First Principles Study. *Applied Surface Science* **2021**, *550*, 149380. https://doi.org/10.1016/j.apsusc.2021.149380.

(104) Larrazábal, G. O.; Martín, A. J.; Mitchell, S.; Hauert, R.; Pérez-Ramírez, J. Synergistic Effects in Silver–Indium Electrocatalysts for Carbon Dioxide Reduction. *Journal of Catalysis* **2016**, *343*, 266–277. https://doi.org/10.1016/j.jcat.2015.12.014.

(105) Xie, H.; Chen, S.; Ma, F.; Liang, J.; Miao, Z.; Wang, T.; Wang, H.-L.; Huang, Y.; Li, Q. Boosting Tunable Syngas Formation via Electrochemical CO2 Reduction on Cu/In2O3 Core/Shell Nanoparticles. *ACS Appl. Mater. Interfaces* **2018**, *10* (43), 36996–37004. https://doi.org/10.1021/acsami.8b12747.

(106) Zhang, N.; Zhang, X.; Tao, L.; Jiang, P.; Ye, C.; Lin, R.; Huang, Z.; Li, A.; Pang, D.; Yan, H.; Wang, Y.; Xu, P.; An, S.; Zhang, Q.; Liu, L.; Du, S.; Han, X.; Wang, D.; Li, Y. Silver Single-Atom Catalyst for Efficient Electrochemical CO2 Reduction Synthesized from Thermal Transformation and Surface Reconstruction. *Angewandte Chemie International Edition* **2021**, *60* (11), 6170–6176. https://doi.org/10.1002/anie.202014718.

(107) Hongrutai, N.; Watmanee, S.; Pinthong, P.; Panpranot, J. Electrochemical Reduction of Carbon Dioxide on the Oxide-Containing Electrocatalysts. *Journal of CO2 Utilization* **2022**, *64*, 102194. https://doi.org/10.1016/j.jcou.2022.102194.

(108) Sikam, P.; Takahashi, K.; Roongcharoen, T.; Jitwatanasirikul, T.; Chitpakdee, C.; Faungnawakij, K.; Namuangruk, S. Effect of 3d-Transition Metals Doped in ZnO Monolayers on the CO2 Electrochemical Reduction to Valuable Products: First Principles Study. *Applied Surface Science* **2021**, *550*, 149380. https://doi.org/10.1016/j.apsusc.2021.149380.

(109) Wang, J.; Xiang, Q.; Zhang, W.; Shi, F.; Li, F.; Tao, P.; Song, C.; Shang, W.; Deng, T.; Wu, J. Effectively Tuning the Ratio of CO and H2 into Syngas through CO2 Electrochemical Reduction over a Wide Potential Range on a ZnO Nanosheet via Ni Doping. *ACS Appl. Energy Mater.* **2022**, *5* (5), 5531–5539. https://doi.org/10.1021/acsaem.1c03419.

(110) Pourbaix, M. *Atlas of Electrochemical Equilibria in Aqueous Solutions*; National Assoc. of Corrosion Engineers [u.a.]: Houston, Tex, 1974.

(111) Pinthong, P.; Klongklaew, P.; Praserthdam, P.; Panpranot, J. Effect of the Nanostructured Zn/Cu Electrocatalyst Morphology on the Electrochemical Reduction of CO2 to Value-Added Chemicals. *Nanomaterials (Basel)* **2021**, *11* (7), 1671. https://doi.org/10.3390/nano11071671.

(112) Velasco-Vélez, J.-J.; Jones, T.; Gao, D.; Carbonio, E.; Arrigo, R.; Hsu, C.-J.; Huang, Y.-C.; Dong, C.-L.; Chen, J.-M.; Lee, J.-F.; Strasser, P.; Roldan Cuenya, B.; Schlögl, R.; Knop-Gericke, A.; Chuang, C.-H. The Role of the Copper Oxidation State in the Electrocatalytic Reduction of CO2 into Valuable Hydrocarbons. *ACS Sustainable Chem. Eng.* **2019**, *7* (1), 1485–1492. https://doi.org/10.1021/acssuschemeng.8b05106.

(113) Chou, T.-C.; Chang, C.-C.; Yu, H.-L.; Yu, W.-Y.; Dong, C.-L.; Velasco-Vélez, J.-J.; Chuang, C.-H.; Chen, L.-C.; Lee, J.-F.; Chen, J.-M.; Wu, H.-L. Controlling the Oxidation State of the Cu Electrode and Reaction Intermediates for Electrochemical CO2 Reduction to Ethylene. *J. Am. Chem. Soc.* **2020**, *142* (6), 2857–2867. https://doi.org/10.1021/jacs.9b11126.

(114) Ma, Z.; Luo, C.; Wang, C.; Liu, J. Study of Optical Properties of ZnO Doped with Fe. *Optik* **2019**, *188*, 104–109. https://doi.org/10.1016/j.ijleo.2019.05.032.

(115) Russo, V.; Ghidelli, M.; Gondoni, P.; Casari, C. S.; Li Bassi, A. Multi-Wavelength Raman Scattering of Nanostructured Al-Doped Zinc Oxide. *Journal of Applied Physics* **2014**, *115* (7), 073508. https://doi.org/10.1063/1.4866322.

(116) Hsieh, P.-T.; Chen, Y.-C.; Kao, K.-S.; Wang, C.-M. Luminescence Mechanism of ZnO Thin Film Investigated by XPS Measurement. *Appl. Phys. A* **2008**, *90* (2), 317–321. https://doi.org/10.1007/s00339-007-4275-3.

(117) Abdel-wahab, M. Sh.; Jilani, A.; Yahia, I. S.; Al-Ghamdi, A. A. Enhanced the Photocatalytic Activity of Ni-Doped ZnO Thin Films: Morphological, Optical and XPS Analysis. *Superlattices and Microstructures* **2016**, *94*, 108–118. https://doi.org/10.1016/j.spmi.2016.03.043.

(118) Li, Z.; Chen, H.; Liu, W. Full-Spectrum Photocatalytic Activity of ZnO/CuO/ZnFe2O4 Nanocomposite as a PhotoFenton-Like Catalyst. *Catalysts* **2018**, *8* (11), 557. https://doi.org/10.3390/catal8110557.

(119) Hu, J.; Li, Y.; Zhen, Y.; Chen, M.; Wan, H. In Situ FTIR and Ex Situ XPS/HS-LEIS Study of Supported Cu/Al2O3 and Cu/ZnO Catalysts for CO2 Hydrogenation. *Chinese Journal of Catalysis* **2021**, *42* (3), 367–375. https://doi.org/10.1016/S1872-2067(20)63672-5.

(120) Li, M.; Xu, J.; Chen, X.; Zhang, X.; Wu, Y.; Li, P.; Niu, X.; Luo, C.; Li, L. Structural and Optical Properties of Cobalt Doped ZnO Nanocrystals. *Superlattices and Microstructures* **2012**, *52* (4), 824–833. https://doi.org/10.1016/j.spmi.2012.07.014.

(121) Lommens, P.; Smet, P. F.; de Mello Donega, C.; Meijerink, A.; Piraux, L.; Michotte, S.; Mátéfi-Tempfli, S.; Poelman, D.; Hens, Z. Photoluminescence Properties of Co2+-Doped ZnO Nanocrystals. *Journal of Luminescence* **2006**, *118* (2), 245–250. https://doi.org/10.1016/j.jlumin.2005.08.020.

(122) Liu, X.; Cheng, W.; Ma, X.; Shi, W. [Fluorescence emission properties of Ni-doped ZnO films]. *Guang Pu Xue Yu Guang Pu Fen Xi* **2006**, *26* (11), 2069–2071.

(123) Wan, L.; Zhang, X.; Cheng, J.; Chen, R.; Wu, L.; Shi, J.; Luo, J. Bimetallic Cu–Zn Catalysts for Electrochemical CO2 Reduction: Phase-Separated versus Core–Shell Distribution. *ACS Catal.* **2022**, *12* (5), 2741–2748. https://doi.org/10.1021/acscatal.1c05272.

(124) Lamaison, S.; Wakerley, D.; Kracke, F.; Moore, T.; Zhou, L.; Lee, D. U.; Wang, L.; Hubert, M. A.; Aviles Acosta, J. E.; Gregoire, J. M.; Duoss, E. B.; Baker, S.; Beck, V. A.; Spormann, A. M.; Fontecave, M.; Hahn, C.; Jaramillo, T. F. Designing a Zn–Ag Catalyst Matrix and Electrolyzer System for CO2 Conversion to CO and Beyond. *Advanced Materials* **2022**, *34* (1), 2103963. https://doi.org/10.1002/adma.202103963.

(125) Zhang, Z.; Wen, G.; Luo, D.; Ren, B.; Zhu, Y.; Gao, R.; Dou, H.; Sun, G.; Feng, M.; Bai, Z.; Yu, A.; Chen, Z. “Two Ships in a Bottle” Design for Zn–Ag–O Catalyst Enabling Selective and Long-Lasting CO2 Electroreduction. *J. Am. Chem. Soc.* **2021**. https://doi.org/10.1021/jacs.0c12418.

(126) Ren, B.; Zhang, Z.; Wen, G.; Zhang, X.; Xu, M.; Weng, Y.; Nie, Y.; Dou, H.; Jiang, Y.; Deng, Y.-P.; Sun, G.; Luo, D.; Shui, L.; Wang, X.; Feng, M.; Yu, A.; Chen, Z. Dual-Scale Integration Design of Sn–ZnO Catalyst toward Efficient and Stable CO2 Electroreduction. *Advanced Materials* **2022**, *34* (38), 2204637. https://doi.org/10.1002/adma.202204637.

(127) Bhalothia, D.; Lee, D.-W.; Jhao, G.-P.; Liu, H.-Y.; Jia, Y.; Dai, S.; Wang, K.-W.; Chen, T.-Y. Reaction Pathways for the Highly Selective and Durable Electrochemical CO2 to CO Conversion on ZnO Supported Ag Nanoparticles in KCl Electrolyte. *Applied Surface Science* **2023**, *608*, 155224. https://doi.org/10.1016/j.apsusc.2022.155224.

(128) Nguyen, V.-H.; Thi Vo, T.-T.; Huu Do, H.; Thuan Le, V.; Nguyen, T. D.; Ky Vo, T.; Nguyen, B.-S.; Nguyen, T. T.; Phung, T. K.; Tran, V. A. Ag@ZnO Porous Nanoparticle Wrapped by rGO for the Effective CO2 Electrochemical Reduction. *Chemical Engineering Science* **2021**, *232*, 116381. https://doi.org/10.1016/j.ces.2020.116381.

(129) Gao, D.; Zhang, Y.; Zhou, Z.; Cai, F.; Zhao, X.; Huang, W.; Li, Y.; Zhu, J.; Liu, P.; Yang, F.; Wang, G.; Bao, X. Enhancing CO2 Electroreduction with the Metal–Oxide Interface. *J. Am. Chem. Soc.* **2017**, *139* (16), 5652–5655. https://doi.org/10.1021/jacs.7b00102.

(130) Stamatelos, I.; da Silva, G. T. S. T.; Ribeiro, C.; Shviro, M. Exploring Heterostructures of D-Block Metal Oxides Coupled to ZnO for the Electrochemical Reduction of CO2. *ACS Appl. Energy Mater.* **2023**, *6* (22), 11510–11520. https://doi.org/10.1021/acsaem.3c01791.

(131) Ning, S.; Guo, Z.; Wang, J.; Huang, S.; Chen, S.; Kang, X. Sn-Doped CeO2 Nanorods as High-Performance Electrocatalysts for CO2 Reduction to Formate. *ChemElectroChem* **2021**, *8* (14), 2680–2685. https://doi.org/10.1002/celc.202100445.

(132) Kou, T.; Wang, S.; Yang, S.; Ren, Q.; Ball, R.; Rao, D.; Chiovoloni, S.; Lu, J. Q.; Zhang, Z.; Duoss, E. B.; Li, Y. Amorphous CeO2–Cu Heterostructure Enhances CO2 Electroreduction to Multicarbon Alcohols. *ACS Materials Lett.* **2022**, *4* (10), 1999–2008. https://doi.org/10.1021/acsmaterialslett.2c00506.

(133) Li, Z.; Deng, Z.; Ouyang, L.; Fan, X.; Zhang, L.; Sun, S.; Liu, Q.; Alshehri, A. A.; Luo, Y.; Kong, Q.; Sun, X. CeO2 Nanoparticles with Oxygen Vacancies Decorated N-Doped Carbon Nanorods: A Highly Efficient Catalyst for Nitrate Electroreduction to Ammonia. *Nano Res.* **2022**, *15* (10), 8914–8921. https://doi.org/10.1007/s12274-022-4863-8.

(134) Ren, X.; Gao, Y.; Zheng, L.; Wang, Z.; Wang, P.; Zheng, Z.; Liu, Y.; Cheng, H.; Dai, Y.; Huang, B. Oxygen Vacancy Enhancing CO2 Electrochemical Reduction to CO on Ce-Doped ZnO Catalysts. *Surfaces and Interfaces* **2021**, *23*, 100923. https://doi.org/10.1016/j.surfin.2020.100923.

(135) Shah, S. S. A.; Najam, T.; Wen, M.; Zang, S.-Q.; Waseem, A.; Jiang, H.-L. Metal–Organic Framework-Based Electrocatalysts for CO2 Reduction. *Small Structures* **2022**, *3* (5), 2100090. https://doi.org/10.1002/sstr.202100090.

(136) Liu, M.; Pang, Y.; Zhang, B.; De Luna, P.; Voznyy, O.; Xu, J.; Zheng, X.; Dinh, C. T.; Fan, F.; Cao, C.; de Arquer, F. P. G.; Safaei, T. S.; Mepham, A.; Klinkova, A.; Kumacheva, E.; Filleter, T.; Sinton, D.; Kelley, S. O.; Sargent, E. H. Enhanced Electrocatalytic CO2 Reduction via Field-Induced Reagent Concentration. *Nature* **2016**, *537* (7620), 382–386. https://doi.org/10.1038/nature19060.

(137) Yin, J.; Gao, Z.; Wei, F.; Liu, C.; Gong, J.; Li, J.; Li, W.; Xiao, L.; Wang, G.; Lu, J.; Zhuang, L. Customizable CO2 Electroreduction to C1 or C2+ Products through Cuy/CeO2 Interface Engineering. *ACS Catal.* **2022**, *12* (2), 1004–1011. https://doi.org/10.1021/acscatal.1c04714.

(138) Fu, H. Q.; Liu, J.; Bedford, N. M.; Wang, Y.; Sun, J. W.; Zou, Y.; Dong, M.; Wright, J.; Diao, H.; Liu, P.; Yang, H. G.; Zhao, H. Synergistic Cr2O3@Ag Heterostructure Enhanced Electrocatalytic CO2 Reduction to CO. *Advanced Materials* **2022**, *34* (29), 2202854. https://doi.org/10.1002/adma.202202854.

(139) Rodwihok, C.; Wongratanaphisan, D.; Tam, T. V.; Choi, W. M.; Hur, S. H.; Chung, J. S. Cerium-Oxide-Nanoparticle-Decorated Zinc Oxide with Enhanced Photocatalytic Degradation of Methyl Orange. *Applied Sciences* **2020**, *10* (5), 1697. https://doi.org/10.3390/app10051697.

(140) Rajendran, S.; Khan, M. M.; Gracia, F.; Qin, J.; Gupta, V. K.; Arumainathan, S. Ce3+-Ion-Induced Visible-Light Photocatalytic Degradation and Electrochemical Activity of ZnO/CeO2 Nanocomposite. *Sci Rep* **2016**, *6* (1), 31641. https://doi.org/10.1038/srep31641.

(141) Sun, K.; Zhan, G.; Chen, H.; Lin, S. Low-Operating-Temperature NO2 Sensor Based on a CeO2/ZnO Heterojunction. *Sensors* **2021**, *21* (24), 8269. https://doi.org/10.3390/s21248269.

(142) Rehman, S.; Kim, H.; Farooq Khan, M.; Hur, J.-H.; Lee, A. D.; Kim, D. Tuning of Ionic Mobility to Improve the Resistive Switching Behavior of Zn-Doped CeO2. *Sci Rep* **2019**, *9* (1), 19387. https://doi.org/10.1038/s41598-019-55716-4.

(143) Hong, S.; Abbas, H. G.; Jang, K.; Patra, K. K.; Kim, B.; Choi, B.-U.; Song, H.; Lee, K.-S.; Choi, P.-P.; Ringe, S.; Oh, J. Tuning the C1/C2 Selectivity of Electrochemical CO2 Reduction on Cu-CeO2 Nanorods by Oxidation State Control. *Advanced Materials n/a* (n/a), 2208996. https://doi.org/10.1002/adma.202208996.

(144) Yang, T.; Lin, L.; Lv, X.; Yang, H.; Feng, H.; Huang, Z.; Li, J.; Pao, C.-W.; Hu, Z.; Zhan, C.; Xu, Y.; Zheng, L.-S.; Jiao, F.; Huang, X. Interfacial Synergy between the Cu Atomic Layer and CeO2 Promotes CO Electrocoupling to Acetate. *ACS Nano* **2023**. https://doi.org/10.1021/acsnano.3c00817.

(145) Zong, X.; Jin, Y.; Zhang, X.; Zhang, J.; Li, X.; Xiong, Y. Stabilization of Oxidation State in ZnO Decorated-CeO2 for Enhanced Formation of CO in CO2 Electroreduction. *Applied Surface Science* **2023**, *609*, 155235. https://doi.org/10.1016/j.apsusc.2022.155235.

(146) Stamatelos, I.; Scheepers, F.; Pasel, J.; Dinh, C.-T.; Stolten, D. Ternary Zn-Ce-Ag Catalysts for Selective and Stable Electrochemical CO2 Reduction at Large-Scale. *Applied Catalysis B: Environment and Energy* **2024**, 124062. https://doi.org/10.1016/j.apcatb.2024.124062.

(147) Park, S. J.; Joo, M. H.; Yang, J. H.; Hong, S.-M.; Rhee, C. K.; Kang, J.-G.; Sohn, Y. Electrochemical Ce(III)/Ce(IV) Redox Behavior and Ce Oxide Nanostructure Recovery over Thio-Terpyridine-Functionalized Au/Carbon Paper Electrodes. *ACS Appl. Mater. Interfaces* **2021**, *13* (23), 27594–27611. https://doi.org/10.1021/acsami.1c05105.

(148) Fang, L.; Lyu, X.; Xu, J. J.; Liu, Y.; Hu, X.; Reinhart, B. J.; Li, T. Operando X-Ray Absorption Spectroscopy Study of SnO2 Nanoparticles for Electrochemical Reduction of CO2 to Formate. *ACS Appl. Mater. Interfaces* **2022**, *14* (50), 55636–55643. https://doi.org/10.1021/acsami.2c17481.

(149) Ge, L.; Rabiee, H.; Li, M.; Subramanian, S.; Zheng, Y.; Lee, J. H.; Burdyny, T.; Wang, H. Electrochemical CO2 Reduction in Membrane-Electrode Assemblies. *Chem* **2022**, *8* (3), 663–692. https://doi.org/10.1016/j.chempr.2021.12.002.

(150) Zhao, X.; Du, L.; You, B.; Sun, Y. Integrated Design for Electrocatalytic Carbon Dioxide Reduction. *Catal. Sci. Technol.* **2020**, *10* (9), 2711–2720. https://doi.org/10.1039/D0CY00453G.

(151) Vass, Á.; Kormányos, A.; Kószó, Z.; Endrődi, B.; Janáky, C. Anode Catalysts in CO2 Electrolysis: Challenges and Untapped Opportunities. *ACS Catal.* **2022**, *12* (2), 1037–1051. https://doi.org/10.1021/acscatal.1c04978.

(152) Pedeferri (Deceased), P. Pourbaix Diagrams. In *Corrosion Science and Engineering*; Pedeferri, P., Ed.; Engineering Materials; Springer International Publishing: Cham, 2018; pp 57–72. https://doi.org/10.1007/978-3-319-97625-9_4.

(153) Mot, B. D.; Ramdin, M.; Hereijgers, J.; Vlugt, T. J. H.; Breugelmans, T. Direct Water Injection in Catholyte-Free Zero-Gap Carbon Dioxide Electrolyzers. *ChemElectroChem* **2020**, *7* (18), 3839–3843. https://doi.org/10.1002/celc.202000961.

(154) Jung, B.; Park, S.; Lim, C.; Lee, W. H.; Lim, Y.; Na, J.; Lee, C.-J.; Oh, H.-S.; Lee, U. Design Methodology for Mass Transfer-Enhanced Large-Scale Electrochemical Reactor for CO2 Reduction. *Chemical Engineering Journal* **2021**, *424*, 130265. https://doi.org/10.1016/j.cej.2021.130265.

(155) Larrazábal, G. O.; Strøm-Hansen, P.; Heli, J. P.; Zeiter, K.; Therkildsen, K. T.; Chorkendorff, I.; Seger, B. Analysis of Mass Flows and Membrane Cross-over in CO2 Reduction at High Current Densities in an MEA-Type Electrolyzer. *ACS Appl. Mater. Interfaces* **2019**, *11* (44), 41281–41288. https://doi.org/10.1021/acsami.9b13081.

(156) Weng, L.-C.; Bell, A. T.; Weber, A. Z. Modeling Gas-Diffusion Electrodes for CO2 Reduction. *Phys. Chem. Chem. Phys.* **2018**, *20* (25), 16973–16984. https://doi.org/10.1039/C8CP01319E.

(157) Wang, Q.; Wang, X.; Wu, C.; Cheng, Y.; Sun, Q.; Dong, H.; Yu, H. Electrodeposition of Tin on Nafion-Bonded Carbon Black as an Active Catalyst Layer for Efficient Electroreduction of CO2 to Formic Acid. *Sci Rep* **2017**, *7* (1), 13711. https://doi.org/10.1038/s41598-017-14233-y.

(158) Xing, Z.; Hu, L.; Ripatti, D. S.; Hu, X.; Feng, X. Enhancing Carbon Dioxide Gas-Diffusion Electrolysis by Creating a Hydrophobic Catalyst Microenvironment. *Nat Commun* **2021**, *12* (1), 136. https://doi.org/10.1038/s41467-020-20397-5.

(159) Kim, B.; Hillman, F.; Ariyoshi, M.; Fujikawa, S.; Kenis, P. J. A. Effects of Composition of the Micro Porous Layer and the Substrate on Performance in the Electrochemical

Reduction of CO2 to CO. *Journal of Power Sources* **2016**, *312*, 192–198. https://doi.org/10.1016/j.jpowsour.2016.02.043.
(160) Samu, A. A.; Szenti, I.; Kukovecz, Á.; Endrődi, B.; Janáky, C. Systematic Screening of Gas Diffusion Layers for High Performance CO2 Electrolysis. *Commun Chem* **2023**, *6* (1), 1–9. https://doi.org/10.1038/s42004-023-00836-2.
(161) Weekes, D. M.; Salvatore, D. A.; Reyes, A.; Huang, A.; Berlinguette, C. P. Electrolytic CO2 Reduction in a Flow Cell. *Acc. Chem. Res.* **2018**, *51* (4), 910–918. https://doi.org/10.1021/acs.accounts.8b00010.
(162) Xie, K.; Miao, R. K.; Ozden, A.; Liu, S.; Chen, Z.; Dinh, C.-T.; Huang, J. E.; Xu, Q.; Gabardo, C. M.; Lee, G.; Edwards, J. P.; O'Brien, C. P.; Boettcher, S. W.; Sinton, D.; Sargent, E. H. Bipolar Membrane Electrolyzers Enable High Single-Pass CO2 Electroreduction to Multicarbon Products. *Nat Commun* **2022**, *13* (1), 3609. https://doi.org/10.1038/s41467-022-31295-3.
(163) Weng, L.-C.; Bell, A. T.; Weber, A. Z. Towards Membrane-Electrode Assembly Systems for CO2 Reduction: A Modeling Study. *Energy Environ. Sci.* **2019**, *12* (6), 1950–1968. https://doi.org/10.1039/C9EE00909D.
(164) Salvatore, D. A.; Gabardo, C. M.; Reyes, A.; O'Brien, C. P.; Holdcroft, S.; Pintauro, P.; Bahar, B.; Hickner, M.; Bae, C.; Sinton, D.; Sargent, E. H.; Berlinguette, C. P. Designing Anion Exchange Membranes for CO2 Electrolysers. *Nat Energy* **2021**, *6* (4), 339–348. https://doi.org/10.1038/s41560-020-00761-x.
(165) Kutz, R. B.; Chen, Q.; Yang, H.; Sajjad, S. D.; Liu, Z.; Masel, I. R. Sustainion Imidazolium-Functionalized Polymers for Carbon Dioxide Electrolysis. *Energy Technology* **2017**, *5* (6), 929–936. https://doi.org/10.1002/ente.201600636.
(166) Li, J.; Ozden, A.; Wan, M.; Hu, Y.; Li, F.; Wang, Y.; Zamani, R. R.; Ren, D.; Wang, Z.; Xu, Y.; Nam, D.-H.; Wicks, J.; Chen, B.; Wang, X.; Luo, M.; Graetzel, M.; Che, F.; Sargent, E. H.; Sinton, D. Silica-Copper Catalyst Interfaces Enable Carbon-Carbon Coupling towards Ethylene Electrosynthesis. *Nat Commun* **2021**, *12* (1), 2808. https://doi.org/10.1038/s41467-021-23023-0.
(167) Garg, S.; Rodriguez, C. A. G.; Rufford, T. E.; Varcoe, J. R.; Seger, B. How Membrane Characteristics Influence the Performance of CO2 and CO Electrolysis. *Energy Environ. Sci.* **2022**, *15* (11), 4440–4469. https://doi.org/10.1039/D2EE01818G.
(168) Fabbri, E.; Schmidt, T. J. Oxygen Evolution Reaction—The Enigma in Water Electrolysis. *ACS Catal.* **2018**, *8* (10), 9765–9774. https://doi.org/10.1021/acscatal.8b02712.
(169) Zhou, L. Q.; Ling, C.; Zhou, H.; Wang, X.; Liao, J.; Reddy, G. K.; Deng, L.; Peck, T. C.; Zhang, R.; Whittingham, M. S.; Wang, C.; Chu, C.-W.; Yao, Y.; Jia, H. A High-Performance Oxygen Evolution Catalyst in Neutral-pH for Sunlight-Driven CO2 Reduction. *Nat Commun* **2019**, *10* (1), 4081. https://doi.org/10.1038/s41467-019-12009-8.
(170) Abbott, D. F.; Lebedev, D.; Waltar, K.; Povia, M.; Nachtegaal, M.; Fabbri, E.; Copéret, C.; Schmidt, T. J. Iridium Oxide for the Oxygen Evolution Reaction: Correlation between Particle Size, Morphology, and the Surface Hydroxo Layer from Operando XAS. *Chem. Mater.* **2016**, *28* (18), 6591–6604. https://doi.org/10.1021/acs.chemmater.6b02625.
(171) *Handbook of Fuel Cells: Fundamentals, Technology, Applications, 4 Volume Set | Wiley*. Wiley.com. https://www.wiley.com/en-us/Handbook+of+Fuel+Cells%3A+Fundamentals%2C+Technology%2C+Applications%2C+4+Volume+Set-p-9780471499268 (accessed 2023-08-12).
(172) Li, C. W.; Kanan, M. W. CO2 Reduction at Low Overpotential on Cu Electrodes Resulting from the Reduction of Thick Cu2O Films. *J. Am. Chem. Soc.* **2012**, *134* (17), 7231–7234. https://doi.org/10.1021/ja3010978.

(173) Whipple, D. T.; Finke, E. C.; Kenis, P. J. A. Microfluidic Reactor for the Electrochemical Reduction of Carbon Dioxide: The Effect of pH. *Electrochem. Solid-State Lett.* **2010**, *13* (9), B109. https://doi.org/10.1149/1.3456590.

(174) Ghorbani, H. R.; Mehr, F. P.; Pazoki, H.; Rahmani, B. M. Synthesis of ZnO Nanoparticles by Precipitation Method. *Oriental Journal of Chemistry* **2015**, *31* (2), 1219–1221.

(175) Li, J.; Fan, H.; Jia, X. Multilayered ZnO Nanosheets with 3D Porous Architectures: Synthesis and Gas Sensing Application. *J. Phys. Chem. C* **2010**, *114* (35), 14684–14691. https://doi.org/10.1021/jp100792c.

(176) Zhang, J.; Wang, W.; Zhu, P.; Chen, J.; Zhang, Z.; Wu, Z. Synthesis of Small Diameter ZnO Nanorods via Refluxing Route in Alcohol–Water Mixing Solution Containing Zinc Salt and Urea. *Materials Letters* **2007**, *61* (2), 592–594. https://doi.org/10.1016/j.matlet.2006.05.018.

(177) Liang, Y.; Wu, C.; Meng, S.; Lu, Z.; Zhao, R.; Wang, H.; Liu, Z.; Wang, J. Ag Single Atoms Anchored on CeO2 with Interfacial Oxygen Vacancies for Efficient CO2 Electroreduction. *ACS Appl. Mater. Interfaces* **2023**, *15* (25), 30262–30271. https://doi.org/10.1021/acsami.3c04556.

(178) Lavrynenko, O. M.; Zahornyi, M. M.; Vember, V. V.; Pavlenko, O. Y.; Lobunets, T. F.; Kolomys, O. F.; Povnitsa, O. Y.; Artiukh, L. O.; Naumenko, K. S.; Zahorodnia, S. D.; Garmasheva, I. L. Nanocomposites Based on Cerium, Lanthanum, and Titanium Oxides Doped with Silver for Biomedical Application. *Condensed Matter* **2022**, *7* (3), 45. https://doi.org/10.3390/condmat7030045.

(179) Aranda, A.; Landers, R.; Carnelli, P.; Candal, R.; Alarcón, H.; Rodríguez, J. Influence of Silver Electrochemically Deposited onto Zinc Oxide Seed Nanoparticles on the Photoelectrochemical Performance of Zinc Oxide Nanorod Films. *Nanomaterials and Nanotechnology* **2019**, *9*, 1847980419844363. https://doi.org/10.1177/1847980419844363.

(180) Liu, F.-C.; Li, J.-Y.; Chen, T.-H.; Chang, C.-H.; Lee, C.-T.; Hsiao, W.-H.; Liu, D.-S. Effect of Silver Dopants on the ZnO Thin Films Prepared by a Radio Frequency Magnetron Co-Sputtering System. *Materials* **2017**, *10* (7), 797. https://doi.org/10.3390/ma10070797.

(181) Shan, G.; Xu, L.; Wang, G.; Liu, Y. Enhanced Raman Scattering of ZnO Quantum Dots on Silver Colloids. *J. Phys. Chem. C* **2007**, *111* (8), 3290–3293. https://doi.org/10.1021/jp066070v.

(182) Zamiri, R.; Rebelo, A.; Zamiri, G.; Adnani, A.; Kuashal, A.; Belsley, M. S.; Ferreira, J. M. F. Far-Infrared Optical Constants of ZnO and ZnO/Ag Nanostructures. *RSC Adv.* **2014**, *4* (40), 20902–20908. https://doi.org/10.1039/C4RA01563K.

(183) 高敦峰魏鹏飞; Dunfeng Gao, P. W. 用于二氧化碳电催化还原的电解器研究进展. 物理化学学报 **2020**, *37* (5), 2009021. https://doi.org/10.3866/PKU.WHXB202009021.

(184) Karimi, P.; Alihosseinzadeh, A.; Ponnurangam, S.; Karan, K. Performance Characteristics of Polymer Electrolyte Membrane CO2 Electrolyzer: Effect of CO2 Dilution, Flow Rate and Pressure. *J. Electrochem. Soc.* **2022**, *169* (6), 064510. https://doi.org/10.1149/1945-7111/ac725f.

(185) Vliet, D. van der; Strmcnik, D. S.; Wang, C.; Stamenkovic, V. R.; Markovic, N. M.; Koper, M. T. M. On the Importance of Correcting for the Uncompensated Ohmic Resistance in Model Experiments of the Oxygen Reduction Reaction. *Journal of Electroanalytical Chemistry* **2010**, *647* (1), 29.

(186) Dinh, C.-T.; Burdyny, T.; Kibria, M. G.; Seifitokaldani, A.; Gabardo, C. M.; García de Arquer, F. P.; Kiani, A.; Edwards, J. P.; De Luna, P.; Bushuyev, O. S.; Zou, C.; Quintero-Bermudez, R.; Pang, Y.; Sinton, D.; Sargent, E. H. CO2 Electroreduction to Ethylene via Hydroxide-Mediated Copper Catalysis at an Abrupt Interface. *Science* **2018**, *360* (6390), 783–787. https://doi.org/10.1126/science.aas9100.

(187) Fujinuma, N.; Ikoma, A.; Lofland, S. E. Highly Efficient Electrochemical CO2 Reduction Reaction to CO with One-Pot Synthesized Co-Pyridine-Derived Catalyst Incorporated in a Nafion-Based Membrane Electrode Assembly. *Advanced Energy Materials* **2020**, *10* (39), 2001645. https://doi.org/10.1002/aenm.202001645.

(188) Hjorth, I.; Nord, M.; Rønning, M.; Yang, J.; Chen, D. Electrochemical Reduction of CO2 to Synthesis Gas on CNT Supported CuxZn1-x O Catalysts. *Catalysis Today* **2020**, *357*, 311–321. https://doi.org/10.1016/j.cattod.2019.02.045.

(189) Löffler, M.; Mayrhofer, K. J. J.; Katsounaros, I. Oxide Reduction Precedes Carbon Dioxide Reduction on Oxide-Derived Copper Electrodes. *J. Phys. Chem. C* **2021**, *125* (3), 1833–1838. https://doi.org/10.1021/acs.jpcc.0c09107.

(190) Jeon, S. S.; Kang, P. W.; Klingenhof, M.; Lee, H.; Dionigi, F.; Strasser, P. Active Surface Area and Intrinsic Catalytic Oxygen Evolution Reactivity of NiFe LDH at Reactive Electrode Potentials Using Capacitances. *ACS Catal.* **2023**, *13* (2), 1186–1196. https://doi.org/10.1021/acscatal.2c04452.

(191) Connor, P.; Schuch, J.; Kaiser, B.; Jaegermann, W. The Determination of Electrochemical Active Surface Area and Specific Capacity Revisited for the System MnOx as an Oxygen Evolution Catalyst. *Zeitschrift für Physikalische Chemie* **2020**, *234* (5), 979–994. https://doi.org/10.1515/zpch-2019-1514.

(192) Yang, F. Size Effect on Electric-Double-Layer Capacitances of Conducting Structures. *Physics Letters A* **2019**, *383* (20), 2353–2360. https://doi.org/10.1016/j.physleta.2019.04.051.

(193) Watkins, N. B.; Schiffer, Z. J.; Lai, Y.; Musgrave, C. B. I.; Atwater, H. A.; Goddard, W. A. I.; Agapie, T.; Peters, J. C.; Gregoire, J. M. Hydrodynamics Change Tafel Slopes in Electrochemical CO2 Reduction on Copper. *ACS Energy Lett.* **2023**, *8* (5), 2185–2192. https://doi.org/10.1021/acsenergylett.3c00442.

(194) Shinagawa, T.; Garcia-Esparza, A. T.; Takanabe, K. Insight on Tafel Slopes from a Microkinetic Analysis of Aqueous Electrocatalysis for Energy Conversion. *Sci Rep* **2015**, *5* (1), 13801. https://doi.org/10.1038/srep13801.

(195) Yoshimitsu, Z.; Nakajima, A.; Watanabe, T.; Hashimoto, K. Effects of Surface Structure on the Hydrophobicity and Sliding Behavior of Water Droplets. *Langmuir* **2002**, *18* (15), 5818–5822. https://doi.org/10.1021/la020088p.

(196) Liu, Y.; Liu, H.; Zhang, Q.; Li, T. Adjusting the Proportions of {0001} Facets and High-Index Facets of ZnO Hexagonal Prisms and Their Photocatalytic Activity. *RSC Adv.* **2017**, *7* (6), 3515–3520. https://doi.org/10.1039/C6RA24912D.

(197) Li, P.; Liu, J.; Bi, J.; Zhu, Q.; Wu, T.; Ma, J.; Zhang, F.; Jia, J.; Han, B. Tuning the Efficiency and Product Composition for Electrocatalytic CO2 Reduction to Syngas over Zinc Films by Morphology and Wettability. *Green Chem.* **2022**. https://doi.org/10.1039/D1GC04364A.

(198) Zhang, T.; Zhong, H.; Qiu, Y.; Li, X.; Zhang, H. Zn Electrode with a Layer of Nanoparticles for Selective Electroreduction of CO2 to Formate in Aqueous Solutions. *J. Mater. Chem. A* **2016**, *4* (42), 16670–16676. https://doi.org/10.1039/C6TA07000K.

(199) Zhang, J.; Yin, R.; Shao, Q.; Zhu, T.; Huang, X. Oxygen Vacancies in Amorphous InOx Nanoribbons Enhance CO2 Adsorption and Activation for CO2 Electroreduction. *Angewandte Chemie International Edition* **2019**, *58* (17), 5609–5613. https://doi.org/10.1002/anie.201900167.

(200) Nguyen, D. L. T.; Jee, M. S.; Won, D. H.; Jung, H.; Oh, H.-S.; Min, B. K.; Hwang, Y. J. Selective CO2 Reduction on Zinc Electrocatalyst: The Effect of Zinc Oxidation State Induced by Pretreatment Environment. *ACS Sustainable Chem. Eng.* **2017**, *5* (12), 11377–11386. https://doi.org/10.1021/acssuschemeng.7b02460.

(201) Zhang, L.; Li, H.; Yang, B.; Zhou, Y.; Zhang, Z.; Wang, Y. Photo-Deposition of ZnO/Co3O4 Core-Shell Nanorods with p-n Junction for Efficient Oxygen Evolution

Reaction. *J Solid State Electrochem* **2019**, *23* (12), 3287–3297. https://doi.org/10.1007/s10008-019-04444-w.

(202) Russo, V.; Ghidelli, M.; Gondoni, P.; Casari, C. S.; Li Bassi, A. Multi-Wavelength Raman Scattering of Nanostructured Al-Doped Zinc Oxide. *Journal of Applied Physics* **2014**, *115* (7), 073508. https://doi.org/10.1063/1.4866322.

(203) Chanda, A.; Gupta, S.; Vasundhara, M.; Joshi, S. R.; Mutta, G. R.; Singh, J. Study of Structural, Optical and Magnetic Properties of Cobalt Doped ZnO Nanorods. *RSC Adv.* **2017**, *7* (80), 50527–50536. https://doi.org/10.1039/C7RA08458G.

(204) Swadźba-Kwaśny, M.; Chancelier, L.; Ng, S.; Manyar, H. G.; Hardacre, C.; Nockemann, P. Facile in Situ Synthesis of Nanofluids Based on Ionic Liquids and Copper Oxide Clusters and Nanoparticles. *Dalton Trans.* **2011**, *41* (1), 219–227. https://doi.org/10.1039/C1DT11578B.

(205) Chai, C.; Liu, H.; Yu, W. The Electronic and Optical Properties of the Fe,Co,Ni and Cu Doped ZnO Monolayer Photocatalyst. *Chemical Physics Letters* **2021**, *778*, 138765. https://doi.org/10.1016/j.cplett.2021.138765.

(206) Qi, S.-C.; Liu, X.-Y.; Zhu, R.-R.; Xue, D.-M.; Liu, X.-Q.; Sun, L.-B. Causation of Catalytic Activity of Cu-ZnO for CO2 Hydrogenation to Methanol. *Chemical Engineering Journal* **2022**, *430*, 132784. https://doi.org/10.1016/j.cej.2021.132784.

(207) Permyakova, A. A.; Herranz, J.; El Kazzi, M.; Diercks, J. S.; Povia, M.; Mangani, L. R.; Horisberger, M.; Pătru, A.; Schmidt, T. J. On the Oxidation State of Cu2O upon Electrochemical CO2 Reduction: An XPS Study. *ChemPhysChem* **2019**, *20* (22), 3120–3127. https://doi.org/10.1002/cphc.201900468.

(208) Zhang, T.; Wu, M.-Y.; Yan, D.-Y.; Mao, J.; Liu, H.; Hu, W.-B.; Du, X.-W.; Ling, T.; Qiao, S.-Z. Engineering Oxygen Vacancy on NiO Nanorod Arrays for Alkaline Hydrogen Evolution. *Nano Energy* **2018**, *43*, 103–109. https://doi.org/10.1016/j.nanoen.2017.11.015.

(209) Faid, A. Y.; Barnett, A. O.; Seland, F.; Sunde, S. Ni/NiO Nanosheets for Alkaline Hydrogen Evolution Reaction: In Situ Electrochemical-Raman Study. *Electrochimica Acta* **2020**, *361*, 137040. https://doi.org/10.1016/j.electacta.2020.137040.

(210) Hall, D. S.; Lockwood, D. J.; Bock, C.; MacDougall, B. R. Nickel Hydroxides and Related Materials: A Review of Their Structures, Synthesis and Properties. *Proceedings of the Royal Society A: Mathematical, Physical and Engineering Sciences* **2015**, *471* (2174), 20140792. https://doi.org/10.1098/rspa.2014.0792.

(211) Wakerley, D.; Lamaison, S.; Ozanam, F.; Menguy, N.; Mercier, D.; Marcus, P.; Fontecave, M.; Mougel, V. Bio-Inspired Hydrophobicity Promotes CO2 Reduction on a Cu Surface. *Nat. Mater.* **2019**, *18* (11), 1222–1227. https://doi.org/10.1038/s41563-019-0445-x.

(212) Xing, Z.; Hu, X.; Feng, X. Tuning the Microenvironment in Gas-Diffusion Electrodes Enables High-Rate CO2 Electrolysis to Formate. *ACS Energy Lett.* **2021**, 1694–1702. https://doi.org/10.1021/acsenergylett.1c00612.

(213) Zhu, A. L.; Wilkinson, D. P.; Zhang, X.; Xing, Y.; Rozhin, A. G.; Kulinich, S. A. Zinc Regeneration in Rechargeable Zinc-Air Fuel Cells—A Review. *Journal of Energy Storage* **2016**, *8*, 35–50. https://doi.org/10.1016/j.est.2016.09.007.

(214) Tahira, A.; Ibupoto, Z. H.; Willander, M.; Nur, O. Advanced Co3O4–CuO Nano-Composite Based Electrocatalyst for Efficient Hydrogen Evolution Reaction in Alkaline Media. *International Journal of Hydrogen Energy* **2019**, *44* (48), 26148–26157. https://doi.org/10.1016/j.ijhydene.2019.08.120.

(215) Wang, C.; Li, Y.; Gu, C.; Zhang, L.; Wang, X.; Tu, J. Active Co@CoO Core/Shell Nanowire Arrays as Efficient Electrocatalysts for Hydrogen Evolution Reaction. *Chemical Engineering Journal* **2022**, *429*, 132226. https://doi.org/10.1016/j.cej.2021.132226.

(216) Panda, C.; Menezes, P. W.; Zheng, M.; Orthmann, S.; Driess, M. In Situ Formation of Nanostructured Core–Shell Cu3N–CuO to Promote Alkaline Water Electrolysis. *ACS Energy Lett.* **2019**, *4* (3), 747–754. https://doi.org/10.1021/acsenergylett.9b00091.

(217) Sheng, T.; Sun, S.-G. Electrochemical Reduction of CO2 into CO on Cu(100): A New Insight into the C–O Bond Breaking Mechanism. *Chem. Commun.* **2017**, *53* (17), 2594–2597. https://doi.org/10.1039/C6CC08583K.

(218) Ma, W.; Mashimo, T.; Tamura, S.; Tokuda, M.; Yoda, S.; Tsushida, M.; Koinuma, M.; Kubota, A.; Isobe, H.; Yoshiasa, A. Cerium Oxide (CeO2-x) Nanoparticles with High Ce3+ Proportion Synthesized by Pulsed Plasma in Liquid. *Ceramics International* **2020**, *46* (17), 26502–26510. https://doi.org/10.1016/j.ceramint.2020.07.093.

(219) Tan, J. P. Y.; Tan, H. R.; Boothroyd, C.; Foo, Y. L.; He, C. B.; Lin, M. Three-Dimensional Structure of CeO2 Nanocrystals. *J. Phys. Chem. C* **2011**, *115* (9), 3544–3551. https://doi.org/10.1021/jp1122097.

(220) Ait Abdelouhab, Z.; Djouadi, D.; Chelouche, A.; Hammiche, L.; Touam, T. Structural and Morphological Characterizations of Pure and Ce-Doped ZnO Nanorods Hydrothermally Synthesized with Different Caustic Bases. *Materials Science-Poland* **2020**, *38* (2), 228–235. https://doi.org/10.2478/msp-2020-0038.

(221) Alim, K. A.; Fonoberov, V. A.; Shamsa, M.; Balandin, A. A. Micro-Raman Investigation of Optical Phonons in ZnO Nanocrystals. *Journal of Applied Physics* **2005**, *97* (12), 124313. https://doi.org/10.1063/1.1944222.

(222) Jayakumar, G.; Albert Irudayaraj, A.; Dhayal Raj, A. A Comprehensive Investigation on the Properties of Nanostructured Cerium Oxide. *Opt Quant Electron* **2019**, *51* (9), 312. https://doi.org/10.1007/s11082-019-2029-z.

(223) Chouchene, B.; Chaabane, T. B.; Balan, L.; Girot, E.; Mozet, K.; Medjahdi, G.; Schneider, R. High Performance Ce-Doped ZnO Nanorods for Sunlight-Driven Photocatalysis. *Beilstein J. Nanotechnol.* **2016**, *7* (1), 1338–1349. https://doi.org/10.3762/bjnano.7.125.

(224) Schilling, C.; Hofmann, A.; Hess, C.; Ganduglia-Pirovano, M. V. Raman Spectra of Polycrystalline CeO2: A Density Functional Theory Study. *J. Phys. Chem. C* **2017**, *121* (38), 20834–20849. https://doi.org/10.1021/acs.jpcc.7b06643.

(225) Rajkumar, T.; Sápi, A.; Ábel, M.; Kiss, J.; Szenti, I.; Baán, K.; Gómez-Pérez, J. F.; Kukovecz, Á.; Kónya, Z. Surface Engineering of CeO2 Catalysts: Differences Between Solid Solution Based and Interfacially Designed Ce1−xMxO2 and MO/CeO2 (M = Zn, Mn) in CO2 Hydrogenation Reaction. *Catal Lett* **2021**, *151* (12), 3477–3491. https://doi.org/10.1007/s10562-021-03591-y.

(226) Anushree; Kumar, S.; Sharma, C. Synthesis, Characterization and Catalytic Performance of ZnO–CeO2 Nanoparticles in Wet Oxidation of Wastewater Containing Chlorinated Compounds. *Appl Nanosci* **2017**, *7* (8), 567–575. https://doi.org/10.1007/s13204-017-0596-5.

(227) Grabchenko, M. V.; Mikheeva, N. N.; Mamontov, G. V.; Salaev, M. A.; Liotta, L. F.; Vodyankina, O. V. Ag/CeO2 Composites for Catalytic Abatement of CO, Soot and VOCs. *Catalysts* **2018**, *8* (7), 285. https://doi.org/10.3390/catal8070285.

(228) Liu, Y.; Wang, M.; Cao, L.-J.; Yang, M.-Y.; Ho-Sum Cheng, S.; Cao, C.-W.; Leung, K.-L.; Chung, C.-Y.; Lu, Z.-G. Interfacial Redox Reaction-Directed Synthesis of Silver@cerium Oxide Core–Shell Nanocomposites as Catalysts for Rechargeable Lithium–Air Batteries. *Journal of Power Sources* **2015**, *286*, 136–144. https://doi.org/10.1016/j.jpowsour.2015.03.147.

(229) Ismail, R. A.; Abid, S. A.; Taha, A. A. Preparation and Characterization of CeO2 @Ag Core/Shell Nanoparticles by Pulsed Laser Ablation in Water. *Lasers Manuf. Mater. Process.* **2019**, *6* (2), 126–135. https://doi.org/10.1007/s40516-019-00086-y.

(230) Kang, Y.; Sun, M.; Li, A. Studies of the Catalytic Oxidation of CO Over Ag/CeO2 Catalyst. *Catal Lett* **2012**, *142* (12), 1498–1504. https://doi.org/10.1007/s10562-012-0893-2.

(231) Grabchenko, M. V.; Mamontov, G. V.; Zaikovskii, V. I.; La Parola, V.; Liotta, L. F.; Vodyankina, O. V. The Role of Metal–Support Interaction in Ag/CeO2 Catalysts for CO and Soot Oxidation. *Applied Catalysis B: Environmental* **2020**, *260*, 118148. https://doi.org/10.1016/j.apcatb.2019.118148.

Appendix A

The content of the Appendix A. is a product of an already published scientific work. The content of which is reproduced for the purposes of this Thesis and under permission of the corresponding Journal.

Ilias Stamatelos, Cao-Thang Dinh, Werner Lehnert, and Meital Shviro
ACS Applied Energy Materials 2022 *5* (11), 13928-13938

DOI: 10.1021/acsaem.2c02557

Appendix A includes additional figures and data corresponding to the experimental work presented in Chapter 4.

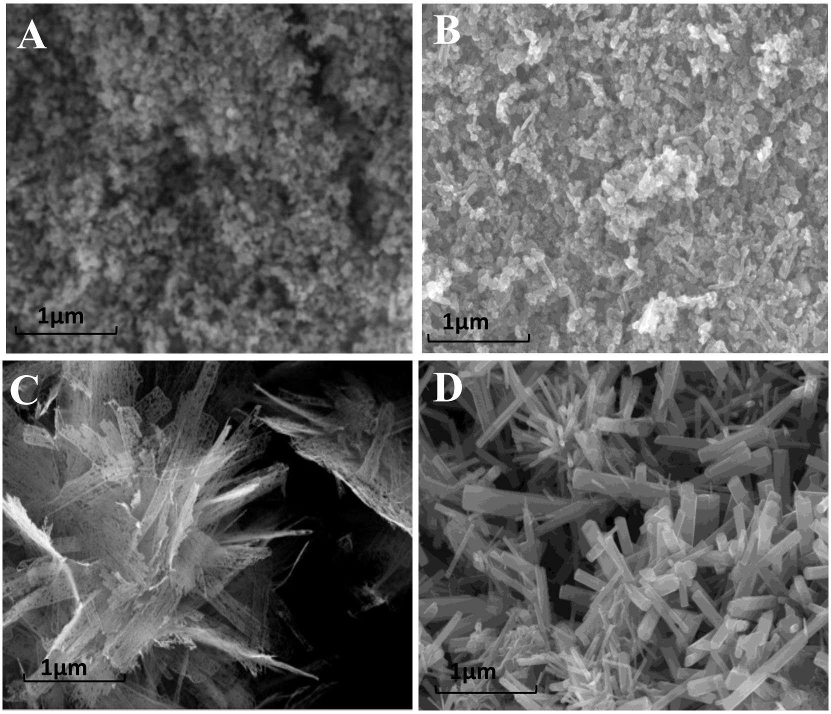

Figure A1: SEM images of all of the ZnO-based powder catalyst materials A.) ZnO-NP, B.) ZnO-RS, C.) ZnO-NS, D.) ZnO-NR.

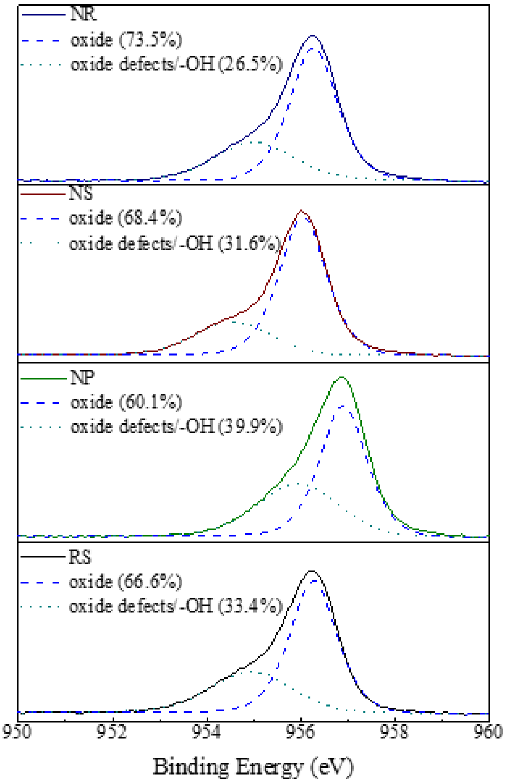

Figure A2: XPS high-resolution spectra of O1s2, for the surface of all of the catalyst materials.

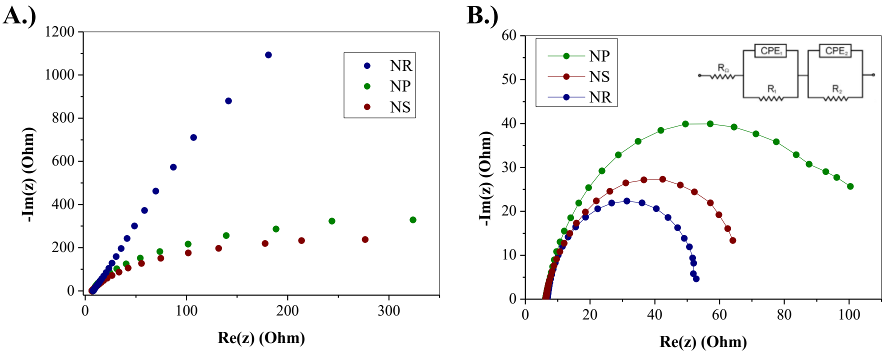

Figure A3: PEIS of the catalyst-loaded GDEs at ECR conditions, A.) At open-circuit potential, OCV, B.) At the onset-potential of each catalyst, presenting the equivalent circuit used for fitting.

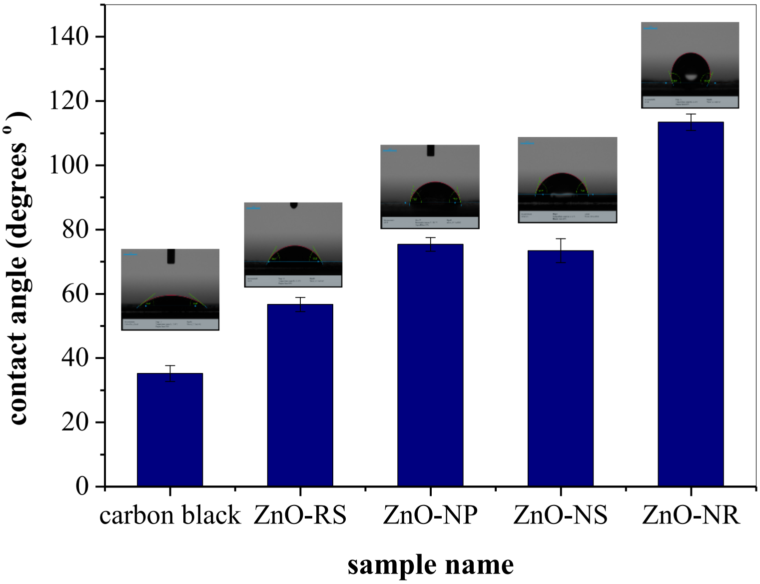

Figure A4: Contact angle of the as-prepared GDEs with the different morphology of the ZnO-based catalysts.

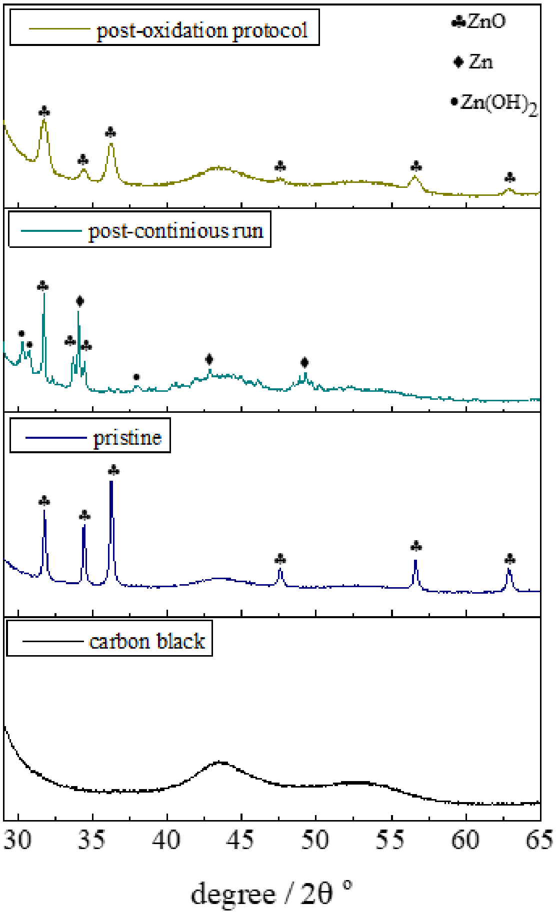

Figure A5: XRD diffractograms of the ZnO-NR GDE after different ECR operation conditions, exhibiting differences induced in the structure ZnO and Zn-metallic phase.

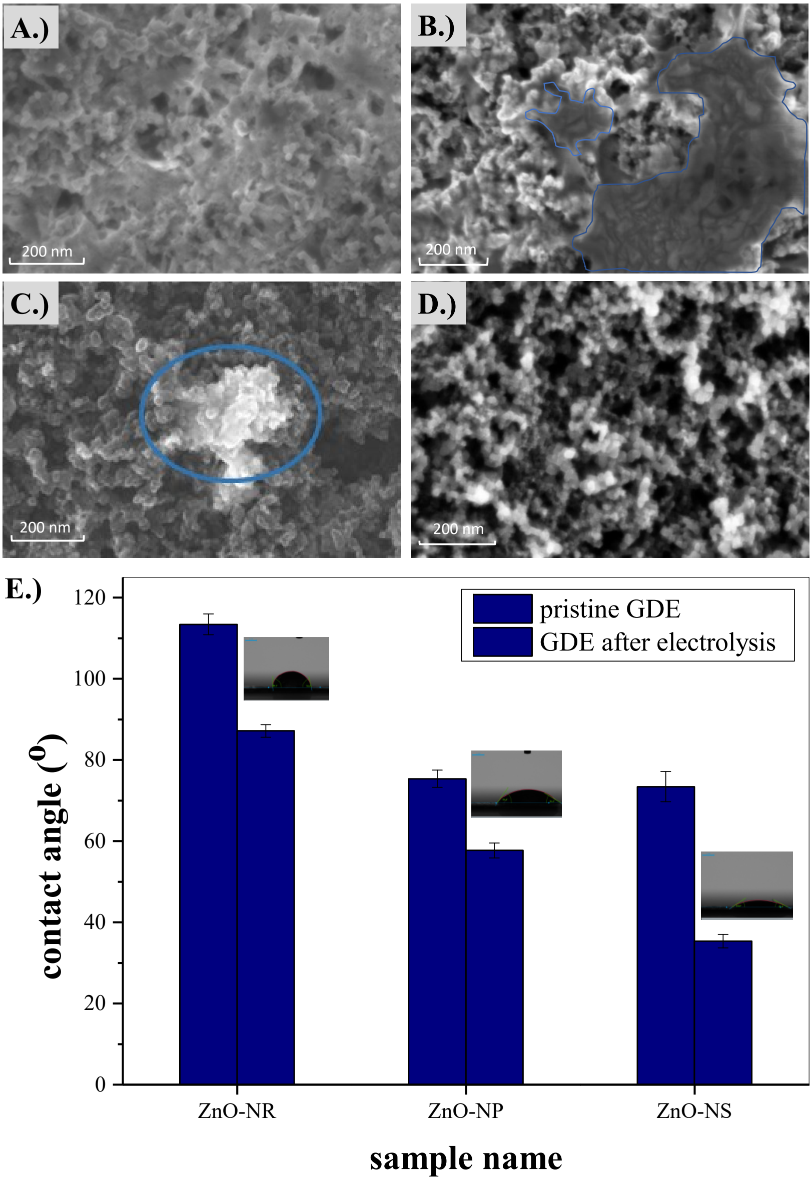

Figure A6: SEM images and contact angle measurements of the ZnO-based GDEs after ECR. Highlighted in blue, are the formed agglomerations of Zn/ZnO over the catalyst layer, A.) SEM image of the ZnO-NR, B.) SEM image of the ZnO-NP, C.) SEM image of the ZnO-NS, D.) SEM image of a blank GDE covered only with carbon black ink, E.) contact angle measurements of the ZnO-based GDEs after ECR.

The changes over the surface morphology are attributed to ZnO agglomerations and reconstruction during the ECR. Even though all the GDE exhibit ZnO agglomerations, the ZnO-NR GDE has a more uniform catalyst surface. To assess how the different ZnO initial morphology affects the agglomerate formation, the ECR was conducted at -160 mA cm^{-2} for 10 h. In the case of ZnO-NR GDE, the altered morphology exhibits an even catalyst layer with no agglomerations. The SEM images of Figure A6B&C, for the ZnO-NP and ZnO-NS GDEs respectively, exhibit large agglomerations, highlighted in blue, that undermine the performance. These agglomerations are attributed to formations of the Zn-metallic and $Zn(OH)_2$ phase, correlated to the data presented in Figure A5.

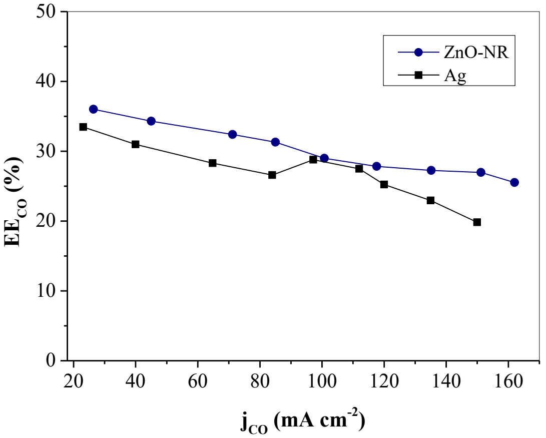

Figure A7: Energy Efficiency for CO production EE$_{CO}$, comparison of the ZnO-NR GDE and the Ag-GDE, each of the same 1 mg cm^{-2} loading, in the MEA cell.

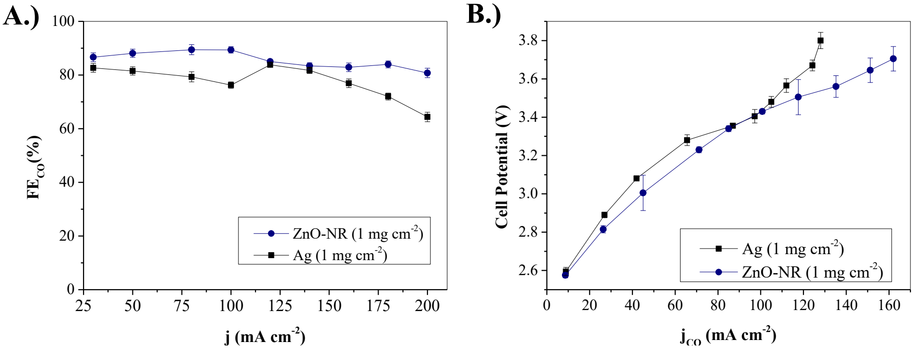

Figure A8: Performance comparison of the ZnO-NR GDE and the Ag-GDE, with the same 1 mg cm^{-2} loading each, in the MEA cell: A.) FE towards CO at different current densities, B.) Polarization curves, exhibiting the partial current density towards CO, j$_{CO}$ of these GDEs.

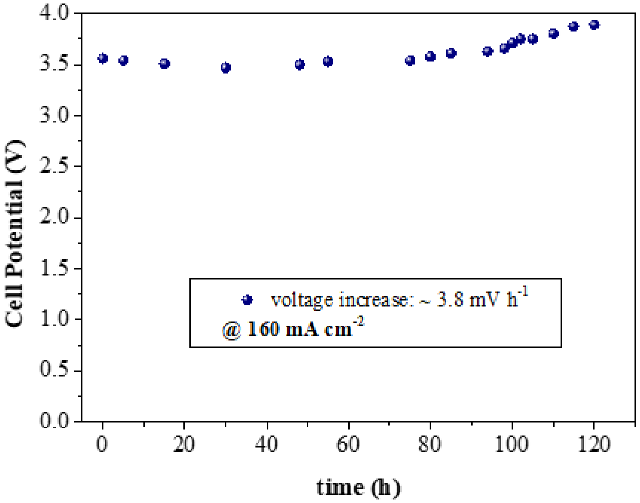

Figure A9: Cell voltage throughout operation under CV2-treatment.

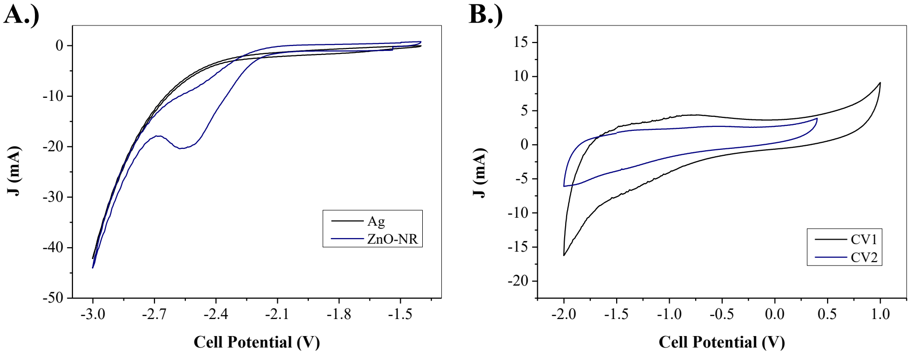

Figure A10: Cyclic-Voltammetry profile for the ZnO-NR and Ag-NP GDEs in the MEA system. A.) initial CVs of the Ag-GDE and the ZnO-NR GDE, B.) Cyclic-Voltammetries on the ZnO-NR GDE, at different oxidation potential windows, representing the different parameters for the periodical oxidation operation, CV1 and CV2.

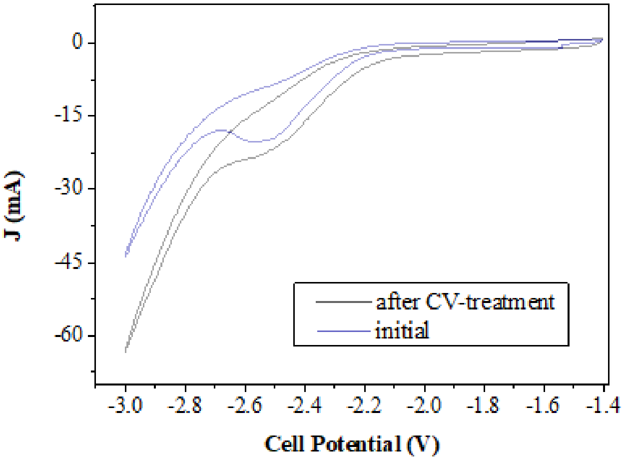

Figure A11: Post-mortem Cyclic-Voltammetry of the ZnO-NR by applying our oxidation strategy during long-term ECR. And comparison with the initial Cyclic-Voltammetry of the ZnO-NR GDE.

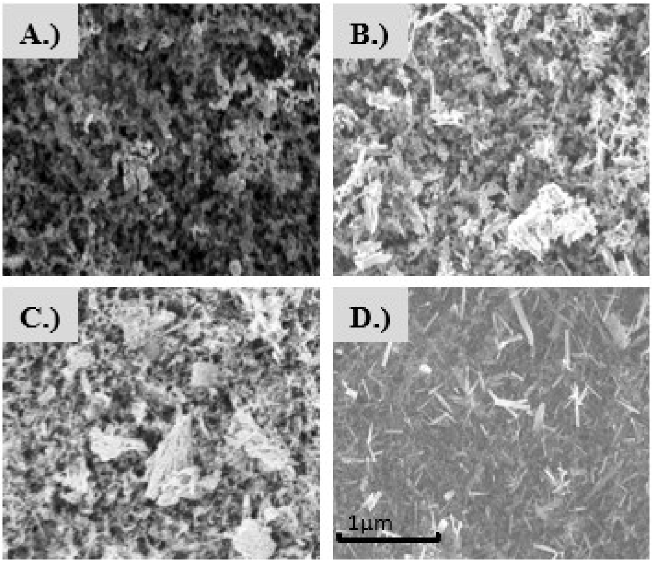

Figure A12: SEM images of the as-prepared catalyst-loaded GDEs, A.) ZnO-NP GDE, B.) ZnO-RS GDE, C.) ZnO-NS GDE, D.) ZnO-NR GDE.

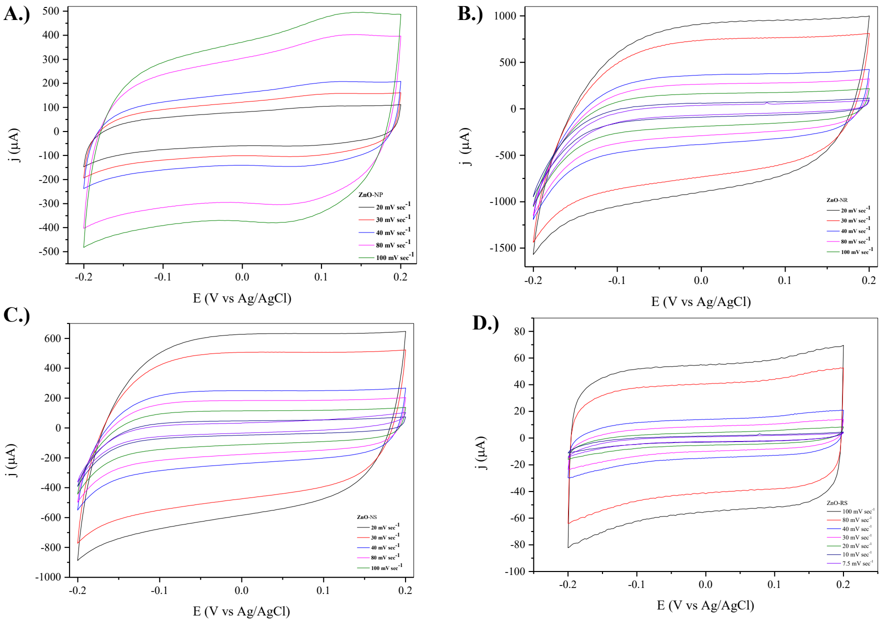

Figure A13: The Cyclic-Voltammetries for the assessment of the C_{dl} for each of the catalyst-loaded GDE with scan rates among 7.5-100 mV sec^{-1}: A.) ZnO-NP, B.) ZnO-NR, C.) ZnO-NS, D.) ZnO-RS.

Appendix B

The content of the Appendix B is a product of an already published scientific work. The content of which is reproduced for the purposes of this Thesis and under permission of the corresponding Journal.

Ilias Stamatelos, Gelson T. S. T. da Silva, Caue Ribeiro, and Meital Shviro

ACS Applied Energy Materials 2023 6 (22), 11510-11520

DOI: 10.1021/acsaem.3c01791

Appendix B includes additional figures and data corresponding to the experimental work presented in Chapter 5.

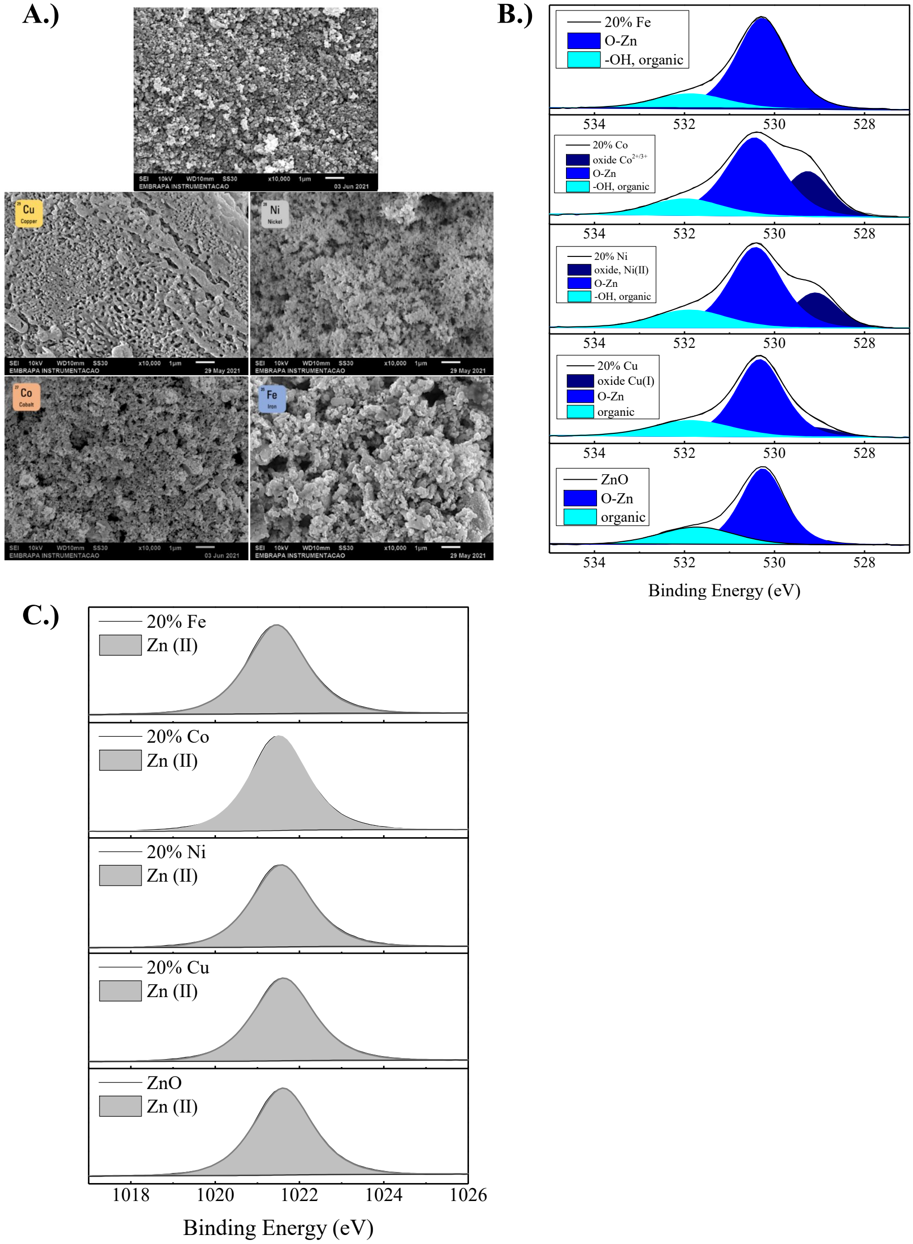

Figure B1: Physical characterizations of the d-block metals heterostructured ZnO-based catalyst materials, A.) SEM images of the different powders, B.) High-resolution oxygen-XPS of the pristine catalyst powders, C.) High-resolution Zn-2p3 XPS of the pristine catalyst powders.

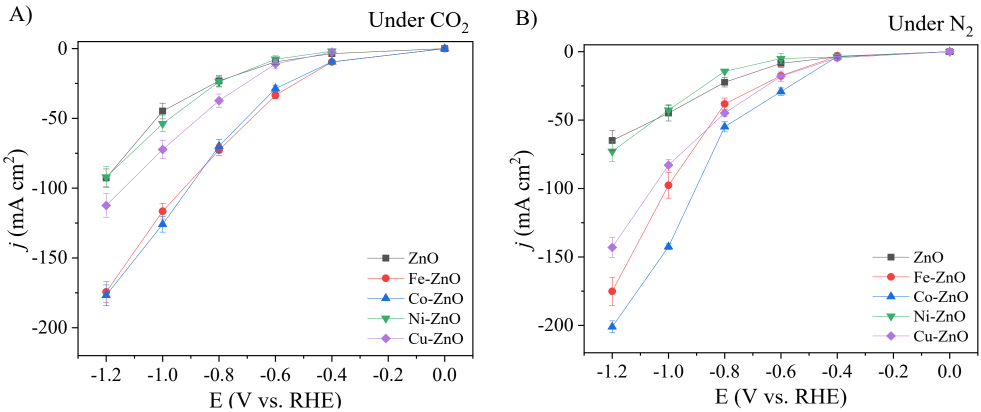

Figure B2: Polarization curves of the catalyst-loaded GDEs. The measurements were conducted in the flow cell in 1 M KOH. A.) Performance at CO_2 feed 20 sccm creating ECR favoring environment, B.) Performance at N_2 feed 20 sccm creating HER favoring environment.

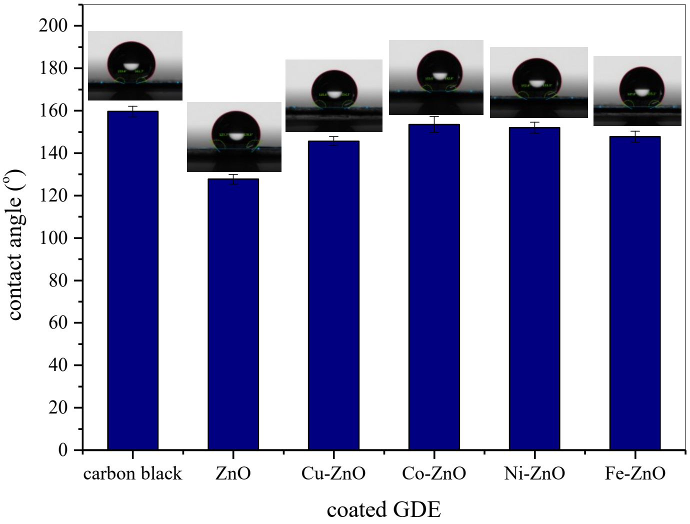

Figure B3: Contact angle of catalyst-coated GDEs. Measured under static conditions, at room temperature using DI water droplet.

The contact angle of the GDEs' reveals similar hydrophobic environments for all the different catalyst materials. The catalyst-loaded GDEs present a lower contact angle in contrast with the blank sample, of a GDE coated with carbon black ink, the latest is related to a stronger affinity of ZnO and the d-block metals with the H_2O.

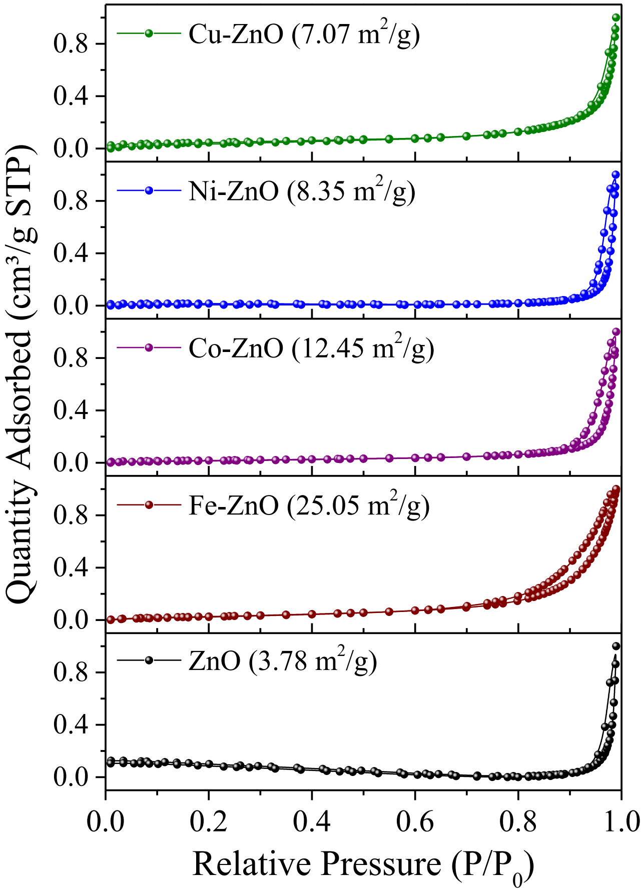

Figure B4: N_2 physisorption isotherms and specific surface area (SSAs) of the prepared materials.

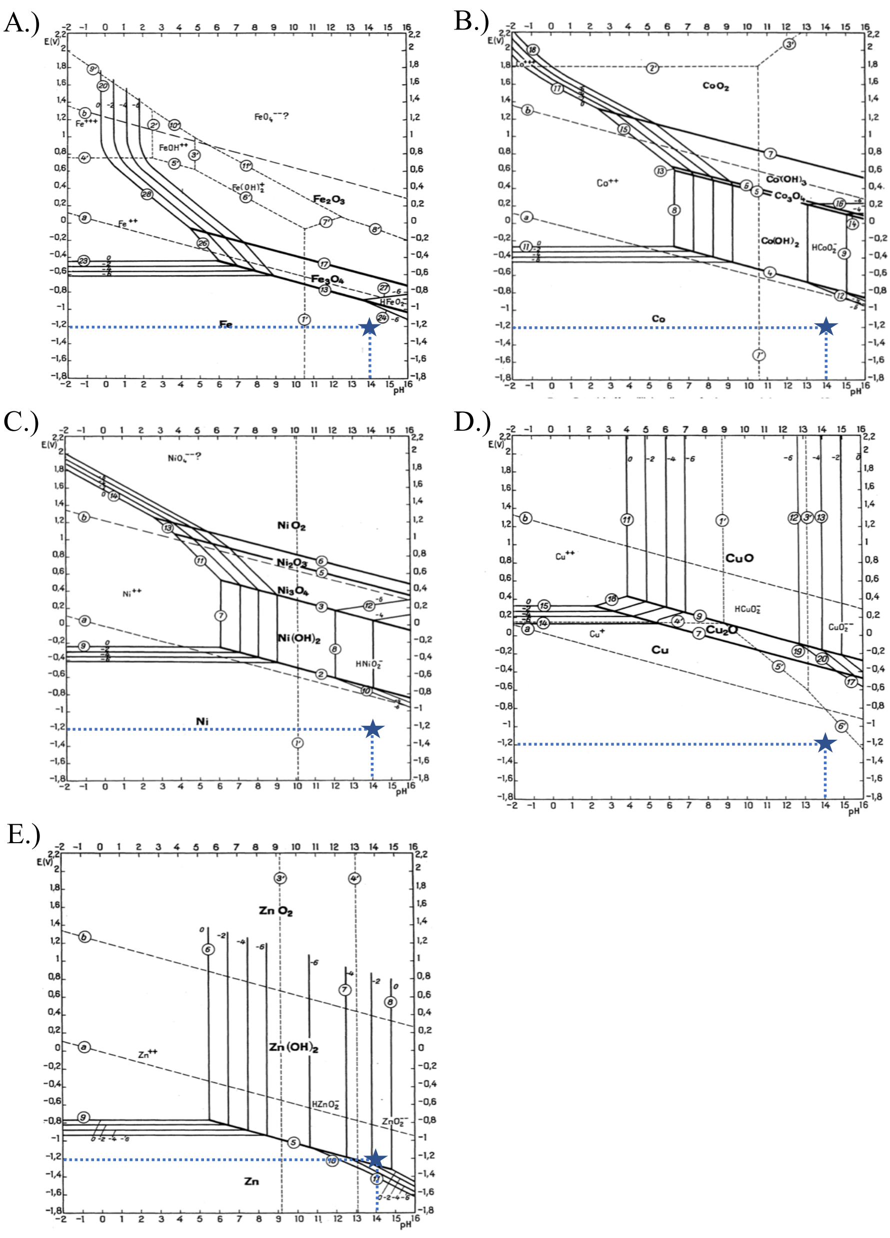

Figure B5: Pourbaix diagrams of the catalyst materials at room temperature A.) Fe-ZnO, B.) Co-ZnO, C.) Ni-ZnO, D.) Cu-ZnO, E.) ZnO.

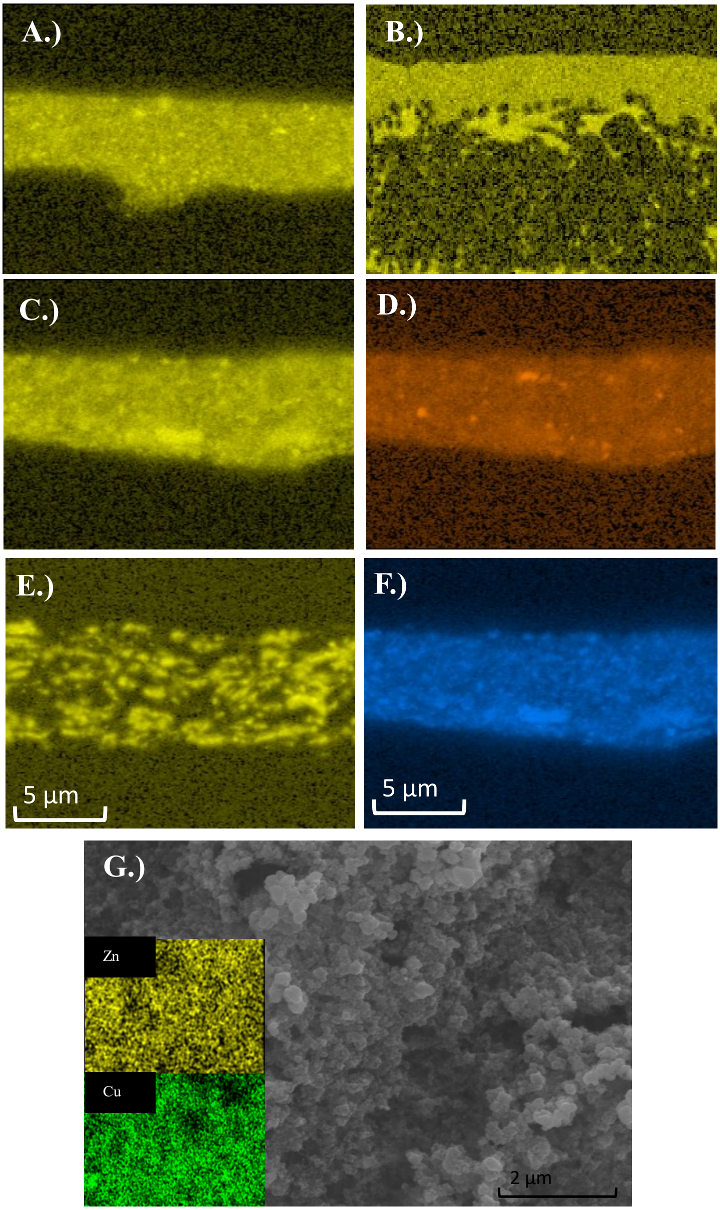

Figure B6: SEM-EDX images of the cross-section of the ZnO and Cu-ZnO GDEs before and after long-term ECR. A.) Zn mapping of the pristine ZnO GDE, B.) Zn mapping of the ZnO GDE after the test, C.) Zn mapping of the pristine Cu-ZnO GDE, D.) Cu mapping of the pristine Cu-ZnO GDE, E.) Zn mapping of the Cu-ZnO GDE after the test, F.) Cu mapping of the Cu-ZnO GDE after the test, G.) SEM and EDX of the catalyst layer of the as-prepared Cu-ZnO GDE.

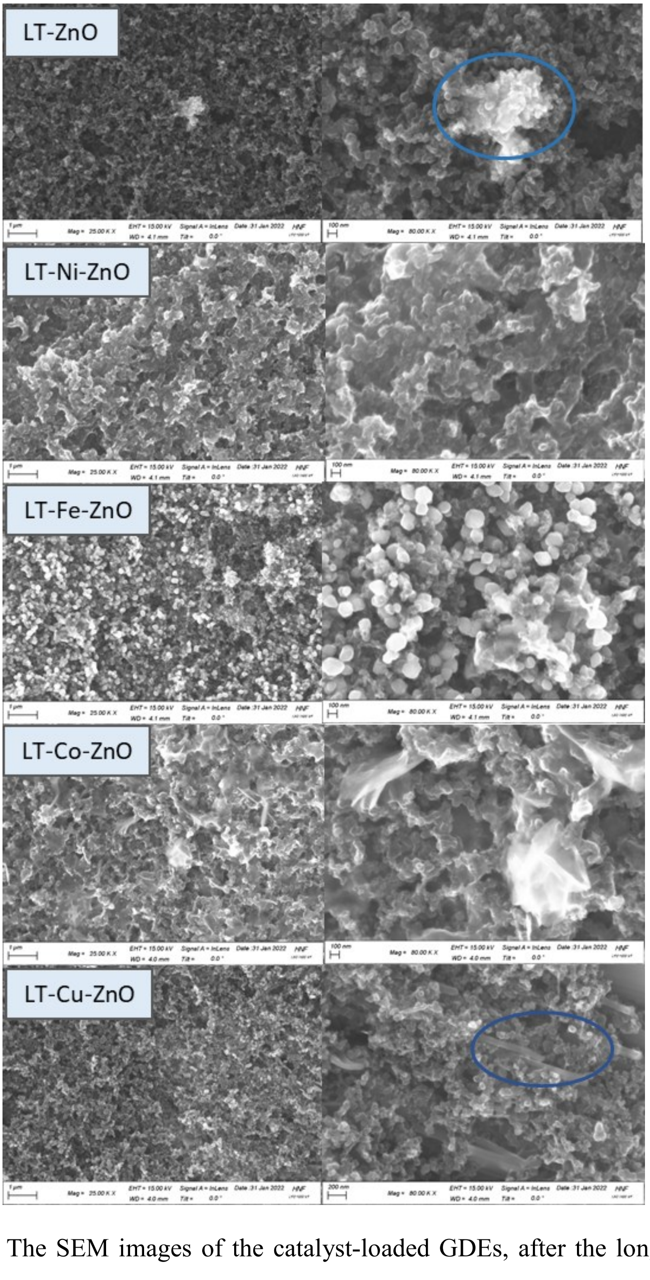

Figure B7: The SEM images of the catalyst-loaded GDEs, after the long-term, LT, testing at -1.4 V_{RHE}. The experiments were conducted under our usual ECR conditions in Flow-Cell configuration, in 1 M KOH.

The SEM images of the GDEs after the long-term run show more details about the decay process of the catalyst layer. Marked in the blue lines the observed aggregates and precipitants formed over the GDE's catalyst layer. The ZnO-GDEs exhibit aggregates of the ZnO material that undermine its active surface. The diffused and extended agglomeration of the catalyst material is more evident in the case of the Ni-, Fe-, and Co-doped ZnO-GDEs. The uneven and degraded morphology of the final surface shows that the performance of the GDE has degraded. Finally, rod-like structures can be seen penetrating the surface of the Cu-ZnO GDE. This is attributed to the formation of potassium carbonate precipitates on the catalyst layer. The impaired hydrophobicity of the surface is responsible for the extensive formation and deep penetration of the precipitates.

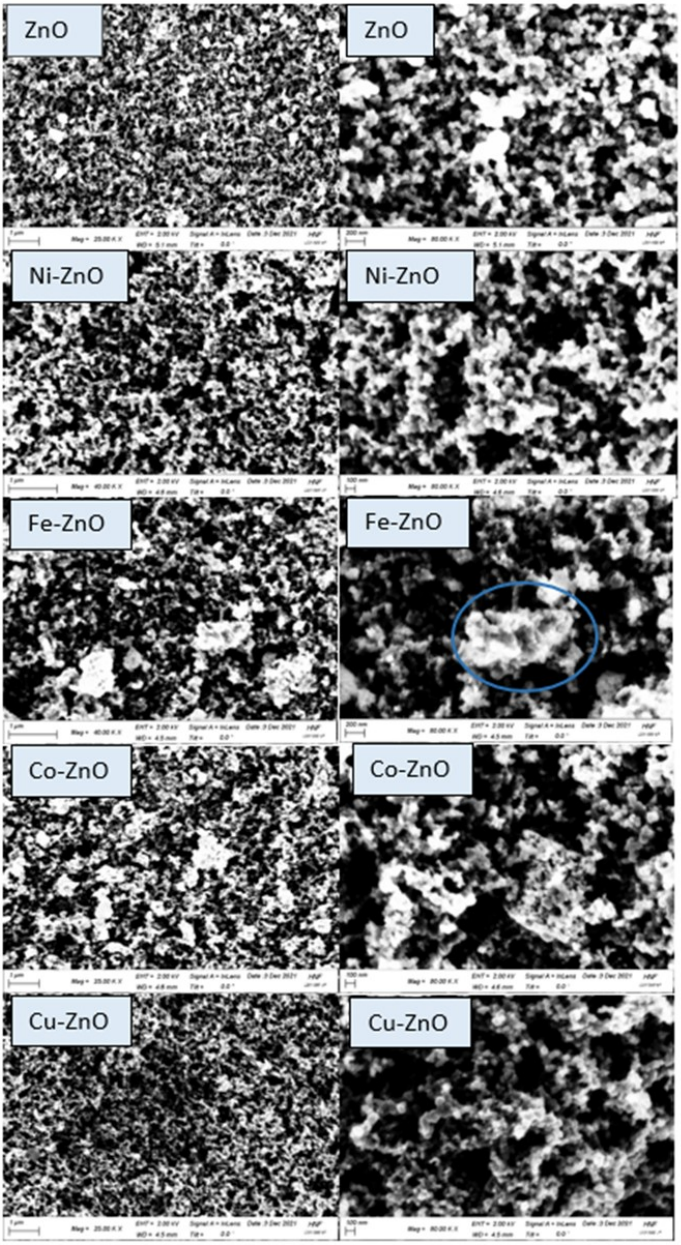

Figure B8: The SEM images of the pristine catalyst-loaded GDEs. The contrast indicates the uniform distribution among the oxide-based and the carbon-black particles.

The SEM images of the initial GDEs, in Figure B8, show a uniform catalyst layer. Only in the case of Fe-ZnO GDEs, the formation of Fe-ZnO agglomerates is observed. The higher magnification shows a good distribution of the ZnO-based nanoparticles for all of the catalyst-loaded GDEs.

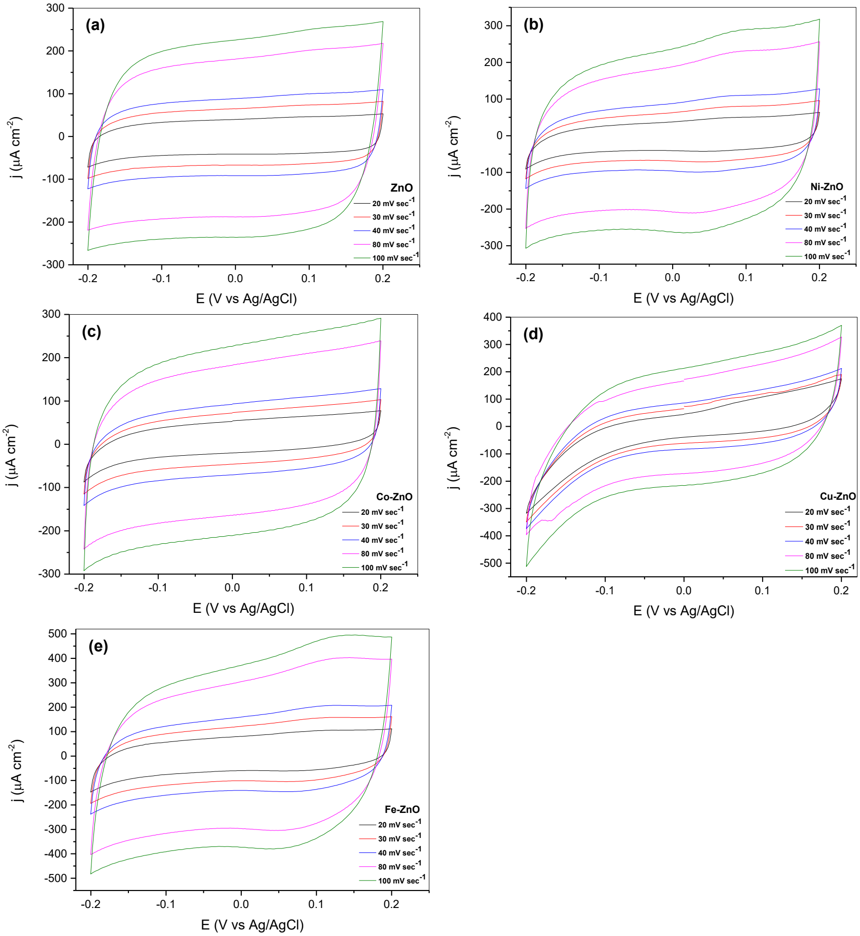

Figure B9: The Cyclic Voltammetries obtained for scan ranges of 20-100 mV sec^{-1}. Measurements were conducted in 0.1 $NaClO_4$ Ar saturated in H-Cell configuration. a.) ZnO GDE, b.) Ni-ZnO GDE, c.) Co-ZnO GDE, d.) Cu-ZnO GDE, e.) Fe-ZnO GDE.

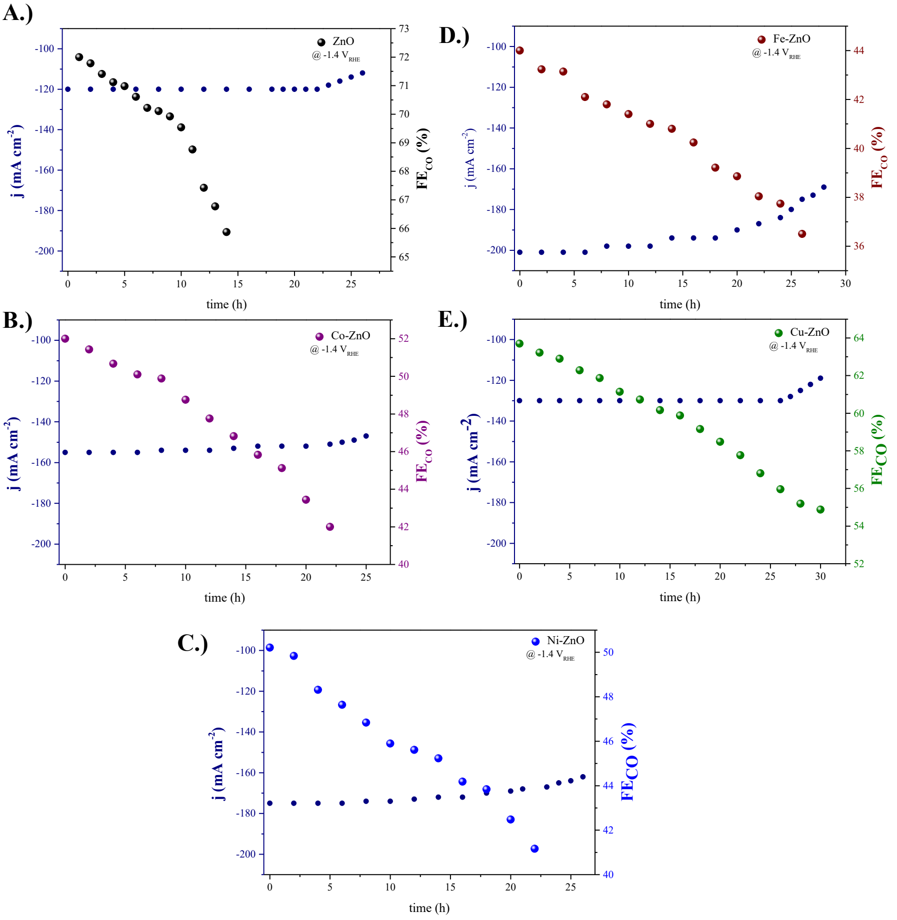

Figure B10: Response of total current density j and faradaic efficiency FE_{CO} during the stress test of constant potentiostatic conditions of -1.4 V_{RHE}. A.) Stability of the ZnO GDE, B.) Stability of the Co-ZnO GDE, C.) Stability of the Ni-ZnO GDE, D.) Stability of the Fe-ZnO GDE, E.) Stability of the Cu-ZnO GDE.

A practical approach of the available active sites and the TOF for CO, TOF_{CO}, of the catalysts was calculated using the following formulas:

$$\mu = A_s \frac{N * m}{Mcat}$$

μ = concentration of active sites [cm^{-2}].

$A_s = \frac{Cdl,cat}{Cdl,ZnO}$, where C_{dl} is the double layer capacitance as calculated by the ECSA.

The A_s ratio describes the total available catalytic centers over the materials surface, in relation with the standard ZnO catalyst.

$N = N_A$ the Avogadro number, $6.023 \bullet 10^{23}$ [atoms $moles^{-1}$].

m = the loading of the catalyst material over the GDE, 0.8 mg cm^{-2}.

M_{cat} = the molecular weight (MW) of the catalyst [g mol^{-1}].

For the composite materials composed of ZnO and metal-oxide, MO), phases, their molecular weight is calculated: $M_{cat} = 0.8MW_{ZnO} + 0.2MW_{MO}$.

$$TOF_{CO} = \frac{Jco}{n*e*\mu}$$

TOF_{CO} = turnover frequency (TOF) for CO [s^{-1}].

J_{CO} = partial current density for CO at -1.2 V_{RHE} overpotential.

μ = concentration of active sites [cm^{-2}].

n = the number of e^{-2} required for the CO formation, $2e^{-}$.

e = the elementary charge, $1.602 \bullet 10^{-19}$ C.

Information about the microstrain was provided through the following formula:

$$\varepsilon = \frac{\beta}{4*tan\theta}$$

ε = micro strain value (%) in the crystalline field of the ZnO phase.

β = is the line broadening at FWHM in radians, Gaussian fitted peak.

θ = the Bragg's angle in degrees, half of 2θ.

The diameter of the crystallites was calculated using the Bragg's law:

$$D = \frac{K*\lambda}{\beta*cos\theta}$$

D = crystalline diameter (nm).

β = is the line broadening at FWHM in radians.

θ = the Bragg's angle in degrees, half of 2θ.

K = diffraction order, 0.94

λ = radiation wavelength, 1.5406 Å.

The effect of the different phases on the ε of the ZnO phase was assessed over the ZnO-wurtzite peak of 56.8°. The diffractogram's peak overlap of the different phases with the ZnO and the altering of the crystalline grain size, D, made the e estimation inaccurate at different 2θ values.

Table B1: Values of the catalysts' microstrain for the ZnO peak of 56.8º.

Catalyst	**2θ**	**β**	**D**	**ε (10^{-3})**
ZnO	56.8	0.32351	29.15	2.61
Cu/ZnO	56.74	0.35082	26.88	2.83
Co/ZnO	56.64	0.46172	22.61	3.37
Ni/ZnO	56.72	0.37285	25.29	3.01
Fe/ZnO	**56.84**	**0.87233**	**20.81**	**6.03**

Table B2: Values of the catalysts' intrinsic catalytic properties.

Catalyst	**MW**	**J_{CO}**	**μ**	**TOF_{CO}**
ZnO	81.38	-101	$9.83\bullet10^{17}$	0.32
Cu/ZnO	81.01	-120	$8.77\bullet10^{17}$	0.41
Co/ZnO	113.26	-81	$6.59\bullet10^{17}$	0.215
Ni/ZnO	80.09	-64	$11.41\bullet10^{17}$	0.176
Fe/ZnO	**97.04**	**-60**	**$13.51\bullet10^{17}$**	**0.142**

Appendix C

The content of the Appendix C is a product of an already published scientific work. The content of which is reproduced for the purposes of this Thesis and under permission of the corresponding Journal.

Ilias Stamatelos, Fabian Scheepers, Joachim Pasel, Cao-Thang Dinh, Detlef Stolten,

Applied Catalysis B: Environment and Energy,Volume 353,2024,124062,

ISSN 0926-3373

Appendix C includes additional figures and data corresponding to the experimental work presented in Chapter 6.

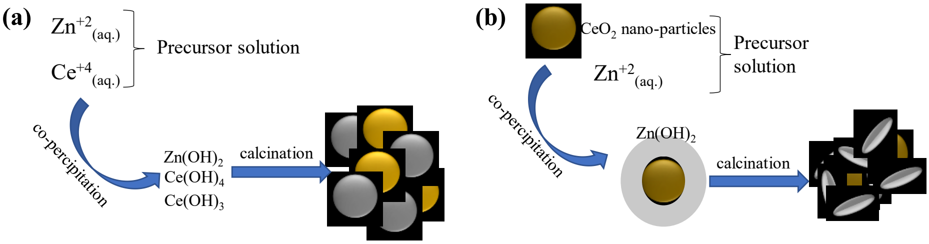

Figure C1. Graphical representation of the two different synthesis approaches of the Zn-Ce oxide catalysts. (a) Gradual co-precipitation of the precursor salts results in the ZnO and CeO_2 nanoparticles of 5 nm being closely packed; (b) sequential precipitation results in a structured architecture, cs, with ZnO as the outer layer.

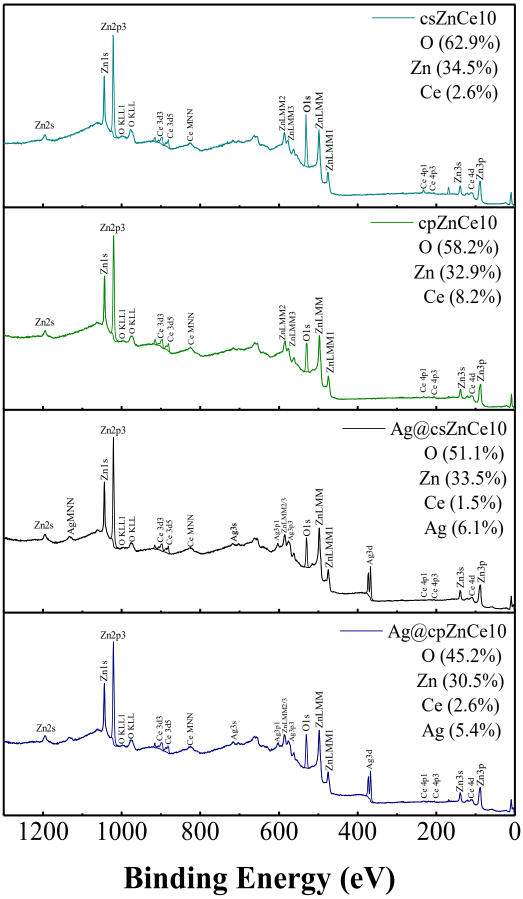

Figure C2. Survey XP specters of the csZnCe10, cpZnCe10 catalysts, and the Ag@csZnCe10 and Ag@cpZnCe10 catalyst powders.

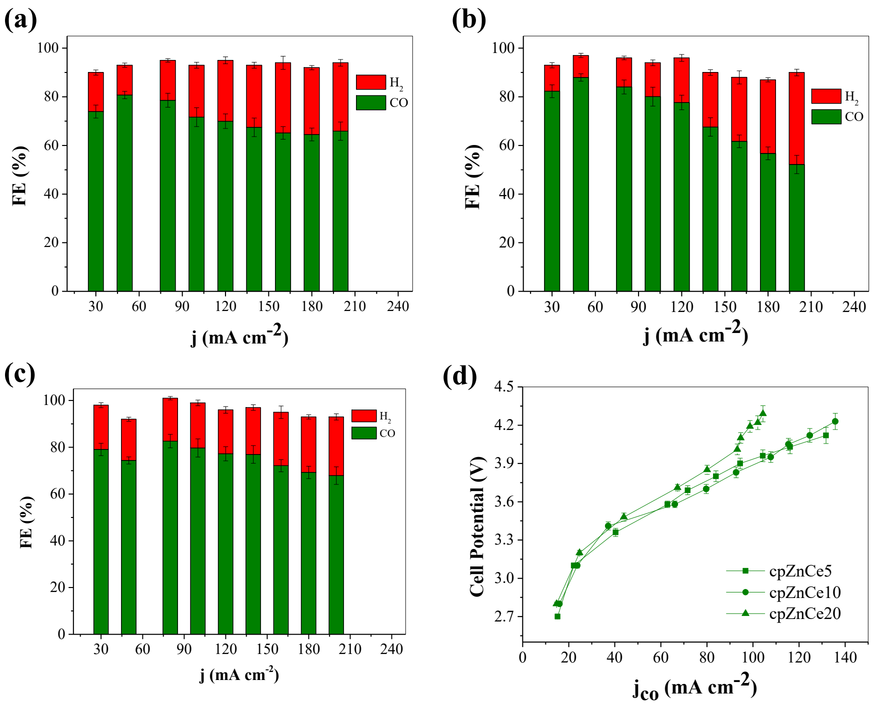

Figure C3. Performance of the ECR of the catalyst-loaded GDEs with CP samples for different Ce contents in the MEA system. (a) Faradaic efficiency of the cpZnCe5-GDE; (b) Faradaic Efficiency of the cpZnCe20-GDE; (c) Faradaic Efficiency of the cpZnCe10-GDE; (d) polarization curve, exhibiting the partial current density for the CO j_{CO} of the different catalyst-loaded GDEs.

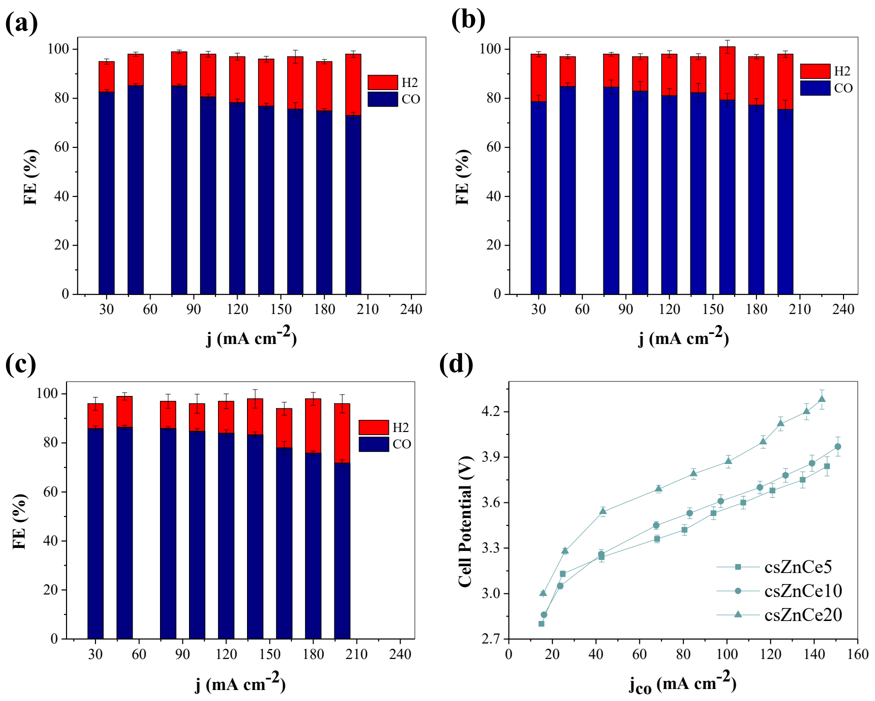

Figure C4. Performance of the ECR of the catalyst-loaded GDEs with CS samples for different Ce contents in the MEA system: (a) Faradaic efficiency of the csZnCe5-GDE; (b) Faradaic efficiency of the csZnCe20–GDE; (c) Faradaic efficiency of the csZnCe10–GDE; (d) polarization curve, exhibiting the partial current density for CO j_{CO} of the different catalyst-loaded GDEs.

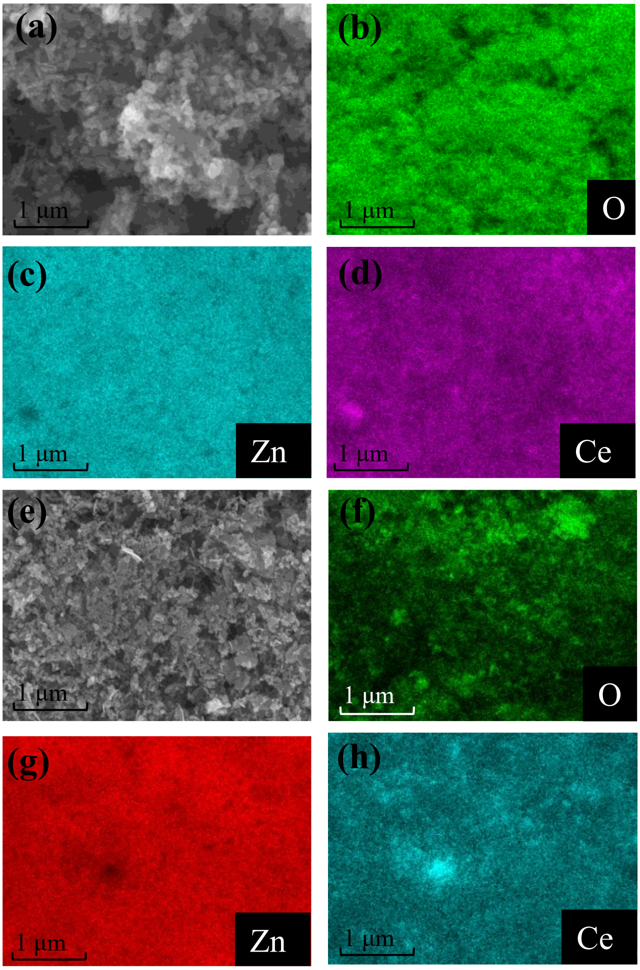

Figure C5. SEM and EDX characterization of the Zn–Ce oxide catalyst. (a) SEM image of the cpZnCe10 powder; (b) EDX of the O-spectra of the cpZnCe10 powder; (c) EDX of the Zn-spectra of the cpZnCe10 powder; (d) EDX of the Ce-spectra of the cpZnCe10 powder; (e) SEM image of the csZnCe10 powder; (f) EDX of the O-spectra of thecsZnCe10 powder; (g) EDX of the Zn-spectra of the csZnCe10 powder; (h) EDX of the Ce-spectra of the csZnCe10 powder.

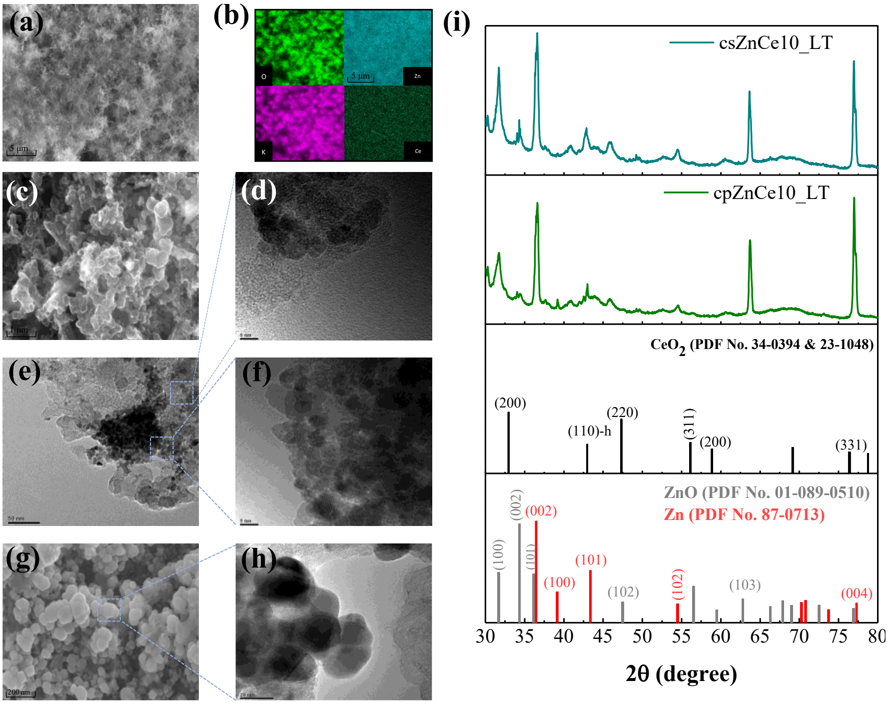

Figure C6. Structural and optical characterization of the catalyst-loaded GDEs after the long-term ECR electrolysis, csZnCe10_LT and cpZnCe10_LT respectively. (a) SEM image of the cpZnCe10_LT–GDE; (b) EDX image of the csZnCe10_LT–GDE; (c) high magnification SEM image of the cpZnCe10_LT-GDE; (d–f) HRTEM images of the catalyst from cpZnCe10_LT–GDE; (g) SEM image of the csZnCe10_LT–GDE; (h) HRTEM images of the catalyst from csZnCe10_LT–GDE; (i) XRD diffractogram of the catalyst-loaded GDEs post-mortem.

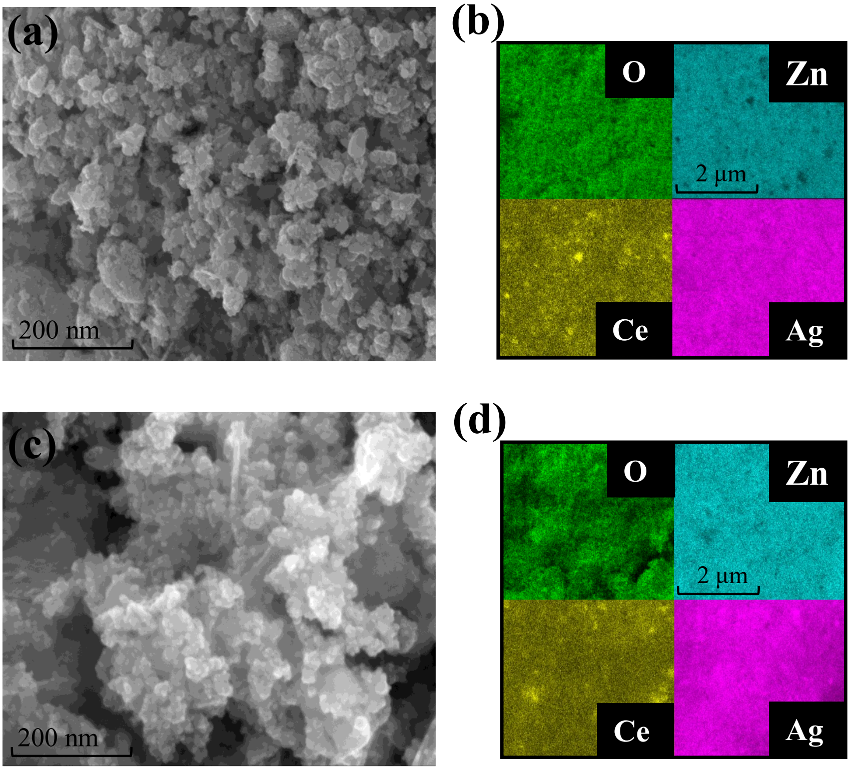

Figure C7. Structural and morphological characterization of the synthesized catalyst powders. (a) SEM image of the Ag@csZnCe10 catalyst powder; (b) EDX image of the Ag@csZnCe10 catalyst powder; (c) SEM image of the Ag@cpZnCe10 catalyst powder; (d) EDX image of the Ag@csZnCe10 catalyst powder.

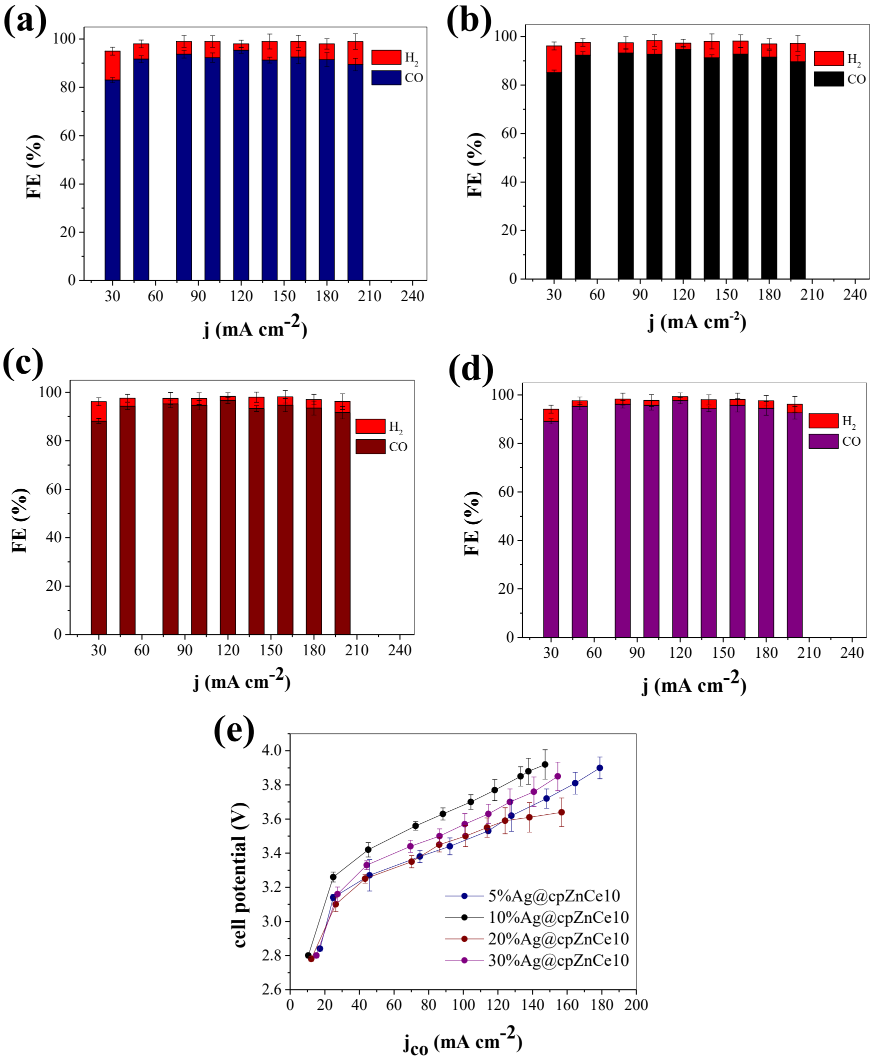

Figure C8. Performance for the ECR for the Zn–Ce–Ag ternary oxide with different Ag quantities. The CP catalyst was covered with a different amount of Ag. The catalyst was loaded on the GDEs and tested in the MEA system. (a) Faradaic efficiency of the Ag@cpZnCe10 GDE; (b) Faradaic efficiency of the 10%Ag@cpZnCe10 GDE; (c) Faradaic efficiency of the 20%Ag@cpZnCe10 GDE; (d) Faradaic efficiency of the 30%Ag@cpZnCe10 GDE; (e) polarization curve exhibiting the partial current density for the CO j_{CO} of the different catalyst-loaded GDEs.

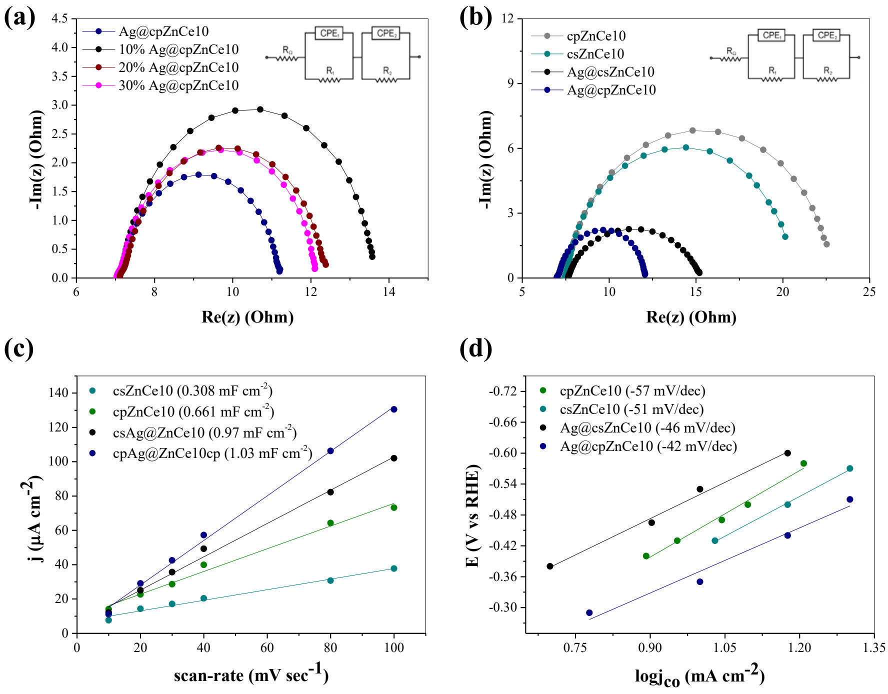

Figure C9. Electrochemical characterizations of catalyst-loaded GDEs. The experiments were conducted in a flow cell electrolyzer in order to focus on the characteristics of the catalyst (cathode). (a) PEIS of the cpZnCe10 catalyst covered with different amounts of Ag; (b) PEIS of the optimized cpZnCe10 and csZnCe10 catalysts and of the optimized Ag@cpZnCe10 and Ag@csZnCe10 GDEs; (c) electrochemically-active surface area (ECSA) of the optimized binary- and ternary-oxide catalyst-loaded GDEs; (d) Tafel slopes of the optimized binary- and ternary-oxide catalyst-loaded GDEs.

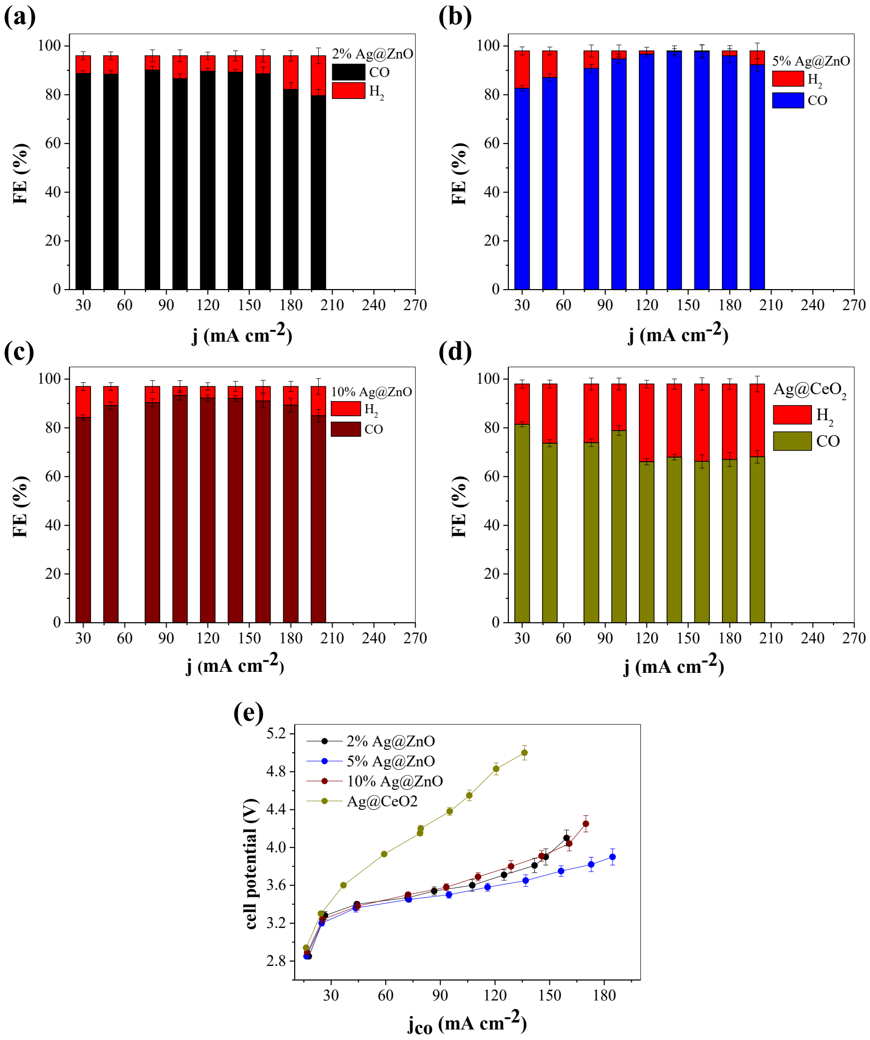

Figure C10. ECR performance of catalyst-loaded GDEs of 1 mg cm^{-2}, in an MEA electrolyzer. (a) FE$_{CO}$ of the Ag@ZnO nanoparticles with 2 % Ag; (b) FE$_{CO}$ of the Ag@ZnO nanoparticles with 5 % Ag; (c) FE$_{CO}$ of the Ag@ZnO nanoparticles with 10 % Ag; (d) FE$_{CO}$ of the Ag@CeO$_2$ nanoparticles with 5 % Ag; (e) polarization of the catalyst loaded GDEs in terms of partial current density for CO j$_{CO}$.

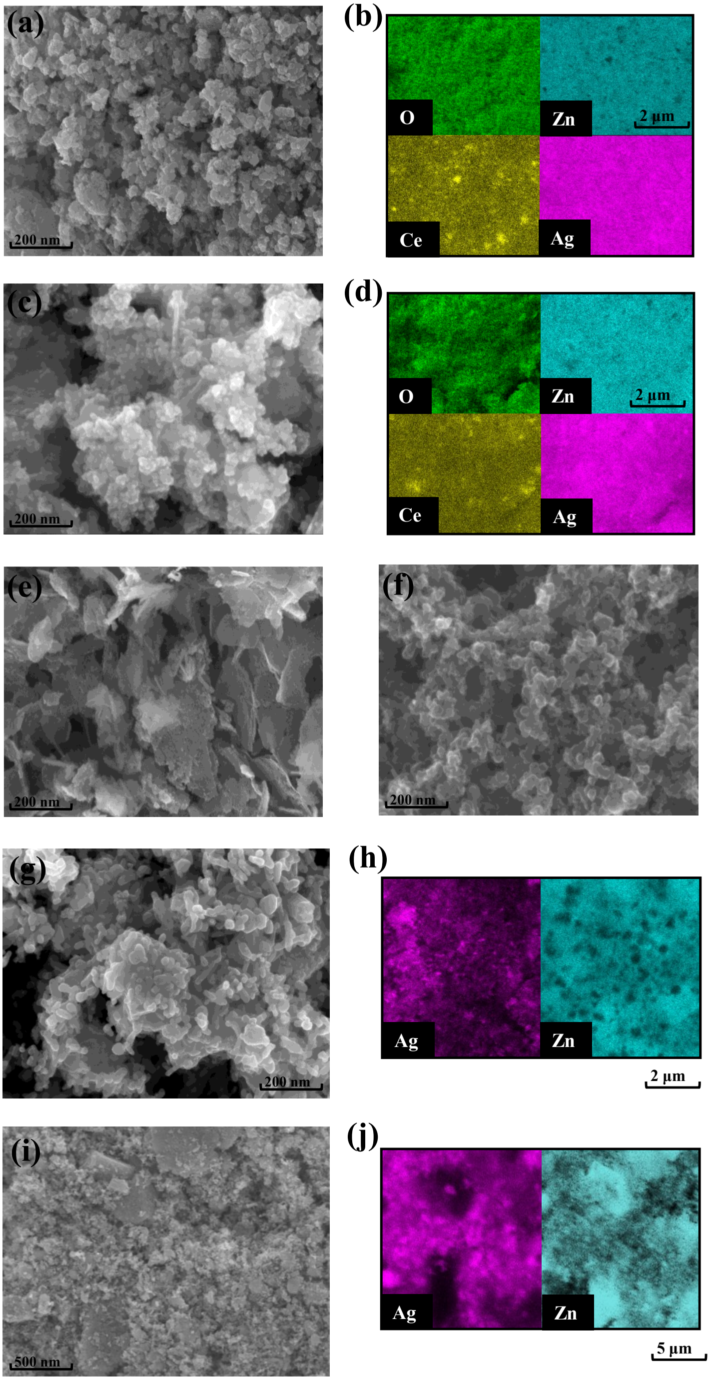

Figure C11. Morphological characterization of the catalyst powders. (a) SEM image of the Ag@csZnCe10 catalyst powder; (b) EDX images of the Ag@csZnCe10 catalyst powder; (c) SEM image of the Ag@cpZnCe10 catalyst powder; (d) EDX images of the

Ag@cpZnCe10 catalyst powder; (e) SEM image of the CeO_2 powder; (f) *post-mortem* SEM image of the CeO_2–GDE after 100 h at 200 mA cm^{-2} in the MEA, used to observe the morphology alteration of the CeO_2 phase; (g) *post-mortem* SEM image of the Ag@csZnCe10–GDE after 100 h of ECR in the MEA; (h) *post-mortem* EDX images of the Ag@csZnCe10–GDE after 100 h of ECR in the MEA; (i) *post-mortem* SEM image of the Ag@ZnO–GDE after 30 h of ECR in the MEA; (j) *post-mortem* EDX images of the Ag@ZnO–GDE after 30 h of ECR in the MEA.

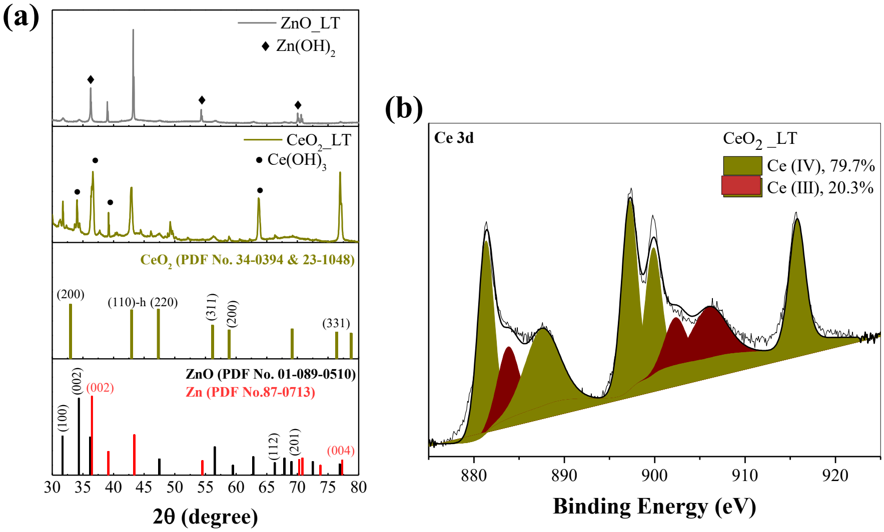

Figure C12. Structural characterization of the CeO_2- and ZnO-loaded GDEs after long-term ECR electrolysis in the MEA. The samples were used to observe the structural alteration of each phase without them interacting. (a) XRD diffractograms of the catalyst-loaded GDEs after long-term ECR electrolysis; (b) high-resolution cerium Ce3d5 XPS of the CeO_2–GDE after 200 h of electrolysis.

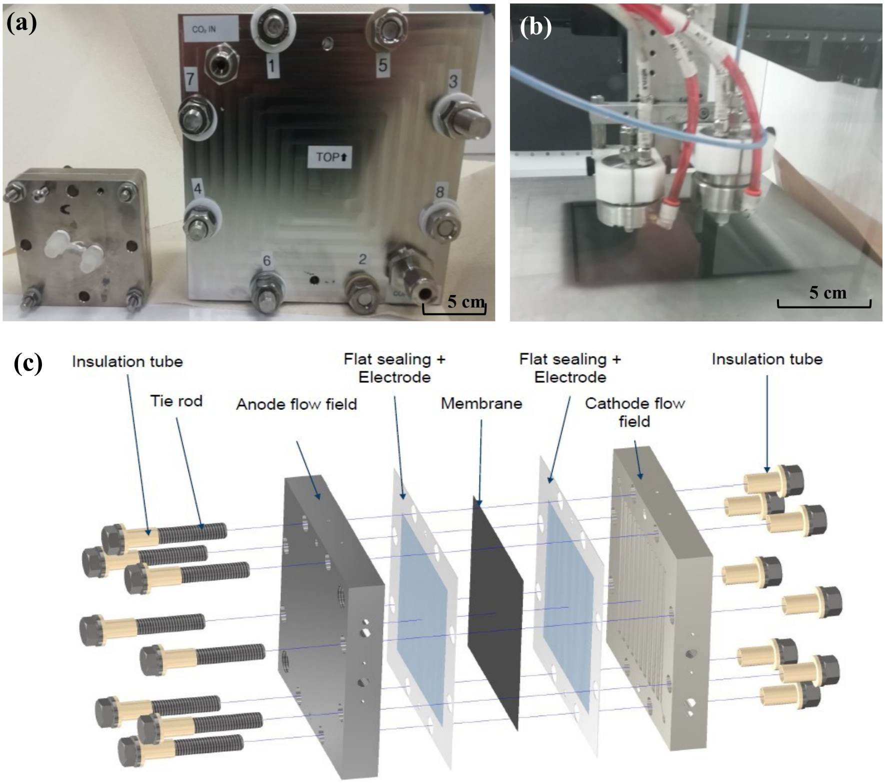

Figure C13. Illustration of the experimental set-up. (a) Image of the small-scale MEA of 2 cm^2 active area and large-scale MEA (100 cm^2 active area); (b) image of the catalyst deposition process, spray-coating, of the GDE in the automated spray-coater; (c) cell architecture of the large-scale MEA with 100 cm^2 active area.

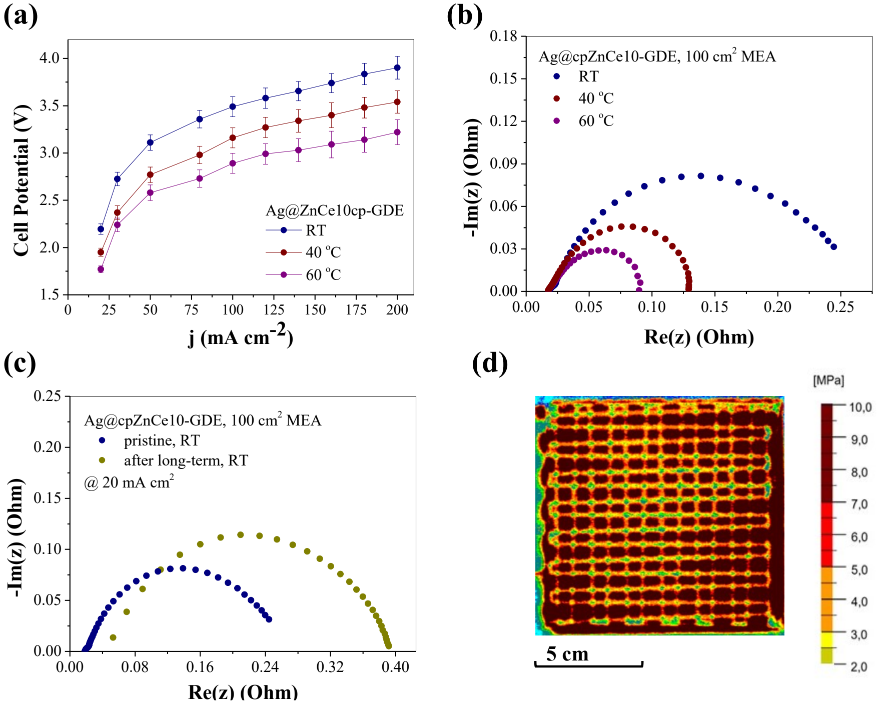

Figure C14. Electrochemical characteristics of the large-scale MEA. (a) Polarization curves of the cell at different temperatures; (b) Galvanostatic Impedance Spectroscopy (GEIS) of the MEA at 20 mA cm^{-2} at different temperatures; (c) GEIS of the large-scale MEA before and after the 200 h ECR, at room-temperature; (d) mechanical pressure distribution over the active area of the 100 cm^2 MEA.

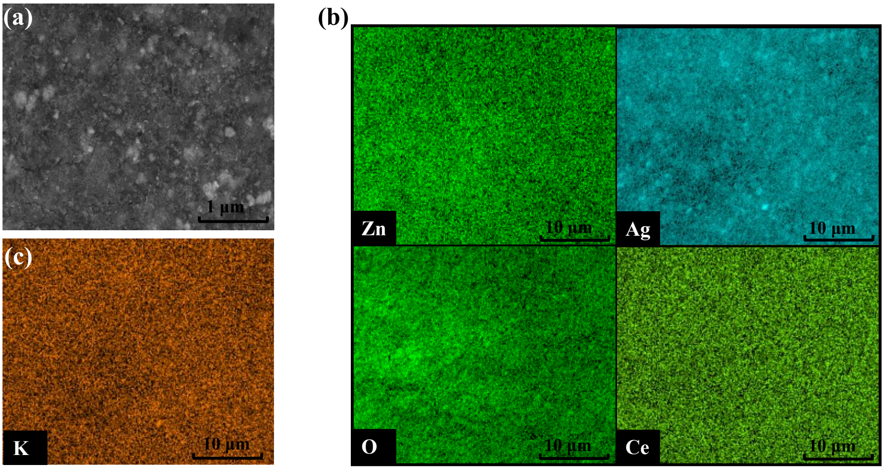

Figure C15. Post-mortem SEM and EDX images of the Ag@cpZnCe10 GDE after 200 h of ECR electrolysis in the large-scale MEA. (a) SEM image of the catalyst layer; (b) EDX images of the catalyst layer; (c) EDX image of potassium over the catalyst layer.

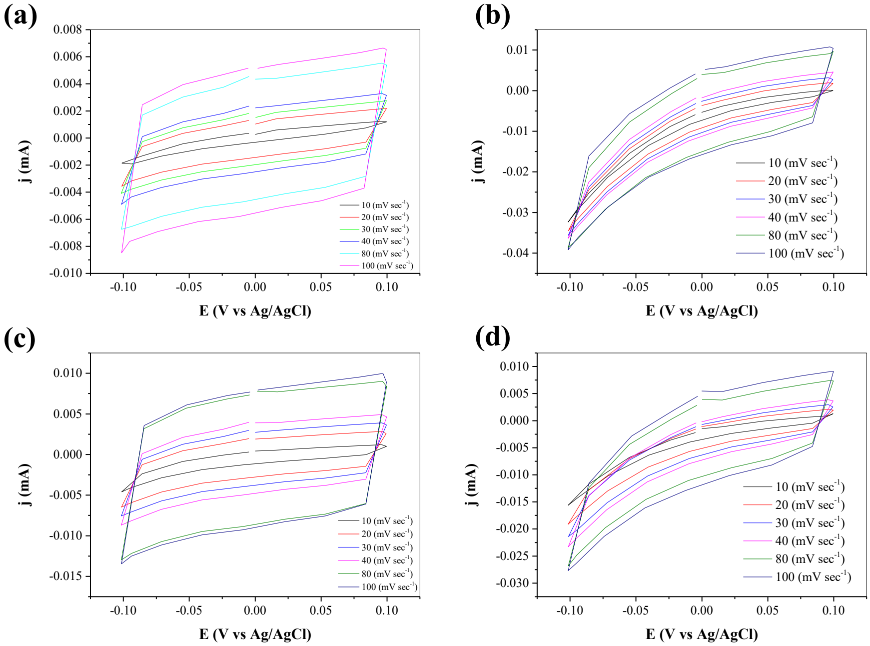

Figure C16. Cyclic Voltammetries (CVs) of the optimized binary- and ternary-oxide catalyst materials. The CVs were measured in a half-cell set-up. (a) csZnCe10 catalyst; (b) cpZnCe10 catalyst; (c) Ag@csZnCe10 catalyst; and (d) Ag@cpZnCe10 catalyst.

Table C1. Elemental composition of all of the catalyst powders synthesized. The concentration (%) of each element was determined using ICP-OES.

Sample	Zn (%)	Ce (%)	Ag (%)
cpZnCe5	70.8	6.7	-
cpZnCe10	64.7	13.8	-
cpZnCe20	54.1	19.9	-
csZnCe5	71.4	6.5	-
csZnCe10	65.4	10.1	-
csZnCe20	54.8	19.5	-
Ag@cpZnCe10	61.3	9.7	6.5
10Ag@cpZnCe10	54.9	10.8	12.7
20Ag@cpZnCe10	47.2	15.8	21.8
30Ag@cpZnCe10	36.2	20.4	31.1
Ag@csZnCe10	64.8	6.9	6.5

List of Figures

List of Tables

Band / Volume 702
Methods for Investigating the Structure-Performance Correlation in Membrane Electrode Assemblies
N. Utsch (2026), XIII, 138, LXVII pp
ISBN: 978-3-95806-901-5

Band / Volume 703
Hot-Spot Formation in Cu(In,Ga)Se$_2$ Thin Film Solar Cells
S. Nofal (2026), xvii, 131 pp
ISBN: 978-3-95806-903-9

Band / Volume 704
Machine Learning Guidance of Manufacturing Process of Solid Oxide Cells
T. Le Dinh (2026), xxi, 122 pp
ISBN: 978-3-95806-904-6

Band / Volume 705
Drivers of spatiotemporal variability of European terrestrial ecosystem processes
C. Poppe Téran (2026), 254 pp
ISBN: 978-3-95806-905-3

Band / Volume 706
Characterization of Nitrogen Reduction Reaction Catalysts for the electrochemical Ammonia Synthesis
D. Sachse (2026), xi, 235, 6 pp
ISBN: 978-3-95806-907-7

Band / Volume 707
Autonomous Image Analysis to Accelerate the Discovery and Integration of Energy Materials
A. Colliard Granero (2026), xiv, 156 pp
ISBN: 978-3-95806-910-7 (Print)
ISBN: 978-3-95806-911-4 (E-Book)

Band / Volume 708
Effect of Soil Mechanical Properties, Root Tip Geometry, and Mucilage on Penetration Restistance to Root Growth
R. K. Janakiram (2026), xxviii, 98 pp
ISBN: 978-3-95806-914-5 (Print)
ISBN: 978-3-95806-915-2 (E-Book)

Schriften des Forschungszentrums Jülich
Reihe Energie & Umwelt / Energy & Environment

Band / Volume 709
European Energy Transition – Germany in the Heart of Europe
T. Klütz, P. Dunkel, T. Busch, J. Linssen, D. Stolten (2026), V, 54 pp
ISBN: 978-3-95806-916-9 (Print)
ISBN: 978-3-95806-917-6 (E-Book)

Band / Volume 710
Development of High-Efficiency Perovskite/Silicon Tandem Solar Cells
Q. Yang (2026), 264 pp
ISBN: 978-3-95806-920-6 (Print)
ISBN: 978-3-95806-921-3 (E-Book)

Band / Volume 711
No-Regret-Maßnahmen der integrierten Netzplanung mit Fokus auf Wasserstoff
T. G. Busch (2026), xx, 325 pp
ISBN: 978-3-95806-922-0 (Print)
ISBN: 978-3-95806-923-7 (E-Book)

Band / Volume 712
Data-Driven Modeling for Digital Representations in Energy Systems
M. C. Zimmer (2026), xv, 166 pp
ISBN: 978-3-95806-926-8 (Print)
ISBN: 978-3-95806-927-5 (E-Book)

Band / Volume 713
Towards integrated PV applications: development of lightweight silicon heterojunction solar modules and their damp-heat and UV stability
K. Zhang (2026), iii, 179 pp
ISBN: 978-3-95806-928-2 (Print)
ISBN: 978-3-95806-929-9 (E-Book)

Band / Volume 714
Zinc-Based Catalysts for the Electrochemical CO2 Reduction
I. Stamatelos (2026), vii, 136 pp
ISBN: 978-3-95806-932-9 (Print)
ISBN: 978-3-95806-933-6 (E-Book)

Weitere ***Schriften des Verlags im Forschungszentrum Jülich*** unter
http://wwwzb1.fz-juelich.de/verlagextern1/index.asp

Energie & Umwelt / Energy & Environment
Band / Volume 714
ISBN 978-3-95806-933-6

Mitglied der Helmholtz-Gemeinschaft

JÜLICH
Forschungszentrum